



Continuous-wave Raman laser in H₂ : semi-classical theory and diode-pumping experiments
by Lei Stone Meng

A dissertation submitted in partial fulfillment of the requirements for the degree of Doctor of
Philosophy in Physics
Montana State University
© Copyright by Lei Stone Meng (2002)

Abstract:

The far-off-resonance continuous-wave Raman laser is studied both theoretically and experimentally in this thesis. A semi-classical theory is developed for the far-off-resonance intracavity Raman process. Pumped by diode lasers in high-pressure H₂ gas, our experiments achieve wide tunability and high conversion efficiency of the vibrational Stokes output. The theory agrees well with the experimental data in the steady state. In addition to the vibrational Stokes output, the rotational Stokes emission is also obtained in the experiments.

The cw Raman laser with anti-Stokes emission is theoretically studied. If all the three fields (pump, Stokes, and anti-Stokes) can be resonant with the cavity, significant cw anti-Stokes output is predicted.

In addition, longitudinal-mode bistability and mode-hop hysteresis in the rotational Stokes laser are experimentally observed. A theory based on a Raman-assisted multi-wave mixing process successfully explains the observation.

CONTINUOUS-WAVE RAMAN LASER IN H_2 : SEMI-CLASSICAL THEORY
AND DIODE-PUMPING EXPERIMENTS

by

Lei Stone Meng

A dissertation submitted in partial fulfillment
of the requirements for the degree

of

Doctor of Philosophy

in

Physics

MONTANA STATE UNIVERSITY
Bozeman, Montana

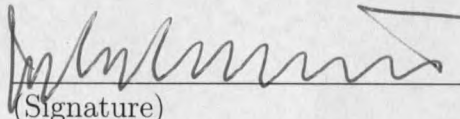
August 2002

APPROVAL

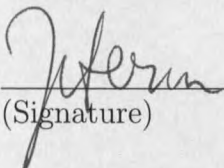
of a dissertation submitted by

Lei Stone Meng

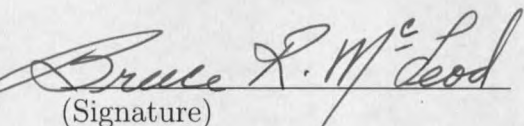
This dissertation has been read by each member of the dissertation committee and has been found to be satisfactory regarding content, English usage, format, citations, bibliographic style, and consistency, and is ready for submission to the College of Graduate Studies.

John L. Carlsten  8-29-02
(Signature) Date

Approved for the Department of Physics

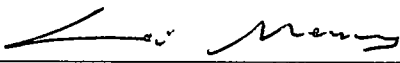
John C. Hermanson  8-29-02
(Signature) Date

Approved for the College of Graduate Studies

Bruce R. McLeod  8-30-02
(Signature) Date

STATEMENT OF PERMISSION TO USE

In presenting this dissertation in partial fulfillment of the requirements for a doctoral degree at Montana State University, I agree that the Library shall make it available to borrowers under rules of the Library. I further agree that copying of this dissertation is allowable only for scholarly purposes, consistent with "fair use" as prescribed in the U. S. Copyright Law. Requests for extensive copying or reproduction of this dissertation should be referred to Bell & Howell Information and Learning, 300 North Zeeb Road, Ann Arbor, Michigan 48106, to whom I have granted "the exclusive right to reproduce and distribute my dissertation in and from microform along with the non-exclusive right to reproduce and distribute my abstract in any format in whole or in part."

Signature 

Date 8/30/02

ACKNOWLEDGEMENTS

First, I would like to thank my advisor, John Carlsten. With almost zero lab skills and poor English, I started my graduate work in John's lab. Without John's extremely patient guidance and support, I could not finish graduate school. Working with John has been a wonderful, and probably the most important experience of my life.

I would like to thank Kevin Repasky, Gregg Switzer, and Jay Brasseur who helped me get started in the lab. Thanks also go to Peter Roos, my coworker and labmate, who gave me many guiding thoughts and discussions. Thanks are also due to those people who helped me: Norm Williams, Peter Sellin, Tom Böttger and Xiaoguang Sun. In addition, I want to thank the rest of my fellow group members, Sytil Murphy and Yihan Xiong for our pleasurable moments in the lab.

Finally, I would like to thank my family; love goes to my parents for their support from far-away China.

TABLE OF CONTENTS

LIST OF TABLES	vii
LIST OF FIGURES	viii
ABSTRACT	xix
1. INTRODUCTION	1
2. SEMI-CLASSICAL THEORY	7
Intracavity Field Equations	7
Maxwell's wave equation and the slowly varying envelope approximation	8
Spatial-mode expansion	9
Density Matrix Equations	11
Theoretical model and Schrödinger equation	11
Adiabatic elimination of C_j	15
Density-matrix equations	17
The polarization	18
The Stokes Laser	18
Population and coherence	19
Polarization and Raman gain	22
Intracavity field equations	25
Field amplitude equation and the steady-state oscillation condition	29
Frequency pulling	30
In terms of pump and Stokes powers	33
Numerical time-dependent solution	36
The Anti-Stokes Emission	42
Complex field equations	42
Analytic steady-state solution for zero two-photon-detuning	47
Numerical solution	50
Bad news: the dispersion	58
3. DIODE-PUMPED CW VIBRATIONAL RAMAN LASER	63
System Overview and Characteristics	63
Vibrational Raman transition in H_2	63
Threshold and steady-state power dependence	66
Stokes conversion efficiency and cavity impedance-matching	71
Tuning characteristics	75
Experiments	82
ECDL pumped, widely tunable	82
Highly efficient cw vibrational Raman laser	89

4. DIODE-PUMPED CW ROTATIONAL RAMAN LASER.....	98
Rotational Raman Transition in H ₂	98
Introduction	98
Rotational Raman linewidth	99
Rotational Raman gain.....	101
Polarization dependence.....	104
Experiment	104
Etalon Effect of the Cavity Mirrors.....	110
5. MODE-HOP HYSTERESIS IN THE ROTATIONAL RAMAN LASER	115
Experimental Observation and Qualitative Explanation	115
Theory	122
6. SUMMARY.....	135
APPENDICES.....	137
APPENDIX A — LASER LOCKING	138
The Error Signal	139
The Electronics.....	142
APPENDIX B — MATHEMATICA PROGRAM	146
REFERENCES CITED	160

LIST OF TABLES

Table	Page
1. Calculated frequency-offset values of the anti-Stokes cavity resonance caused by the dispersion (all for room temperature). Refractive indexes of H_2 are estimated by curve-fitting the published values given in reference [1]; page 6-95.....	61
2. Relative rotational Raman gains for different polarization conditions. . .	104

LIST OF FIGURES

Figure	Page
1. Energy level diagram of the far-off-resonance Raman process.	1
2. Energy levels and laser fields for the far-off-resonance Raman process. The lowest level a is the ground state and the higher level b can be either a vibrational state or a rotational state. We allow an arbitrary number of higher level j and all possible orders of Stokes and anti-Stokes [labeled by an integer q and here only shows $q = \pm 1$ ($q = 0$ is the pump)] generated by the Raman process for the most generality. The transition between levels a and b is electric dipole forbidden. The transitions $j \leftrightarrow a$ and $j \leftrightarrow b$ are far off single-photon resonances and there may be a two-photon detuning δ for the $a \leftrightarrow b$ transition ($\delta < 0$ in the configuration shown).	12
3. Energy levels and laser fields for the Stokes laser. Level a is the ground state; level b can be either a vibrational state or a rotational state; levels denoted by j are multiple excited electronic states. The pump field ω_p ($q = 0$) is red-shifted to the Stokes field ω_s ($q = -1$) and a molecular coherence $\rho_{ab}e^{i\omega_m t}$ is established between levels a and b . There can be a two-photon detuning denoted by δ	19
4. Raman plane-wave gain coefficient as a function of the two photon detuning. For the vibrational Raman transition (792→1180 nm, solid line), $\alpha_{gv}(0) = 1.5 \times 10^{-11}$ m/W [2], linewidth (HWHM) $\gamma_{abv}/2\pi = 250$ MHz [3]. For the rotational transition (792→830 nm, dashed line), $\alpha_{gr}(0) = 0.5 \times 10^{-11}$ m/W [4, 5, 6], linewidth (HWHM) $\gamma_{abr}/2\pi = 510$ MHz [7]. Gain and linewidth are for 10 atm H_2 at 300 K room temperature.	25
5. Theoretical calculation of the amount of frequency-pulling ϕ as a function of two-photon-detuning δ in a cw vibrational Raman laser. Solid line: pump; dashed line: Stokes. Parameters used are: $\lambda_p = 792$ nm; $\lambda_s = 1180$ nm; $\alpha_g = 1.5 \times 10^{-9}$ cm/W (line-center value for 10 atm H_2 at 25°C); mirror transmittance = 0.9999; mirror absorption = 30×10^{-6} ; cavity length = 7.62 cm; and pumping rate is at four times the line-center threshold. In the two shaded areas, the Stokes laser is below threshold.....	33

6. Numerical simulation of the "turn-on" behavior in a cw vibrational Raman laser at different pumping rates. The pump (top) and the Stokes (bottom) powers are plotted as functions of time. The solid line is at a pumping rate of 4 times the threshold; the dashed line is at 2 times the threshold; and the dotted line is at 1.2 times the threshold. All the curves are at the Raman gain line-center (i.e., the two-photon-detuning $\delta = 0$). The left horizontal axis is the intracavity spatial peak power and the right axis is the cavity transmitted power (single end). 37
7. Numerical simulation of the "turn-on" behavior in a cw vibrational Raman laser at different detunings. The pump (top) and the Stokes (bottom) powers are plotted as functions of time. The solid line is when the two-photon-detuning $\delta/2\pi = 0$; the dashed line is when $\delta/2\pi = 200$ MHz; and the dotted line is when $\delta/2\pi = 400$ MHz. All the curves are at the pumping rate of 4 times the line-center threshold. The left horizontal axis is the intracavity spatial peak power and the right axis is the cavity transmitted power (single end). 38
8. After the cw Raman laser in Fig. 7 grows into steady-state (note the horizontal time scale), the calculated phase evolutions of the pump (top) and the Stokes (bottom) beams are shown for different detunings. The slope of the phase curve gives the amount of frequency-pulling. 40
9. The slopes of the phase curves in Fig. 7 as functions of the two-photon-detunings. This numerical calculation agrees with the theoretical plot in Fig. 5. 41
10. The values of $\text{sinc}(\Delta k L/2) = \frac{\sin(\Delta k L/2)}{\Delta k L/2}$ as a function of cavity length. We plotted for $\lambda_p = 792$ nm, $\lambda_s = 830$ nm in the rotational transition and $\lambda_s = 1180$ nm in the vibrational transition at two different H₂ pressures. When the H₂ pressure is 10 atm (3 atm), $\Delta k \approx -4.6\text{m}^{-1}(-1.4\text{m}^{-1})$ for the rotational transition and $\Delta k \approx -54\text{m}^{-1}(-16\text{m}^{-1})$ for the vibrational transition. 7.62 cm (3 in) is the cavity length we have used in the demonstrated cw Stokes laser systems. 46

11. Values of ξ 's are calculated as function of cavity length (left: ξ_- , right: ξ_+). ξ_+ is always larger than 1. 7.62 cm (3 in) is the cavity length we have used in the demonstrated systems. Parameters used for calculation are: $\lambda_p = 792$ nm, $\lambda_s = 830$ nm, $\lambda_a = 757$ nm (rotational), $\lambda_s = 1180$ nm, $\lambda_a = 596$ nm (vibrational), reflectance and absorption are 0.9999 and 30 ppm for both mirrors and all wavelengths, mirror radius of curvature is 50 cm, H_2 pressure is 10 atm, and $\Delta k \approx -4.6 \text{ m}^{-1}$ for the rotational transition, $\Delta k \approx -54 \text{ m}^{-1}$ for the vibrational transition. 49
12. Theoretical plots for the rotational Raman laser (steady-state and zero two-photon-detuning). Thin curves are for the usual Stokes laser while thick curves are when there is four-wave mixing coupling between the Stokes and anti-Stokes. About 8.5% power conversion from Stokes to anti-Stokes, or 3.5% peak power conversion from the input pump to the anti-Stokes can be achieved. Same parameters are used for calculation as in Fig. 11. 50
13. Numerical simulation of the "turn-on" behavior in a cw rotational Raman laser with anti-Stokes emission at different Raman detunings. The pump (top), Stokes (middle), and anti-Stokes (bottom) powers are plotted as functions of time. They are all pumped at 4 times the line-center threshold (= 2.4 mW). The solid line, the dashed line, and the dotted line are when the two-photon-detuning $\delta/2\pi = 0$ MHz, = 400 MHz, and = 800 MHz respectively. The left horizontal axis is the intracavity spatial peak power and the right axis is the cavity transmitted power (single end)..... 53
14. The steady-state powers of pump (top), Stokes (middle), and anti-Stokes (bottom) are numerically calculated as functions of the two-photon-detuning. The solid line, the dashed line, and the dotted line are when the pumping-rate is equal to 2 \times , 4 \times , and 8 \times the line-center threshold (= 2.4 mW) respectively. The left horizontal axis is the intracavity spatial peak power and the right axis is the cavity transmitted power (single end)..... 54
15. The numerically calculated steady-state phase evolutions in a cw rotational Raman laser with anti-Stokes emission at different Raman detunings. The pump (top), the Stokes (middle), and the anti-Stokes (bottom) phases are plotted as functions of time. They are all pumped at 4 times the line-center threshold (= 2.4 mW). The solid line, the dashed line, and the dotted line are when the two-photon-detuning $\delta/2\pi = 0$ MHz, = 400 MHz, and = 800 MHz respectively. 55

16. The numerically calculated steady-state frequency-pullings of pump (top), Stokes (middle), and anti-Stokes (bottom) as functions of two-photon-detuning. The solid line, the dashed line, and the dotted line are when the pumping-rate is equal to $2\times$, $4\times$, and $8\times$ the line-center threshold ($= 2.4$ mW) respectively. The random noise-like curves are when the laser is below threshold. 56
17. The numerically calculated phase difference, $\Delta\phi = 2\phi_p - \phi_s - \phi_a$, as a function of time. The solid line, the dashed line, and the dotted line are when the two-photon-detuning $\delta/2\pi = 0$ MHz, $= 400$ MHz, and $= 800$ MHz respectively. They are all pumped at 4 times the line-center threshold ($= 2.4$ mW). 57
18. The numerically calculated steady-state values of the phase difference, $\Delta\phi = 2\phi_p - \phi_s - \phi_a$, as a function of two-photon-detuning. The solid line, the dashed line, and the dotted line are when the pumping-rate is equal to $2\times$, $4\times$, and $8\times$ the line-center threshold ($= 2.4$ mW) respectively. 57
19. Illustration of (single-photon) dispersion effect in a high-finesse Raman cavity. Solid vertical lines represent actual cavity longitudinal modes (the taller and thicker solid lines means the oscillating modes); dotted vertical lines are "conceptual" and are drawn equally spaced — they are the longitudinal modes assuming that the intracavity refractive index is a constant n_p . Using these modes as a reference, the actual cavity mode-spacings will be larger at lower frequencies and smaller at higher frequencies. ν_{ab} is the Raman shift; Δ is the Raman detuning of the lasing Stokes mode; Δ' is the detuning of the anti-Stokes resonance. The anti-Stokes mode cannot oscillate unless $\Delta' = -\Delta$ 58
20. Dispersion in Raman cavity. Refractive index values are for rotational Raman transition (pump $= 792$ nm, Stokes $= 830$ nm, and anti-Stokes $= 757$ nm) in 10 atm H_2 at room temperature. Δn and $\Delta n'$ are the average index changes per free-spectral-range. 60

21. Energy level diagram for the cw vibrational Raman laser in H_2 . Spectral distances between levels and laser frequencies are drawn to scale. a, Three levels from bottom to top are (thick solid lines): the ground state, the first vibrational state, and the first excited electronic state. Distance between the ground state and the first electronic state is about $90,000 \text{ cm}^{-1}$. b, Zoomed-in diagram showing the two-photon Raman process. The incident pump photon transfers population from the ground state (the vibrational quantum number $v = 0$) to the vibrational state $v = 1$ producing a Stokes photon with a frequency shift of 4155 cm^{-1} 63
22. Vibrational Raman gain linewidth and peak plane-wave gain coefficient in H_2 as functions of pressure at 25°C . A pump wavelength of 792 nm is used in calculating the gain coefficient. 65
23. Theoretically calculated intra-cavity pump and Stokes spatial peak powers as functions of input pump power. This is calculated for the vibrational Stokes emission (1180 nm) pumped by 792 nm laser and the Stokes cavity resonance is in the gain line-center. Cavity finesse is assumed to be $31,400$ ($R = 0.9999$) at both wavelengths. 68
24. Theoretically calculated optical powers measured outside the cavity as functions of input pump power. The calculation parameters are the same as used in Fig.23. We add the Stokes powers in front and back of the cavity to obtain the total Stokes power. 70
25. Theoretically calculated photon conversion efficiency as a function of input pump power. The top x axis labels the pumping rate normalized to the laser threshold. Parameters for calculation are the same as used in Fig.23. Photon conversion efficiency reaches the maximum value at 4 times threshold. 71
26. Various optical fields associated with a high-finesse Raman cavity. Field 1: input pump; 2: directly-reflected pump field from the front mirror; 3: cavity leakage pump field; 4: cavity leakage Stokes field; 5: intra-cavity pump field; 6: intra-cavity Stokes field. Field 2 and 3 have 180° phase difference; thus the total reflected pump field is the destructive interference between these two fields. 72

27. Behaviors of asymmetric pump cavity ($R_{1p} = 0.998$, $R_{2p} = 0.9999$) predicted by the theory. a, Stokes and pump fields as functions of input pump power; b, photon conversion efficiency as a function of input pump power. Above the threshold (3.3 mW), the reflected pump power decreases to approach the impedance-matched condition. The Stokes photon conversion efficiency reaches a maximum value of $\sim 66\%$ at four times threshold. Ideally, if we let all the mirror losses be zero and $R_{2p} = 1$, 100% photon conversion efficiency can be reached (dotted line in b)..... 74
28. Picture of cavity longitudinal modes in a cw Raman laser and how the Stokes field chooses a lasing mode. Frequency distance ν_{ab} between pump and Stokes gain line-center is the Raman shift. $c/2L$ is the cavity longitudinal mode spacing or the free-spectral-range (c : light speed, L : cavity length). This cavity mode picture was first viewed by Roos. 75
29. Tuning picture of the cw Raman laser. Initially the Stokes cavity resonance ν_s has an arbitrary detuning of Δ_0 away from the Raman gain line-center. As the pump frequency ν_p is tuned by $\delta\nu_p$, the Stokes gain line-center is tuned by the same amount. However the frequency change of the Stokes cavity resonance is smaller: $\delta\nu_s < \delta\nu_p$. Thus in this picture the Stokes resonance will be tuned closer to the Raman gain line-center. 76
30. The gain "seen" by three adjacent longitudinal Stokes modes as the pump laser's frequency is tuned. The Stokes longitudinal mode-spacing is assumed to be 2 GHz. For the center Stokes mode, we assume its initial detuning $\Delta_0 = 0$ when $\delta\nu_p = 0$ 78
31. Tuning characteristics of the cw Raman laser in symmetric pump cavity. We calculate the total Stokes power (top), the transmitted pump power (middle) and the reflected pump power (bottom) as functions of the pump frequency tuning. Four different pumping rates, $2\times$, $4\times$, $8\times$, and $16\times$ the line-center threshold are plotted. Parameters used for calculation are the same as those used in Fig. 24 and 25..... 79
32. Tuning characteristics of the cw Raman laser in asymmetric pump cavity. Parameters used for calculation are the same as those used in Fig. 27. 80

33. Experimental setup of the ECDL-pumped vibrational Raman laser. ECDL: external-cavity diode laser; APP: anamorphic prism pair; MML: mode-matching lenses; EOM: electrooptic modulator; $\frac{\lambda}{2}$: half-wave plate; PBS: polarizing beam splitter; $\frac{\lambda}{4}$: quarter-wave plate; HFC: high-finesse cavity; PBP: Pellin-Broca prism. 84
34. Experimental data of the ECDL-pumped vibrational Raman laser. The Stokes power and the transmitted pump power are measured as functions of the input pump power. The lines are the theoretical fits. ... 86
35. Photon conversion efficiency as a function of input pump power. The maximum efficiency is $(12.0 \pm 1.3)\%$ occurring at four times threshold. . 87
36. Tunability of the ECDL-pumped vibrational Raman laser. The 18 nm wavelength of the pump beam (top) results in a 40 nm discretely tunable Stokes beam (bottom). The wavelength measurements were taken with a HP optical spectrum analyzer (resolution: 0.1 nm)..... 88
37. Continuous tuning of the ECDL-pumped vibrational Raman laser. The Stokes power is measured when the pump frequency is tuned (bottom horizontal axis; the Stokes frequency change is shown by the top horizontal axis). We take the measurements at five different pumping rates: $2\times$, $4\times$, $8\times$, $16\times$, and $26\times$ the line-center threshold. The Stokes can be continuously tuned by about 1.3 GHz..... 89
38. Experimental setup of a highly efficient cw vibrational Raman laser. The pump laser is a broad-area diode laser (BADL) injection-locked by an external-cavity diode laser (ECDL). APP: anamorphic prism pair; $\frac{\lambda}{2}$: half-wave plate; MML: mode-matching lenses; EOM: electrooptic modulator; PBS: polarizing beam splitter; $\frac{\lambda}{4}$: quarter-wave plate; HFC: high-finesse cavity. 91
39. Geometry of the injection into the slave BADL diode. The BADL's facet size is $100 \times 1 \mu\text{m}$. It has been experimentally discovered [8, 9] that the best injection-locking performance is achieved when (1) the master beam is injected into one edge of the BADL front facet by an incident angle of $3\text{-}4^\circ$ and (2) the beam waist diameter is $1/2$ width of the front facet area ($50 \times 1 \mu\text{m}$). 92

40. BADL injection-locking results. a, Spectra of BADL's output measured by an optical spectrum analyzer (resolution 0.1 nm) when free-running and injection-locked. b, When injection-locked, the transmitted signal from the scanning Raman HFC (without H₂). The HFC's free-spectral-range is 2 GHz; its linewidth is ~1 MHz. 93
41. Experimental data of the BADL-pumped vibrational Raman laser. a, The Stokes power and the transmitted pump power are measured as functions of the input pump power. b, Photon conversion efficiency as a function of the input pump power. Curves are the theoretical fits. The deviations between the data and the theory are caused by the thermal lens effect of the Raman gas [10]. 95
42. Energy levels in H₂ showing transitions for both vibrational (1180nm) and rotational (830 nm) Stokes pumped with 792 nm. At room temperature of 300 K and a H₂ pressure of 10 atm, the FWHM Raman gain linewidth of the vibrational transition Q₀₁(1) is $\Gamma_v = 0.5$ GHz and the rotational transition S₀₀(1) has $\Gamma_r = 1.02$ GHz. 98
43. Rotational and vibrational Raman linewidth in H₂ as functions of pressure or density at 295 k. 0.146 atm (0.134 amagat) is the cut-off pressure (density) for the rotational transition, below this density, the rotational linewidth is dominated by Doppler-broadening and Eq. (4.1) cannot be applied. The cutoff density for the vibrational transition is 1 amagat. 100
44. Rotational and vibrational Raman gain in H₂ as functions of pressure or density at room-temperature (295-300 K). Both are calculated for the pump wavelength of 792 nm. The rotational gain is for circularly polarized pump light and counter-circularly polarized Stokes output; while the vibrational gain is independent of pump polarization. 103
45. Experimental setup of the ECDL-pumped rotational Raman laser. ECDL: external-cavity diode laser; $\frac{\lambda}{2}$: half-wave plate; PBS: polarizing beam splitter; EOM: electrooptic modulator; SM-PM fiber: single-mode and polarization-maintaining fiber; MML: mode-matching lens; $\frac{\lambda}{4}$: quarter-wave plate; HFC: high-finesse cavity. 105
46. Continuous-tuning data measured from the setup in Fig. 45. 106
47. Power dependences measured from the setup in Fig. 45. 106

48. HFC-mirror transmittance trace provided by the mirror-coating manufacturer (Research Electro-Optics, inc.). The double-wavelength coating at 792 and 1180 nm is originally manufactured for the cw vibrational Raman laser, but the wide coating bandwidth also covers the rotational wavelength at 830 nm. 107
49. (a) The Raman plane-wave gain coefficients associated with the vibrational and rotational Stokes cavity modes as functions of the pump frequency tuning. The cavity resonances of both Stokes are assumed to be at the gain line-center when the relative pump frequency is zero (i.e., $\Delta_0=0$). (b) Based on these gain profiles, calculation of the power of the transmitted pump, the rotational Stokes, and the vibrational Stokes as functions of pump tuning. Parameters used for the calculation are: mirror reflectances: 0.9999; mirror absorptions: 40 ppm at all wavelengths and both mirrors; input pump power: 5 mW. The range shown is in qualitative agreement with the measure data presented in Fig. 46. 108
50. Illustration of the etalon effect of the HFC mirrors. The uncoated back surfaces have reflectances of about 0.034, given by the refractive index of fused silica: 1.4534 (800 nm) [1, page6-25]..... 111
51. Cavity reflected and transmitted laser power (normalized to the coupled input power) as functions of the incident laser's frequency. The incident laser's power remains at ~ 5.3 mW and the cavity coupling efficiency is estimated to be $\sim 85\%$. The laser frequency is measured relative to 378 600.00 GHz by a Burleigh wavemeter with 10 MHz resolution. Because the two cavity mirrors are actually two etalons, the mirrors' effective reflectance is a function of the laser's frequency and this results in periodic reflected and transmitted laser power from the HFC. The curves are fittings assuming sinusoidal effective reflectances (see Fig. 52) of the HFC mirrors. 111
52. Comparison between the sinusoidal effective-reflectances which fit the data and the calculated effective-reflectances based on the etalon model. 114
53. Experimental data showing the mode-hop hysteresis between the two adjacent rotational Stokes modes. Optical frequencies are measured by a Burleigh wavemeter with 10 MHz resolution. The pump frequency is measured relative to 378 350 GHz and the Stokes frequency is measured relative to 360 750 GHz. 116

54. Transmitted pump power (top) and rotational Stokes power (bottom) as functions of pump frequency tuning show butterfly-like patterns. Power discontinuities indicate mode-hops. The input pump beam is circularly polarized and the rotational Stokes is counter-circularly polarized for both modes [11]. The pump frequency tuning is shown relative to 378 384 GHz. Back and forth tuning of the pump frequency is performed twice. 117
55. Picture showing how the mode-hop hysteresis happens. $\delta (< 0)$ and $\delta_+ (> 0)$ are the two-photon-detunings of the rotational Stokes modes ω_s and ω_{s+} respectively. $\Delta_c = \delta_+ - \delta$ is the longitudinal mode spacing of the two Stokes modes. The width of the rotational Raman gain linewidth is sufficient to cover the two adjacent longitudinal Stokes modes. a, The "symmetric point", where the two Stokes modes lie symmetrically away from the line-center, $|\delta| = |\delta_+|$. The sub-threshold mode ω_{s+} loses some gain so it is below threshold. b, The mode-hop point, where $|\delta| > |\delta_+|$ and the mode ω_{s+} reaches the threshold since it is closer to the line-center and the lost gain is compensated. c, After the mode-hop, the steady-state gain is quickly saturated to a lower level so that the mode ω_{s+} sees equal gain and loss. 118.
56. Theoretical model for mop-hop hysteresis. a, The usual Raman process: the pump field at frequency ω_p and the lasing-Stokes mode at frequency ω_s establish a strong coherence between the two energy states oscillating at frequency $\omega_m = \omega_p - \omega_s$. b, The first FWM process: the sub-threshold Stokes $\omega_{s+} = \omega_s + \Delta_c$ beats with the strong pump ω_p , producing a weak coherence sideband oscillating at $\omega_{p-} = \omega_p - \omega_{s+} = \omega_m - \Delta_c$; then the lasing-Stokes mode is scattered off this coherence sideband to produce a weak pump sideband with frequency $\omega_{p-} = \omega_p - \Delta_c$. c, The second FWM process (a and c together): the sub-threshold Stokes ω_{s+} is scattered off the strong coherence, producing another new weak field ω_{p+} . d, A "bonus" new weak field is generated, although it does not contribute to the gain suppression on ω_{s-} : the sideband ω_{p-} is scattered off the strong coherence, producing a new field ω_{s+} . In this plot, we use the thick lines to represent "strong" and the thin lines mean "weak". 120
57. Plot of $f(\delta, R')$ as a function of the two-photon detuning at 3 different pumping rates. $f(\delta, R') = 0$ is when mode-hop should happen. $\delta_1/2\pi = -\Delta_c/2 = 0.985$ GHz (cavity length = 3 inch) is the symmetric point — there is no hysteresis when the laser is pumped right at the threshold. As the laser is pumped harder, we see $\delta_2 > \delta_{1.5} > \delta_1$ — the higher the pumping level, the larger the hysteresis. 132

58. Plot of H as a function of the pumping rate R' . Circles are the experimental measurements. 133
59. Illustration of the Pound-Drever-Hall laser stabilization technique. EOM: electrooptic modulator; PBS: polarizing beam splitter; $\lambda/4$: quarter-wave plate. 139
60. Calculated error signal shape from Eq.(6.11) when either the laser frequency ω_L or the cavity length L is scanned. The in-phase signal is obtained when $\Delta\phi = 0$; the quadrature signal is when $\Delta\phi = \pi/2$. Following parameters are used in calculation: modulation frequency: 12 MHz; mirror reflectance: 0.998 for both mirrors; laser wavelength: 792 nm; cavity length: 7.62 cm. 142
61. Electronic circuit diagram of the EOM driver and phase shifter. It can produce rf sine wave to two output channels. Relative phase of the two channels is adjustable..... 144
62. Electronic circuit diagram of the error signal amplifier. It has variable gain (5k Ω pot) and adjustable dc offset (20k Ω pot)..... 145

ABSTRACT

The far-off-resonance continuous-wave Raman laser is studied both theoretically and experimentally in this thesis. A semi-classical theory is developed for the far-off-resonance intracavity Raman process. Pumped by diode lasers in high-pressure H_2 gas, our experiments achieve wide tunability and high conversion efficiency of the vibrational Stokes output. The theory agrees well with the experimental data in the steady state. In addition to the vibrational Stokes output, the rotational Stokes emission is also obtained in the experiments.

The cw Raman laser with anti-Stokes emission is theoretically studied. If all the three fields (pump, Stokes, and anti-Stokes) can be resonant with the cavity, significant cw anti-Stokes output is predicted.

In addition, longitudinal-mode bistability and mode-hop hysteresis in the rotational Stokes laser are experimentally observed. A theory based on a Raman-assisted multi-wave mixing process successfully explains the observation.

CHAPTER 1

INTRODUCTION

The continuous-wave (cw) Raman laser is a recently developed laser technique for generating tunable high-quality laser beams in the near-infrared. It is based on stimulated Raman scattering as illustrated in Fig. 1.

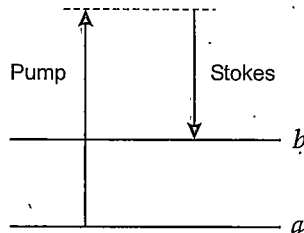
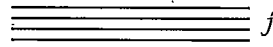


Figure 1 Energy level diagram of the far-off-resonance Raman process.

Level a in Fig. 1 is the ground state, level b is the molecular vibrational or rotational state, and the levels marked j are the excited electronic states. The transition between levels a and b is electric dipole forbidden. Raman scattering occurs when an incident photon (called the pump) interacts with the molecule and generates a

red-shifted photon (called the Stokes). When the intensity of the pump laser is high enough to reach some certain threshold, the Stokes output experiences significant amplification (appearing as exponential growth) and this is called stimulated Raman scattering (SRS). Note that for the 792 nm pump wavelength we will be using in this thesis, the transitions $j \leftrightarrow a$ and $j \leftrightarrow b$ are far off single-photon electronic resonance and therefore we call the Raman scattering in Fig. 1 the “far-off-resonance” Raman process.

Because of this far-off-resonance condition, the gain of the SRS is very low. The SRS threshold is in the range of 10^2 – 10^3 kW of pump power. Therefore traditionally, the SRS is usually associated with high power pulsed lasers. For example, in a review paper written by Bloembergen in 1967 [12], it was said: “The general background for the development of the field of stimulated Raman emission contained the following factors: ...the development of high-power pulsed solid-state lasers.”

Because of the lower intensity of cw pump lasers, to realize SRS in the cw regime, the low Raman gain has to be enhanced in some way. One technique is called resonance enhancement [13, page 101]: the cw pump laser and the Raman medium are chosen so that the pump frequency is near a molecular or atomic resonance. The Raman gain is usually large when near resonance but the drawback is that the SRS is tunable only in the very narrow regions near resonance. Many near-resonance cw Raman lasers have been developed over the last 2-3 decades (for example, references [14] and [15]).

In this thesis, when speaking of a “cw Raman laser”, we refer to a far-off-resonance cw Raman laser exclusively. Instead of resonance enhancement, we utilize high-finesse-cavity enhancement — performing SRS in a high finesse cavity. Currently mirror coating technology is able to manufacture low loss (< 15 ppm) mirrors with high reflectances ($> 99.99\%$). With these mirrors, we are able to build Fabry-Perot cavities with finessees of 10^4 and higher. Furthermore, the mirrors can be doubly coated and the finessees of $> 10^4$ can be realized at both the pump and Stokes wavelengths. Through the use of this double-cavity-enhancement, it can be shown that a SRS threshold of 200 kW can be effectively lowered to 0.8 mW (see page 68). This is an order of 10^8 enhancement and the result is that cw diode laser pumping is fully possible.

The first far-off-resonance cw Raman laser was realized by Brasseur *et al.* in 1998 [16]. Diatomic hydrogen gas (H_2) was used as the Raman gain medium and the pump laser was a frequency-doubled Nd:YAG laser. Roos *et al.* then demonstrated the first diode-pumped cw Raman laser, using a free-running diode laser and a passive optical locking technique [17]. The Stokes laser threshold was as low as $240 \mu\text{W}$. Shortly after, an external-cavity-diode-laser(ECDL)-pumped cw Raman laser succeeded [18]. The Stokes output of this system was able to be tuned over a wide 40 nm range due to the tunability of the ECDL. Next, by improving the cavity impedance-matching, another diode-pumped cw Raman laser was demonstrated to have a high photon-conversion-efficiency of 66% [19, 20]. The latest achievement on the cw Raman laser

was the discovery of the rotational Stokes emission in H_2 [11], while all the above demonstrations were based on the vibrational Raman transition in H_2 .

There are several distinguishing features associated with the cw Raman laser. First, the Stokes output is widely tunable because the far-off-resonance condition leads to flat gain over a wide spectral range. This wide tunability (tens of nanometers) is usually discrete due to the double cavity resonance requirement. But the Raman gain linewidth and the relative movement of the pump and Stokes resonances can bring us a continuous tuning range of 1-2 GHz for the vibrational transition and of >20 GHz for the rotational transition. Second, the Stokes output has a very narrow spectral linewidth. A linewidth of less than 10 kHz has been measured in the Nd:YAG-pumped system [21]. Third, the Stokes output also has a high spatial purity. The Stokes beam is a pure TEM_{00} fundamental Gaussian mode because of the output from the high-finesse non-confocal cavity.

In cw Raman lasers, phase matching is automatically satisfied since the dipole (or molecular coherence) is induced with the proper phase which leads to Stokes growth, independent of the phase relation between the laser and the Stokes waves. This is an advantage of the cw Raman laser compared to other techniques of laser frequency down-conversion, such as the optical parametric oscillator.

The cw Raman laser may provide a novel tool for studying Raman scattering itself. The traditional pulsed-laser-method has its own limitations on studying Raman scattering. For example, vibrational as well as rotational scatterings always appear

at the same time under many conditions, making independent studies on each type impossible. Just as Minck *et al.* wrote in a 1966 paper [22]: "Because in both D_2 and H_2 the vibrational transitions were always stimulated when the laser was plane polarized, it was not possible to measure the polarization dependence of threshold power for the rotational transitions." Now this difficulty can be easily solved in cw Raman lasers. As shown in Chapter 4, the double resonance requirement and the homogeneous gain nature of the Raman medium assures single-mode operation — pure vibrational Stokes or pure rotational Stokes can be selected just by tuning the pump laser's frequency.

The cw Raman laser also serves as a unique system for studying some aspects of basic laser physics, such as mode-mode competition and the resulting dynamics. For example, in Chapter 5 we report a mode-hop hysteresis and bistability observed in a cw rotational Raman laser. When two adjacent longitudinal laser modes lie symmetrically between the homogeneous gain line-center, the laser output shows a mode-hop hysteresis. To our knowledge, such a mode-hop hysteresis in a homogeneous laser has not been directly observed before.

Besides being a down-conversion technique, it is also possible to generate blue-shifted laser light (up-conversion) in a cw Raman laser system. This up-conversion is based on Stokes-anti-Stokes coupling. We will show theoretically that if the triple-resonance condition (i.e., the cavity is resonant simultaneously at the pump, Stokes, and anti-Stokes wavelengths) is satisfied, significant anti-Stokes light can be generated

with the threshold pump power lower than 10 mW (See Section 2).

The structure of this thesis is as follows. Chapter 2 gives the complete semiclassical theory for the cw Raman laser. Not only the Stokes lasing is described mathematically, but the anti-Stokes emission is studied theoretically as well. Both the analytical steady-state solution and the time-dependent numerical simulation are given for the Stokes and anti-Stokes equations. Chapter 3 – 5 give experimental achievements of the diode-pumped cw Raman lasers. The vibrational Stokes lasers are presented in Chapter 3, including general characteristics of the cw Raman laser, the ECDL-pumped system, and the broad-area-diode-laser(BADL)-pumped system. The discovery of the rotational Stokes emission is reported in Chapter 4, including an introduction to the rotational Raman transition, the experimental observations, and a practical issue regarding the cavity's etalon effect. The mode-hop hysteresis effect in the rotational Raman laser is studied in Chapter 5, in which our theoretical model successfully explains the hysteresis.

CHAPTER 2

SEMI-CLASSICAL THEORY

In this chapter, we develop a semi-classical theory for the far-off-resonance cw Raman laser. In the first Section we derive the cw field equations in a laser cavity. In the second Section we study the density matrix equations. Then in the third Section we discuss the cw Raman laser with first-order Stokes generation. Finally, the last Section solves the intracavity Stokes-anti-Stokes coupling.

The semi-classical theory for the single-mode Stokes laser was first developed by Brasseur [23, 21]. We derive his theory in this thesis more systematically and also extend it to a more general case — arbitrary number of intracavity fields. The intracavity Stokes-anti-Stokes coupling equations were derived by the great help from Roos. He solved the same problem fully quantum mechanically [24] and obtained the same results.

Intracavity Field Equations

In this section we derive the laser field equations in a standing-wave Fabry-Perot cavity. We first apply the slowly varying envelope approximation into the classical Maxwell's wave equation. We then separate the time and spatial dependence by a method of normal mode expansion. The references of these derivations are Siegman

[25], Brasseur [23], and Roos [24].

Maxwell's wave equation and the slowly varying envelope approximation

We start from Maxwell's wave equation¹ (in scalar form for simplicity):

$$\ddot{\tilde{E}}(\mathbf{r}, t) + \frac{\sigma}{\epsilon_0} \dot{\tilde{E}}(\mathbf{r}, t) - c^2 \nabla^2 \tilde{E}(\mathbf{r}, t) = -\frac{1}{\epsilon_0} \ddot{P}(\mathbf{r}, t), \quad (2.1)$$

where σ is the ohmic conductivity of the laser medium; ϵ_0 and c are the dielectric permeability and the light velocity of the free space; P is the total macroscopic polarization of the medium. The second term in the left-hand-side of the equation is used to simulate losses in a Fabry-Perot cavity. We suppose that there are multiple fields in the cavity:

$$\tilde{E}(\mathbf{r}, t) = \frac{1}{2} \sum_q [E_q(\mathbf{r}, t)e^{-i\omega_q t} + \text{c.c.}], \quad (2.2)$$

where the integer q will denote the various frequency components inside the cavity such as the pump and the Stokes fields in our later sections. It can also denote different longitudinal modes of the pump or the Stokes depending on the problem, as, for example, in the analysis of the mode-hop hysteresis in a rotational Raman laser in Chapter 5. We assume that the polarization density in the cavity can be written in the same form:

$$\tilde{P}(\mathbf{r}, t) = \frac{1}{2} \sum_q [P_q(\mathbf{r}, t)e^{-i\omega_q t} + \text{c.c.}]. \quad (2.3)$$

1

Throughout this thesis, we use the tilde to denote a quantity that varies rapidly in time, while the slowly-varying amplitudes of Fourier components are written without the tilde.

There may also be external injected fields in the same form:

$$\tilde{E}_e(\mathbf{r}, t) = \frac{1}{2} \sum_q [E_{eq}(\mathbf{r}, t)e^{-i\omega_q t} + \text{c.c.}], \quad (2.4)$$

and the wave equation (2.1) is expanded to

$$\ddot{\tilde{E}}(\mathbf{r}, t) + \gamma_c \dot{\tilde{E}}(\mathbf{r}, t) - c^2 \nabla^2 \tilde{E}(\mathbf{r}, t) = -\frac{1}{\epsilon_0} \ddot{P}(\mathbf{r}, t) + \gamma_e \dot{\tilde{E}}_e(\mathbf{r}, t), \quad (2.5)$$

where we introduce the notation γ_c to represent the intracavity energy decay rate due to primarily the losses of the mirrors, while γ_e represents the coupling rate of the externally injected energy.

Substituting these expansions (2.2)-(2.4) into the wave equation (2.5) and by making the slowly varying envelope approximation[25, page 945], we have for each field q :

$$\dot{E}_q(\mathbf{r}, t) + \left[\frac{\gamma_{cq}}{2} - i \frac{1}{2\omega_q} (\omega_q^2 + c^2 \nabla^2) \right] E_q(\mathbf{r}, t) = i \frac{\omega_q}{2\epsilon_0} P_q(\mathbf{r}, t) + \frac{\gamma_{eq}}{2} E_{eq}(\mathbf{r}, t). \quad (2.6)$$

Here γ_{cq} and γ_{eq} are associated with cavity mirrors' reflectance R , transmittance T and cavity length L by (if we neglect the scattering loss inside the cavity)

$$\gamma_{cq} = -\frac{c}{n_q L} \ln \sqrt{R_{1q} R_{2q}}, \quad (2.7a)$$

$$\gamma_{eq} = \frac{2c}{n_q L} \sqrt{T_{1q}}, \quad (2.7b)$$

where n_q is the refractive index for the field q ; the subscript "1" represents the front mirror that couples the external field E_{eq} and "2" means the back mirror.

Spatial-mode expansion

We next assume that each electric field q inside the cavity can be expanded in a set of normal spatial modes $u_n(\mathbf{r})$:

$$E_q(\mathbf{r}, t) = \sum_n E_{q,n}(t) u_{q,n}(\mathbf{r}). \quad (2.8)$$

These modes are assumed to be solutions of Laplace's equation

$$(\nabla^2 + k_{cq,n}^2) u_{q,n}(\mathbf{r}) = 0 \quad (2.9)$$

which satisfy the boundary condition of the cavity. $k_{cq,n} = \omega_{cq,n}/c$, where $\omega_{cq,n}$ is the cold cavity resonance frequency of the mode (q, n) . We also assume that these modes are orthogonal for the same frequency component q :

$$\iiint_{\text{cavity}} u_{q,n}(\mathbf{r}) u_{q,n}^*(\mathbf{r}) dx dy dz = V_{q,n}, \quad (2.10)$$

$$\iiint_{\text{cavity}} u_{q,n}(\mathbf{r}) u_{q,n'}^*(\mathbf{r}) dx dy dz = 0 \quad (n \neq n'), \quad (2.11)$$

where $V_{q,n}$ is the mode volume occupied by the q -th frequency component in the n -th spatial mode. In the cw Raman laser systems we will study later, all the intracavity fields ($q = \text{pump, Stokes, anti-Stokes...}$) will be in single spatial modes. Therefore we can drop the subscript n in the equations (2.8) through (2.10) and Eq.(2.8) can be written as

$$E_q(\mathbf{r}, t) = E_q(t) u_q(\mathbf{r}). \quad (2.12)$$

Next we substitute Eq.(2.12) and the Laplace equation (2.9) into Eq. (2.6), multiply $u_q^*(z)$ and perform the volume integral (normalized by the volume V_q)

$$\frac{1}{V_q} \iiint_{\text{cavity}} dx dy dz = \frac{1}{V_q} \int_{-L/2}^{L/2} dz \int_0^\infty r dr \int_0^{2\pi} d\phi \quad (2.13)$$

on both sides. By using Eq.(2.10), we obtain for each frequency component q ,

$$\dot{E}_q(t) + \left[\frac{\gamma_{cq}}{2} - i(\omega_q - \omega_{cq}) \right] E_q(t) = i \frac{\omega_q}{2\epsilon_0} P_q(t) + \frac{\gamma_{eq}}{2} E_{eq}(t), \quad (2.14)$$

where $P_q(t)$ is given by:

$$P_q(t) = \frac{1}{V_q} \iiint_{\text{cavity}} dx dy dz P_q(\mathbf{r}, t) u_q^*(\mathbf{r}). \quad (2.15)$$

In deriving Eq.(2.14), $\omega_q^2 - \omega_{cq}^2 \approx 2\omega_q(\omega_q - \omega_{cq})$ has been used.

In order to solve the field equation (2.14), we need to know the relation between P and E . So in the next section we develop the density-matrix equations.

Density Matrix Equations

Theoretical model and Schrödinger equation

We consider a far-off-resonance multilevel Λ -configuration system as shown in Fig. 2.

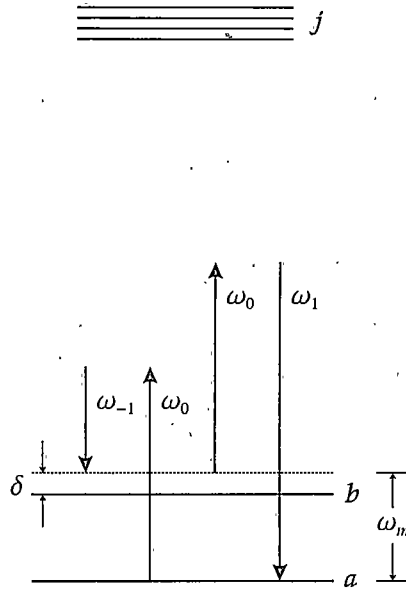


Figure 2 Energy levels and laser fields for the far-off-resonance Raman process. The lowest level a is the ground state and the higher level b can be either a vibrational state or a rotational state. We allow an arbitrary number of higher level j and all possible orders of Stokes and anti-Stokes [labeled by an integer q and here only shows $q = \pm 1$ ($q = 0$ is the pump)] generated by the Raman process for the most generality. The transition between levels a and b is electric dipole forbidden. The transitions $j \leftrightarrow a$ and $j \leftrightarrow b$ are far off single-photon resonances and there may be a two-photon detuning δ for the $a \leftrightarrow b$ transition. ($\delta < 0$ in the configuration shown).

There are multiple upper levels j and two lower levels a and b , as well as multiple laser fields with frequencies ω_q ($q = \text{integer}$). Levels j (with energies ω_j) are coupled to the two lower levels (with energies ω_a and ω_b) by electric dipole transitions, while the transition between a and b is electric dipole forbidden. The transitions $j \leftrightarrow a$ and $j \leftrightarrow b$ are far off single-photon resonances and there may be a two-photon detuning δ for the $a \leftrightarrow b$ transition. The results of this model have been given by Harris [26, 27] and Fam Le Kien [28]. In this section, we derive it in detail.

The multiple fields are given by Eq. (2.2)²:

$$\tilde{E} = \frac{1}{2} \sum_q (E_q e^{-i\omega_q t} + \text{c.c.}), \quad (2.16)$$

where

$$\omega_q = \omega_0 + q(\omega_b - \omega_a - \delta) = \omega_0 + q\omega_m, \quad (2.17)$$

or

$$\omega_q = \omega_{q-1} + q\omega_m. \quad (2.18)$$

In the cw Raman laser, we have only two fields: $q = 0$ for the pump and $q = -1$ for the first-order Stokes. But we still do our derivation for multiple fields so that the density matrix equations can be easily extended to other cases, for example, the anti-Stokes emission.

The system Hamiltonian can be written as this matrix form:

$$H = \begin{pmatrix} \hbar\omega_a & 0 & \cdots & V_{aj} & \cdots \\ 0 & \hbar\omega_b & \cdots & V_{bj} & \cdots \\ \vdots & \vdots & \ddots & \vdots & \\ V_{ja} & V_{jb} & \cdots & \hbar\omega_j & \cdots \\ \vdots & \vdots & & \vdots & \ddots \end{pmatrix}, \quad (2.19)$$

where

$$V_{aj} = V_{ja}^* = -\mu_{aj} \cdot \frac{1}{2} \sum_q (E_q e^{-i\omega_q t} + \text{c.c.}), \quad (2.20a)$$

$$V_{bj} = V_{jb}^* = -\mu_{bj} \cdot \frac{1}{2} \sum_q (E_q e^{-i\omega_q t} + \text{c.c.}), \quad (2.20b)$$

and μ_{aj} and μ_{bj} are the dipole moments between levels $a \leftrightarrow j$ and $b \leftrightarrow j$ respectively.

²

If written in full notation, $\tilde{E} = \tilde{E}(\mathbf{r}, t)$ and $E_q = E_q(\mathbf{r}, t)$, but here we take the shorter notation because all the fields will be functions of \mathbf{r} and t throughout this section.

The wavefunction of the system is

$$|\psi(t)\rangle = \sum_n C'_n e^{-i\omega_n t} |n\rangle, \quad (2.21)$$

where $n = a, b, j$. The amplitude C'_n obeys the Schrödinger equation:

$$i\hbar \dot{C}'_n = \sum_k e^{-i\omega_{nk}t} V_{nk} C'_k, \quad (2.22)$$

where $\omega_{nk} = \omega_n - \omega_k$. By making the transformation

$$C_a = C'_a, \quad C_b = C'_b e^{-i\delta t}, \quad C_j = C'_j, \quad (2.23)$$

Eq. (2.22) becomes

$$\dot{C}'_a = \frac{i}{2\hbar} \sum_j C'_j \mu_{aj} \left[\sum_q E_q e^{-i(\omega_{ja} + \omega_q)t} + \sum_q E_q^* e^{-i(\omega_{ja} - \omega_q)t} \right], \quad (2.24a)$$

$$\dot{C}'_b = -i\delta C'_b + \frac{i}{2\hbar} \sum_j C'_j \mu_{bj} \left[\sum_q E_q e^{-i(\omega_{jb} + \omega_q)t} + \sum_q E_q^* e^{-i(\omega_{jb} - \omega_q)t} \right], \quad (2.24b)$$

$$\begin{aligned} \dot{C}'_j = & \frac{i}{2\hbar} C'_a \mu_{ja} \left[\sum_q E_q e^{i(\omega_{ja} - \omega_q)t} + \sum_q E_q^* e^{i(\omega_{ja} + \omega_q)t} \right] \\ & + \frac{i}{2\hbar} C'_b \mu_{jb} \left[\sum_q E_q e^{i(\omega_{jb} - \omega_q)t} + \sum_q E_q^* e^{i(\omega_{jb} + \omega_q)t} \right], \end{aligned} \quad (2.24c)$$

Since $\omega_{jb} \pm \omega_q + \delta = \omega_{ja} \pm \omega_{q\mp 1}$, Eqs. (2.24) can be written in terms of ω_{ja} only:

$$\dot{C}'_a = \frac{i}{2\hbar} \sum_j C'_j \mu_{aj} \left[\sum_q E_q e^{-i(\omega_{ja} + \omega_q)t} + \sum_q E_q^* e^{-i(\omega_{ja} - \omega_q)t} \right], \quad (2.25a)$$

$$\dot{C}'_b = -i\delta C'_b + \frac{i}{2\hbar} \sum_j C'_j \mu_{bj} \left[\sum_q E_{q+1} e^{-i(\omega_{ja} + \omega_q)t} + \sum_q E_{q-1}^* e^{-i(\omega_{ja} - \omega_q)t} \right], \quad (2.25b)$$

$$\begin{aligned} \dot{C}_j = & \frac{i}{2\hbar} C_a \mu_{ja} \left[\sum_q E_q e^{i(\omega_{ja} - \omega_q)t} + \sum_q E_q^* e^{i(\omega_{ja} + \omega_q)t} \right] \\ & + \frac{i}{2\hbar} C_b \mu_{jb} \left[\sum_q E_{q-1} e^{i(\omega_{ja} - \omega_q)t} + \sum_q E_{q+1}^* e^{i(\omega_{ja} + \omega_q)t} \right], \end{aligned} \quad (2.25c)$$

Adiabatic elimination of C_j

Because of the far-off-resonance condition, we assume that for all times the upper levels j are in steady state. Therefore in the Schrödinger equation (2.25), we perform adiabatic elimination of C_j by first integrating Eq. (2.25c):

$$\begin{aligned} C_j = & \frac{i}{2\hbar} \int_{-\infty}^t \left[\sum_q e^{i(\omega_{ja} - \omega_q)t'} (C_a \mu_{ja} E_q + C_b \mu_{jb} E_{q-1}) \right] dt' \\ & + \frac{i}{2\hbar} \int_{-\infty}^t \left[\sum_q e^{i(\omega_{ja} + \omega_q)t'} (C_a \mu_{ja} E_q^* + C_b \mu_{jb} E_{q+1}^*) \right] dt'. \end{aligned}$$

Compared with $e^{i(\omega_{ja} \pm \omega_q)t}$, C_a , C_b and E_q vary slowly in time so they can be taken out of the integral:

$$\begin{aligned} C_j = & \frac{1}{2\hbar} \sum_q \frac{e^{i(\omega_{ja} - \omega_q)t}}{\omega_{ja} - \omega_q} (C_a \mu_{ja} E_q + C_b \mu_{jb} E_{q-1}) \\ & + \frac{1}{2\hbar} \sum_q \frac{e^{i(\omega_{ja} + \omega_q)t}}{\omega_{ja} + \omega_q} (C_a \mu_{ja} E_q^* + C_b \mu_{jb} E_{q+1}^*). \end{aligned} \quad (2.26)$$

Substituting C_j into Eq. (2.25a) and (2.25b) and dropping all the fast oscillating terms (slowly-varying amplitude approximation), we get

$$\begin{aligned} \dot{C}_a = & \frac{i}{(2\hbar)^2} C_a \sum_q \sum_j |\mu_{aj}|^2 |E_q|^2 \left(\frac{1}{\omega_{ja} - \omega_q} + \frac{1}{\omega_{ja} + \omega_q} \right) \\ & + \frac{i}{(2\hbar)^2} C_b \sum_q \sum_j \mu_{aj} \mu_{jb} E_q E_{q+1}^* \left(\frac{1}{\omega_{jb} - \omega_q} + \frac{1}{\omega_{ja} + \omega_q} \right), \end{aligned} \quad (2.27a)$$

$$\begin{aligned} \dot{C}_b = & -i\delta C_b + \frac{i}{(2\hbar)^2} C_a \sum_q \sum_j \mu_{bj} \mu_{ja} E_q E_{q+1}^* \left(\frac{1}{\omega_{jb} - \omega_q} + \frac{1}{\omega_{ja} + \omega_q} \right) \\ & + \frac{i}{(2\hbar)^2} C_b \sum_q \sum_j |\mu_{bj}|^2 |E_q|^2 \left(\frac{1}{\omega_{jb} - \omega_q} + \frac{1}{\omega_{jb} + \omega_q} \right), \end{aligned} \quad (2.27b)$$

where we have used

$$\begin{aligned} \omega_{ja} - \omega_q &= \omega_{jb} - \omega_{q-1} + \delta \approx \omega_{jb} - \omega_{q-1}, \\ \omega_{ja} + \omega_q &= \omega_{jb} + \omega_{q+1} + \delta \approx \omega_{jb} + \omega_{q+1}. \end{aligned} \quad (2.28)$$

Eqs. (2.27) can be written as a simple form.

$$\frac{d}{dt} \begin{pmatrix} C_a \\ C_b \end{pmatrix} = i \begin{pmatrix} \Omega_{aa} & \Omega_{ab} \\ \Omega_{ab}^* & \Omega_{bb} - \delta \end{pmatrix} \begin{pmatrix} C_a \\ C_b \end{pmatrix}, \quad (2.29)$$

where we have introduced the Stark shifts

$$\Omega_{aa} = \frac{1}{2} \sum_q a_q |E_q|^2, \quad (2.30a)$$

$$\Omega_{bb} = \frac{1}{2} \sum_q b_q |E_q|^2, \quad (2.30b)$$

and the two-photon Rabi frequency

$$\Omega_{ab} = \frac{1}{2} \sum_q d_q E_q E_{q+1}^*. \quad (2.31)$$

The constants a_q , b_q and d_q , with units of $[\text{m}^2 \cdot \text{V}^{-2} \cdot \text{s}^{-1}]$, are related to the dipole moments and the single-photon detunings:

$$a_q = \frac{1}{2\hbar^2} \sum_j |\mu_{aj}|^2 \left(\frac{1}{\omega_{ja} - \omega_q} + \frac{1}{\omega_{ja} + \omega_q} \right), \quad (2.32a)$$

$$b_q = \frac{1}{2\hbar^2} \sum_j |\mu_{bj}|^2 \left(\frac{1}{\omega_{jb} - \omega_q} + \frac{1}{\omega_{jb} + \omega_q} \right), \quad (2.32b)$$

$$d_q = \frac{1}{2\hbar^2} \sum_j \mu_{aj} \mu_{jb} \left(\frac{1}{\omega_{jb} - \omega_q} + \frac{1}{\omega_{ja} + \omega_q} \right). \quad (2.32c)$$

Density-matrix equations

The density-matrix equations can be obtained from Eq. (2.29). The density-matrix elements are defined by:

$$\tilde{\rho}_{ab} = C'_a e^{-i\omega_a t} \cdot C'_b{}^* e^{i\omega_b t} = C_a C_b{}^* e^{i\omega_m t} = \rho_{ab} e^{i\omega_m t}, \quad (2.33a)$$

$$\tilde{\rho}_{aa} = |C_a|^2 = \rho_{aa}, \quad (2.33b)$$

$$\tilde{\rho}_{bb} = |C_b|^2 = \rho_{bb}. \quad (2.33c)$$

Then from Eq. (2.29),

$$\dot{\rho}_{aa} = i(\Omega_{ab}\rho_{ba} - \Omega_{ba}\rho_{ab}) + \Gamma_{ba}\rho_{bb}, \quad (2.34a)$$

$$\dot{\rho}_{bb} = -i(\Omega_{ab}\rho_{ba} - \Omega_{ba}\rho_{ab}) - \Gamma_{ba}\rho_{bb}, \quad (2.34b)$$

$$\dot{\rho}_{ab} = i(\Omega_{aa} - \Omega_{bb} + \delta)\rho_{ab} + i\Omega_{ab}(\rho_{bb} - \rho_{aa}) - \gamma_{ab}\rho_{ab}, \quad (2.34c)$$

where the phenomenological damping has been included: Γ_{ba} is a population decay rate from level b to a and γ_{ab} is a coherence dephasing rate. They both have the units of radians per second³.

We note that if we change the two-photon Rabi frequency to a single-photon Rabi frequency and ignore the relative Stark shift $\Omega_{aa} - \Omega_{bb}$, then Eqs. (2.34) are simply the density-matrix equations for a two-level atom in the presence of one optical field [13, page 200], where δ becomes the single-photon-detuning. In other words, the

Note that in this chapter, all the quantities associated with frequency or rate are with angular frequency. For example, these quantities: ω_{ja} , Ω_{ab} , δ , and γ_{ab} , etc., all have the units of rad/sec.

adiabatic elimination of the upper levels j simplifies our system to an effective two-level problem.

The polarization

The polarization density $\tilde{P} = \tilde{P}(\mathbf{r}, t)$ in Eq.(2.3) is defined by

$$\tilde{P} = N \text{tr}(\tilde{\rho}\mu) = N \sum_j (\mu_{ja}\tilde{\rho}_{aj} + \mu_{aj}\tilde{\rho}_{ja} + \mu_{jb}\tilde{\rho}_{bj} + \mu_{bj}\tilde{\rho}_{jb}), \quad (2.35)$$

where N is the atomic density and the density matrix elements $\tilde{\rho}_{aj}$ and $\tilde{\rho}_{bj}$ are defined by, similar to Eq. (2.33a),

$$\tilde{\rho}_{aj} = C'_a e^{-i\omega_a t} \cdot C'_j{}^* e^{i\omega_j t} = C_a C_j^* e^{-i\omega_{aj} t}, \quad (2.36)$$

$$\tilde{\rho}_{bj} = C'_b e^{-i\omega_b t} \cdot C'_j{}^* e^{i\omega_j t} = C_b C_j^* e^{-i(\omega_{bj} - \delta)t}. \quad (2.37)$$

By substituting Eq. (2.26) into Eq. (2.35) and using Eq. (2.28) we find in the expansion Eq.(2.3),

$$P_q(\mathbf{r}, t) = 2N\hbar(a_q \rho_{aa} E_q + b_q \rho_{bb} E_q + d_{q-1} \rho_{ba} E_{q-1} + d_q^* \rho_{ab} E_{q+1}). \quad (2.38)$$

With Eqs. (2.14), (2.34), and (2.38), we are now ready to solve for the far-off-resonance intracavity Raman process.

The Stokes Laser

In this section, as illustrated in Fig. 3, we consider only two fields: $q = 0$ for the pump and $q = -1$ for the first-order Stokes. We use the subscripts p and s to denote the “pump” and the “Stokes” respectively.

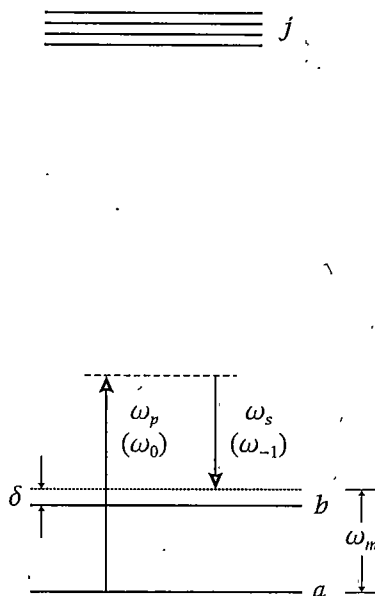


Figure 3 Energy levels and laser fields for the Stokes laser. Level a is the ground state; level b can be either a vibrational state or a rotational state; levels denoted by j are multiple excited electronic states. The pump field ω_p ($q = 0$) is red-shifted to the Stokes field ω_s ($q = -1$) and a molecular coherence $\rho_{ab}e^{i\omega_m t}$ is established between levels a and b . There can be a two-photon detuning denoted by δ .

Population and coherence

Because of the far-off-resonance condition, we can neglect the population on the upper levels j ⁴. Therefore we assume

$$\rho_{aa} + \rho_{bb} = 1. \quad (2.39)$$

Define $D = \rho_{bb} - \rho_{aa}$ to be the population difference between levels b and a . By using

⁴ Specifically, this is due to $\Omega \ll \Delta$ in our system, where $\Omega \sim 10^{10}$ rad/sec is the single-photon Rabi frequency of either the pump or the Stokes field and $\Delta \sim 10^{16}$ rad/sec is the single-photon detuning. This can be understood by solving the "two-level atom with one field" problem, which is given in many quantum optics textbooks. See, for example, Boyd [13], Eq.(5.3.11), when $\Omega \ll \Delta$ is satisfied, almost no population can be excited to the upper level.

Eq. (2.39), the density matrix equations (2.34) can be written as

$$\dot{D} = -2i(\Omega_{ab}\rho_{ba} - \Omega_{ba}\rho_{ab}) - \Gamma_{ba}(D - D^{eq}), \quad (2.40a)$$

$$\dot{\rho}_{ab} = -[\gamma_{ab} - i(\Omega_{aa} - \Omega_{bb} + \delta)]\rho_{ab} + i\Omega_{ab}D, \quad (2.40b)$$

where the Stark shifts Ω_{aa} and Ω_{bb} have been given by Eq. (2.30):

$$\Omega_{aa} = \frac{1}{2}(a_p|E_p|^2 + a_s|E_s|^2), \quad (2.41a)$$

$$\Omega_{bb} = \frac{1}{2}(b_p|E_p|^2 + b_s|E_s|^2), \quad (2.41b)$$

and the two-photon Rabi frequency [given by Eq. (2.31)]

$$\Omega_{ab} = \frac{d_s}{2}E_s(\mathbf{r}, t)E_p^*(\mathbf{r}, t) \quad (2.42)$$

contains the pump and Stokes fields which drive the coherence ρ_{ab} . The dispersion constants $a_{p(s)}$ and $b_{p(s)}$ are defined by Eqs. (2.32a) and (2.32b):

$$a_{p(s)} = \frac{1}{2\hbar^2} \sum_j |\mu_{aj}|^2 \left(\frac{1}{\omega_{ja} - \omega_{p(s)}} + \frac{1}{\omega_{ja} + \omega_{p(s)}} \right), \quad (2.43a)$$

$$b_{p(s)} = \frac{1}{2\hbar^2} \sum_j |\mu_{bj}|^2 \left(\frac{1}{\omega_{jb} - \omega_{p(s)}} + \frac{1}{\omega_{jb} + \omega_{p(s)}} \right). \quad (2.43b)$$

The coupling constant d_s is defined by Eq. (2.32c):

$$d_s = \frac{1}{2\hbar^2} \sum_j \mu_{aj}\mu_{jb} \left(\frac{1}{\omega_{jb} - \omega_s} + \frac{1}{\omega_{ja} + \omega_s} \right). \quad (2.44)$$

We will take d_s to be a real number for simplicity. In Eq. (2.40a), we have included a population difference in thermal equilibrium denoted by D^{eq} [13, Page 196] and we assume $D^{eq} = -1$, i.e., all the population is in the ground state in thermal equilibrium.

At steady state, all the time derivatives are set to zero. Eqs. (2.40) can then be solved algebraically:

$$D = \frac{\Gamma_{ba} D^{eq} (\gamma_{ab}^2 + \delta^2)}{\Gamma_{ba} (\gamma_{ab}^2 + \delta^2) + 4|\Omega_{ab}|^2 \gamma_{ab}}, \quad (2.45a)$$

$$\rho_{ab} = \frac{i\Omega_{ab} D}{\gamma_{ab} - i(\Omega_{aa} - \Omega_{bb} + \delta)}. \quad (2.45b)$$

We can estimate steady-state values of the population difference D and the coherence amplitude $|\rho_{ab}|$ in the cw Raman lasers. At room temperature, for the pure vibrational $v = 0 \rightarrow 1$ transition in 10 atm H_2 , the population decay rate $\Gamma_{ba} \approx 2\pi \times 1 \times 10^4$ rad/s [29] and the Raman gain linewidth (HWHM) $\gamma_{ab} \approx 2\pi \times 250 \times 10^6$ rad/s [3]. The constants $a_{p(s)}$, $b_{p(s)}$, and d_s have been calculated by Fam Le Kien et al [28]: $a_p \approx a_s \approx 2.6 \times 10^{-7}$, $b_p \approx b_s \approx 2.8 \times 10^{-7}$, and $d_s \approx 6.1 \times 10^{-8}$, in the SI units (i.e., $\text{m}^2 \cdot \text{V}^{-2} \cdot \text{s}^{-1}$). If we assume that the input pump power is 10 mW and both the cavity mirrors have a reflectance of 0.9999, then the intracavity spatial peak pump power is approximately 28 W. Converting this intracavity power to field amplitude and assuming the Stokes field has the same intracavity amplitude, we calculate that the Stark shifts $\Omega_{aa} \approx 1.0 \times 10^5$ rad/s, $\Omega_{bb} \approx 1.1 \times 10^5$ rad/s, and the two-photon Rabi frequency $\Omega_{ab} \approx 1.2 \times 10^4$ rad/s. Using all these data, we obtain that for the vibrational Raman laser and at the gain line center ($\delta = 0$),

$$D \approx -0.99996, \quad (2.46a)$$

$$|\rho_{ab}| \approx 8 \times 10^{-6}. \quad (2.46b)$$

This calculation shows that, because of $\Gamma_{ba}\gamma_{ab} \gg \Omega_{ab}^2$, the population for the cw

Raman laser can be considered undepleted from the ground state a (or $D \approx D^{eq}$) and therefore we can ignore the population equation (2.40a) for the later theoretical work. This calculation also tells us that, because of $\gamma_{ab} \gg \Omega_{ab}$, the coherence ρ_{ab} has a very small amplitude, far from the region of electromagnetically induced transparency [30], in which the coherence can be built up to its maximum value of 0.5 [26].

Polarization and Raman gain

In the two-field condition, Eq.(2.38) now becomes

$$P_p(\mathbf{r}, t) = 2N\hbar[(a_p\rho_{aa} + b_p\rho_{bb})E_p(\mathbf{r}, t) + d_s\rho_{ba}(\mathbf{r}, t)E_s(\mathbf{r}, t)], \quad (2.47a)$$

$$P_s(\mathbf{r}, t) = 2N\hbar[(a_s\rho_{aa} + b_s\rho_{bb})E_s(\mathbf{r}, t) + d_s\rho_{ab}(\mathbf{r}, t)E_p(\mathbf{r}, t)], \quad (2.47b)$$

where, as given by Eq.(2.12),

$$E_{p(s)}(\mathbf{r}, t) = E_{p(s)}(t)u_{p(s)}(\mathbf{r}). \quad (2.48)$$

Before we derive the intracavity field equations, let's first connect ρ_{ab} to some real physical quantities. Substituting (2.45b) into (2.47b), we obtain

$$P_s = 2N\hbar(a_s\rho_{aa} + b_s\rho_{bb})E_s + i\frac{N\hbar d_s^2 D}{\gamma_{ab} - i(\Omega_{aa} - \Omega_{bb} + \delta)}|E_p|^2 E_s. \quad (2.49)$$

Since $\rho_{aa} \approx 1$ and $\rho_{bb} \approx 0$, and $\Omega_{aa} \approx \Omega_{bb}$ (i.e., we ignore the population on level b and the relative Stark shift $\Omega_{aa} - \Omega_{bb}$), the Stokes polarization has the form

$$P_s = 2N\hbar a_s E_s + i\frac{N\hbar d_s^2 D}{\gamma_{ab} - i\delta}|E_p|^2 E_s. \quad (2.50)$$

Comparing with the definition [31, Page 471]

$$P_s = \epsilon_0\chi^{(1)}E_s - \epsilon_0\chi^{(3)}|E_p|^2 E_s, \quad (2.51)$$

where $\chi^{(1)}$, the linear susceptibility, is associated with the refractive index change caused by the single-photon-induced dispersion in the medium by the form

$$n_s = \sqrt{1 + \chi^{(1)}} \approx 1 + \frac{\chi^{(1)}}{2}, \quad (2.52)$$

we obtain

$$n_s \approx 1 + N\hbar a_s / \epsilon_0. \quad (2.53)$$

The $\chi^{(3)}$ in the second term of Eq. (2.51) is the complex Raman nonlinear susceptibility. It can be split into real and imaginary parts in the form $\chi'_R - i\chi''_R$, where

$$\chi'_R = -\frac{N\hbar d_s^2 D \delta}{\epsilon_0 (\gamma_{ab}^2 + \delta^2)}, \quad (2.54a)$$

$$\chi''_R = -\frac{N\hbar d_s^2 D \gamma_{ab}}{\epsilon_0 (\gamma_{ab}^2 + \delta^2)}. \quad (2.54b)$$

To see the physical roles of χ'_R and χ''_R , we note from Eq. (2.14) that the Stokes field is driven by a term proportional to iP_s . Therefore the two-photon (Raman) induced dispersion is reflected by the real part χ'_R ; while the Raman plane-wave gain coefficient⁵ is proportional to the imaginary part of the Raman susceptibility [32, 33]:

$$\alpha_g = \frac{2\omega_s \chi''_R}{n_s n_p c^2 \epsilon_0} = \frac{2\omega_s N \hbar d_s^2 (-D) \gamma_{ab}}{n_s n_p c^2 \epsilon_0 (\gamma_{ab}^2 + \delta^2)}. \quad (2.55)$$

5

For the case of SRS in free space, using the classical wave equation, one should obtain that the Stokes field experiences spatially exponential growth in the form [32]

$$\frac{\partial E_s}{\partial z} = \frac{\omega_s}{2cn_s} \chi''_R |E_p|^2 E_s = \frac{g_s}{2} E_s,$$

where g_s is the Stokes power gain. When the pump beam is a plane wave with uniform transverse intensity, the Stokes power gain per unit pump intensity g_s/I_s is defined as the plane-wave gain coefficient.

By substituting Eq.(2.45a), we can write α_g in the following form:

$$\alpha_g(\delta) = \alpha_g(0) \left(1 + \frac{4|\Omega_{ab}|^2}{\gamma_{ab}\Gamma_{ba}}\right)^{-1} \left(1 + \frac{\delta^2}{\gamma_{ab}^2} \frac{1}{1 + 4|\Omega_{ab}|^2/\gamma_{ab}\Gamma_{ba}}\right)^{-1}, \quad (2.56)$$

where

$$\alpha_g(0) = \frac{2\omega_s N \hbar d_s^2 (-D^{eq})}{n_s n_p c^2 \epsilon_0^2 \gamma_{ab}} \quad (2.57)$$

is the line center value of the unsaturated or small-signal plane-wave gain coefficient. This value is decreased by the factor $(1 + 4|\Omega_{ab}|^2/\gamma_{ab}\Gamma_{ba})^{-1}$, a phenomenon called saturation [13, page 203]. The last term in Eq. (2.56) indicates that the Raman gain has a Lorentzian lineshape with a FWHM linewidth of $2\gamma_{ab} \cdot \sqrt{1 + 4|\Omega_{ab}|^2/\gamma_{ab}\Gamma_{ba}}$. The small-signal linewidth $2\gamma_{ab}$ is broadened by the factor $\sqrt{1 + 4|\Omega_{ab}|^2/\gamma_{ab}\Gamma_{ba}}$, an effect called power broadening [13, page 202].

We can calculate the Raman plane-wave gain coefficient $\alpha_g(0)$ using Eq.(2.57). At a pressure of 10 atm and a temperature of 300 K, the hydrogen number density $N = 2.432 \times 10^{26} \text{ m}^{-3}$ [1, page 4-118]; for the pure vibrational $v = 0 \rightarrow 1$ transition, the Raman gain linewidth (HWHM) $\gamma_{ab} = 2\pi \times 250 \times 10^6 \text{ rad/s}$ [3]; the coupling constant $d_s \approx 6.1 \times 10^{-8} \text{ m}^2\text{Hz}/\text{V}^2$ [28]. By taking $n_s \approx n_p \approx 1$, $D^{eq} \approx -1$ and the Stokes wavelength of 1180 nm, we get $\alpha_{gv}(0) = 1.4 \times 10^{-11} \text{ m/W}$. Experimentally measured value of the Raman plane-wave gain coefficient for the vibrational transition pumped at 792 nm is $\alpha_{gv}(0) = 1.5 \times 10^{-11} \text{ m/W}$ [2]. Our theoretical calculation is very close to this value.

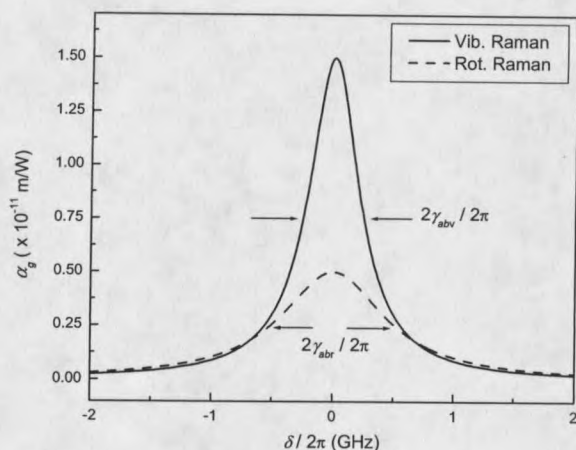


Figure 4 Raman plane-wave gain coefficient as a function of the two photon detuning. For the vibrational Raman transition (792→1180 nm, solid line), $\alpha_{gv}(0) = 1.5 \times 10^{-11}$ m/W [2], linewidth (HWHM) $\gamma_{abv}/2\pi = 250$ MHz [3]. For the rotational transition (792→830 nm, dashed line), $\alpha_{gr}(0) = 0.5 \times 10^{-11}$ m/W [4, 5, 6], linewidth (HWHM) $\gamma_{abr}/2\pi = 510$ MHz [7]. Gain and linewidth are for 10 atm H_2 at 300 K room temperature.

The gain saturation and linewidth broadening shown by Eq. (2.56) can also be estimated: the population decay rate $\Gamma_{ba}/2\pi$ is approximately 10 kHz [29]; the typical intracavity power of both the pump and Stokes is around 10 W. Then it can be calculated that the gain saturation factor is about 0.999997 and the linewidth broadening factor is about 1.000003. Both effects are small and thus negligible.

Intracavity field equations

Now we are ready to derive the intracavity field equations for the Stokes laser. We assume that the coherence establishes its steady-state value much faster than the intracavity fields (adiabatic following approximation [13, page 212]). Then the steady-state solution of ρ_{ab} , i.e., Eq.(2.45b), can be used for the field equations. We first obtain the polarization amplitudes at the pump and Stokes frequencies by

substituting Eq.(2.45b) to Eqs.(2.47):

$$P_p(\mathbf{r}, t) = 2N\hbar a_p \dot{E}_p(t) u_p(\mathbf{r}) - i \frac{N\hbar d_s^2 D}{\gamma_{ab} + i\delta} |E_s(t) u_s(\mathbf{r})|^2 E_p(t) u_p(\mathbf{r}), \quad (2.58a)$$

$$P_s(\mathbf{r}, t) = 2N\hbar a_s E_s(t) u_s(\mathbf{r}) + i \frac{N\hbar d_s^2 D}{\gamma_{ab} - i\delta} |E_p(t) u_p(\mathbf{r})|^2 E_s(t) u_s(\mathbf{r}), \quad (2.58b)$$

where we have ignored the population on level b (i.e., $\rho_{aa} \approx 1$ and $\rho_{bb} \approx 0$, or $D \approx -1$) as well as the relative Stark shift (i.e., $\Omega_{aa} - \Omega_{bb} \approx 0$). The continuous-wave Raman laser is a double-resonance laser system, i.e., both the pump and Stokes fields are resonant with the cavity. Thus both fields should observe the intracavity field equation (2.14), or

$$\begin{aligned} \dot{E}_p(t) + \left[\frac{\gamma_{cp}}{2} - i(\omega_p - \omega_{cp}) \right] E_p(t) &= \frac{\gamma_{ep}}{2} E_{ep}(t) \\ &+ i \frac{\omega_p}{2\epsilon_0} \frac{1}{V_p} \iiint_{\text{cavity}} dx dy dz P_p(\mathbf{r}, t) u_p^*(\mathbf{r}), \end{aligned} \quad (2.59a)$$

$$\dot{E}_s(t) + \left[\frac{\gamma_{cs}}{2} - i(\omega_s - \omega_{cs}) \right] E_s(t) = i \frac{\omega_s}{2\epsilon_0} \frac{1}{V_s} \iiint_{\text{cavity}} dx dy dz P_s(\mathbf{r}, t) u_s^*(\mathbf{r}). \quad (2.59b)$$

Substituting Eqs.(2.58) into (2.59), we obtain

$$\begin{aligned} \dot{E}_p(t) + \left[\frac{\gamma_{cp}}{2} - i(\omega_p - \omega_{cp}) \right] E_p(t) &= i\omega_p \frac{N\hbar a_p}{\epsilon_0} \frac{V_p}{V_p} E_p(t) \\ &+ \omega_p \frac{N\hbar d_s^2 D}{2\epsilon_0} \frac{1}{\gamma_{ab} + i\delta} \frac{V_{ps}}{V_p} |E_s(t)|^2 E_p(t) + \frac{\gamma_{ep}}{2} E_{ep}(t), \end{aligned} \quad (2.60a)$$

$$\begin{aligned} \dot{E}_s(t) + \left[\frac{\gamma_{cs}}{2} - i(\omega_s - \omega_{cs}) \right] E_s(t) &= i\omega_s \frac{N\hbar a_s}{\epsilon_0} \frac{V_s}{V_s} E_s(t) \\ &- \omega_s \frac{N\hbar d_s^2 D}{2\epsilon_0} \frac{1}{\gamma_{ab} - i\delta} \frac{V_{ps}}{V_s} |E_p(t)|^2 E_s(t), \end{aligned} \quad (2.60b)$$

where the cavity's single mode-volumes V_p and V_s and the two-field overlap mode-volume V_{ps} are given by

$$V_{p(s)} = \int_{-L/2}^{L/2} dz \int_0^\infty r dr \int_0^{2\pi} d\phi |u_{p(s)}|^2, \quad (2.61a)$$

$$V_{ps} = \int_{-L/2}^{L/2} dz \int_0^\infty r dr \int_0^{2\pi} d\phi |u_p|^2 |u_s|^2. \quad (2.61b)$$

In a stable two-mirror laser cavity of length L and in the TEM₀₀ spatial mode, $u_q(\mathbf{r})$ is of the form [32]

$$u_q(\mathbf{r}) = u_q(r, z) = \frac{1}{1 + i2z/b_q} e^{-r^2 k_q/b_q(1+i2z/b_q)} \sin(k_q z), \quad (2.62)$$

where $r^2 = x^2 + y^2$. Here k_q and b_q are the wave vector and the confocal parameter (twice the Rayleigh range) of the q -th field respectively.

With Eq.(2.62); noting that the confocal parameter b is the same for both the pump and the Stokes since it is only determined by the cavity's geometric property, we compute the above integrals to obtain

$$V_{p(s)} = 2\pi \frac{L}{8} \frac{b}{k_{p(s)}}, \quad (2.63a)$$

$$V_{ps} = 2\pi \frac{1}{16} \frac{b^2}{k_p + k_s} \tan^{-1} \left(\frac{L}{b} \right). \quad (2.63b)$$

Then Eqs.(2.60) become

$$\begin{aligned} \dot{E}_p(t) + \left\{ \frac{\gamma_{cp}}{2} - i \left[\left(\frac{N\hbar a_p}{\epsilon_0} + 1 \right) \omega_p - \omega_{cp} \right] \right\} E_p(t) = \frac{\gamma_{ep}}{2} E_{ep}(t) + \\ \frac{1}{4} \omega_p \frac{N\hbar d_s^2 D}{\epsilon_0} \frac{1}{\gamma_{ab} + i\delta} \frac{\lambda_s}{\lambda_p + \lambda_s} \frac{\tan^{-1}(L/b)}{L/b} |E_s(t)|^2 E_p(t), \end{aligned} \quad (2.64a)$$

$$\begin{aligned} \dot{E}_s(t) + \left\{ \frac{\gamma_{cs}}{2} - i \left[\left(\frac{N\hbar a_s}{\epsilon_0} + 1 \right) \omega_s - \omega_{cs} \right] \right\} E_s(t) = \\ \frac{1}{4} \omega_s \frac{N\hbar d_s^2 D}{\epsilon_0} \frac{1}{\gamma_{ab} - i\delta} \frac{\lambda_p}{\lambda_p + \lambda_s} \frac{\tan^{-1}(L/b)}{L/b} |E_p(t)|^2 E_s(t). \end{aligned} \quad (2.64b)$$

We can define a gain term

$$\begin{aligned} G(\delta) &= -\frac{1}{4}\omega_s \frac{N\hbar d_s^2 D}{\epsilon_0} \frac{\gamma_{ab}}{\gamma_{ab}^2 + \delta^2} \frac{\lambda_p}{\lambda_p + \lambda_s} \frac{\tan^{-1}(L/b)}{L/b} \\ &= \frac{1}{8}c^2 \epsilon_0 \alpha_g(\delta) \frac{\lambda_p}{\lambda_p + \lambda_s} \frac{\tan^{-1}(L/b)}{L/b}, \end{aligned} \quad (2.65)$$

where $\alpha_g(\delta)$ is the plane-wave gain coefficient given by Eq.(2.55). Eq.(2.65) has the same form as the gain defined by Brasseur[21, Eq.(3)] if

$$\frac{\tan^{-1}(L/b)}{L/b} \approx 1. \quad (2.66)$$

This relation is valid if the laser cavity's length is well within the confocal parameter (or twice the Rayleigh range) of the laser beam, so that the beam inside the cavity can be considered collimated. This is true for all the cw Raman lasers that have been demonstrated so far.

Eqs. (2.64) now has the form

$$\begin{aligned} \dot{E}_p(t) + \left[\frac{\gamma_{cp}}{2} - i(n_p \omega_p - \omega_{cp}) \right] E_p(t) &= \frac{\gamma_{ep}}{2} E_{ep}(t) + \\ &- \frac{\omega_p k_p}{\omega_s k_s} \left[G(\delta) - i \frac{\delta}{\gamma_{ab}} G(\delta) \right] |E_s(t)|^2 E_p(t), \end{aligned} \quad (2.67a)$$

$$\begin{aligned} \dot{E}_s(t) + \left[\frac{\gamma_{cs}}{2} - i(n_s \omega_s - \omega_{cs}) \right] E_s(t) &= \\ &\left[G(\delta) + i \frac{\delta}{\gamma_{ab}} G(\delta) \right] |E_p(t)|^2 E_s(t), \end{aligned} \quad (2.67b)$$

where the refractive indexes $n_p = 1 + N\hbar a_p / \epsilon_0$ and $n_s = 1 + N\hbar a_s / \epsilon_0$ [see Eq. (2.53)]

have been substituted.

Next the complex fields can be separated into their amplitudes and phases in the forms

$$\dot{E}_p(t) = |E_p(t)|e^{-i\phi_p(t)}, \quad E_{ep}(t) = |E_{ep}(t)|e^{-i\phi_p(t)}; \quad (2.68a)$$

$$E_s(t) = |E_s(t)|e^{-i\phi_s(t)}. \quad (2.68b)$$

Here we suppose that the intracavity pump field always has the same phase with the incident pump field. This is valid for the continuous-wave and single-frequency incident light whose phase change is slower than the cavity's response time. By substituting Eqs. (2.68) into (2.67), two sets of equations, one for the field amplitudes and one for their phases/frequencies, can be obtained.

Field amplitude equation and the steady-state oscillation condition

Substituting Eqs. (2.68) into (2.67), the real parts give the equations of motion for the pump and Stokes field amplitudes:

$$|\dot{E}_p(t)| + \frac{\gamma_{cp}}{2}|E_p(t)| = -\frac{\omega_p k_p}{\omega_s k_s}G(\delta)|E_s(t)|^2|E_p(t)| + \frac{\gamma_{ep}}{2}|E_{ep}(t)|, \quad (2.69a)$$

$$|\dot{E}_s(t)| + \frac{\gamma_{cs}}{2}|E_s(t)| = G(\delta)|E_p(t)|^2|E_s(t)|. \quad (2.69b)$$

We first give the steady-state solutions. At steady state, all the time derivatives are set to be zero. We solve Eqs.(2.69a) and (2.69b) algebraically to obtain that when the laser is above threshold,

$$|E_p|_{ss} = \sqrt{\frac{\gamma_{cs}}{2G(\delta)}}, \quad (2.70)$$

$$|E_s|_{ss} = \sqrt{\frac{\omega_s k_s \gamma_{ep}|E_{ep}|/|E_p|_{ss} - \gamma_{cp}}{\omega_p k_p 2G(\delta)}}. \quad (2.71)$$

When the numerator in Eq.(2.71) equals zero, the laser's threshold is found to be

$$|E_{ep}|_{\text{threshold}} = \frac{\gamma_{cp}}{\gamma_{ep}} |E_p|_{ss}. \quad (2.72)$$

In the non-steady-state regime, Eqs.(2.69a) and (2.69b) needs to be numerically solved. The results will be given in a later section, or can also be found in Ref. [21]. Here we only give a simple view of the Stokes transient growth by adopting a trial solution of the form

$$|E_s(t)| = |E_s(0)|e^{gt}, \quad (2.73)$$

where g represents an exponential growth rate for Stokes. We substitute this form into Eq. (2.69b) and find g satisfies

$$g = G(\delta)|E_p|^2 - \frac{\gamma_{cs}}{2}. \quad (2.74)$$

If $E_p = E_{p,ss} = \sqrt{\gamma_{cs}/2G(\delta)}$ then $g = 0$, and the laser will be running in the steady-state; however once $E_p > E_{p,ss}$ the Stokes light will experience exponential growth, which will deplete the pump until $E_p = E_{p,ss}$ is again satisfied. In other words, Eq. (2.70) can be viewed as the steady-state oscillation condition:

Saturated gain = Cavity loss;

$$G(\delta)|E_p|^2 = \frac{\gamma_{cs}}{2}. \quad (2.75)$$

This understanding will be helpful when we analyze the Stokes mode-hop hysteresis in a later chapter.

Frequency pulling

Substituting Eqs. (2.68) into (2.67), the imaginary parts give the frequency-determining equations:

$$\omega_p + \dot{\phi}_p = \omega_{cp} - (n_p - 1)\omega_p - \frac{\omega_p k_p}{\omega_s k_s} G(\delta) |E_s(t)|^2 \frac{\delta}{\gamma_{ab}}, \quad (2.76a)$$

$$\omega_s + \dot{\phi}_s = \omega_{cs} - (n_s - 1)\omega_s - G(\delta) |E_p(t)|^2 \frac{\delta}{\gamma_{ab}}. \quad (2.76b)$$

Since $\omega_p \approx \omega_{cp}$, we can rewrite the term $\omega_{cp} - (n_p - 1)\omega_p$ in Eq. (2.76a):

$$\begin{aligned} \omega_{cp} - (n_p - 1)\omega_p &\approx \omega_{cp}[1 - (n_p - 1)] \\ &\approx \frac{\omega_{cp}}{1 + (n_p - 1)} \\ &= \frac{\omega_{cp}}{n_p}. \end{aligned} \quad (2.77)$$

Similarly, $\omega_{cs} - (n_s - 1)\omega_s \approx \omega_{cs}/n_s$ ⁶ in Eq. (2.76b). By using these approximations and then substituting Eqs. (2.70) and (2.71), Eqs. (2.76) give that at steady-state and above threshold, the *required* oscillating frequencies are

$$\begin{aligned} \omega_p + \dot{\phi}_p &= \frac{\omega_{cp}}{n_p} + \frac{\delta \gamma_{cp}}{2 \gamma_{ab}} - \frac{\delta \gamma_{ep}}{2 \gamma_{ab}} \frac{|E_{ep}|}{|E_p|_{ss}} \\ &= \frac{\omega_{cp}}{n_p} + \left[1 - \sqrt{\mathcal{R}(\delta)}\right] \frac{\delta \gamma_{cp}}{2 \gamma_{ab}}, \end{aligned} \quad (2.78a)$$

$$\omega_s + \dot{\phi}_s = \frac{\omega_{cs}}{n_s} - \frac{\delta \gamma_{cs}}{2 \gamma_{ab}}, \quad (2.78b)$$

where $\sqrt{\mathcal{R}(\delta)} = |E_{ep}|/|E_{ep}|_{\text{threshold}}(\delta)$ is the field pumping rate which is a function of the two-photon-detuning. We first note that although the steady-state solution

⁶

When $|x| \ll 1$, $1 - x^2 \approx 1$, this is equivalent to $1 - x \approx 1/(1 + x)$. Here $x = n_{p(s)} - 1$.

means $d/dt \equiv 0$ for all amplitude quantities, steady state can still mean $d\phi/dt =$ constant [25, page 948], which means a constant frequency. Therefore, while the reference frequencies $\omega_{p(s)}$ were arbitrarily chosen when we derived the wave equations using the slowly varying envelope approximation in Section 2, Eqs. (2.78) reveal that the *required* oscillating frequencies $\omega_{p(s)} + \dot{\phi}_{p(s)}$ are different from the “cold” cavity resonant frequencies $\omega_{cp(s)}$. (We could choose $\omega_{p(s)} = \omega_{cp(s)}$ from the beginning, then $\dot{\phi}_{p(s)}$ will be the required frequency shifts or the amount of frequency-pulling).

The first term at the right-hand-side of Eq. (2.78a) or (2.78b) is the frequency-pulling due to the single-photon-induced dispersion. It simply means that the resonances of a vacuum cavity (ω_{cq}) should be modified if there is any medium inside the cavity (divided by medium’s refractive index n_q).

The second term proportional to the two-photon-detuning δ in Eqs. (2.78) is the frequency-pulling due to the Raman-induced dispersion. Let us estimate how large the Raman frequency-pulling is. For typical cw Raman lasers $\gamma_{cp,s}/2\pi \sim 0.01 - 1$ MHz and $\gamma_{ab}/2\pi$ is around several hundred MHz, the amount of pulling is in the range $(10^{-5} \sim 10^{-3}) \times \delta$. Usually the two-photon-detuning $\delta/2\pi$ is less than ± 1 GHz, so the amount of pulling is in the kHz range. Using Eqs. (2.78), we calculate the amounts of frequency-pulling in a real vibrational Raman laser and plot the results in Fig. 5.

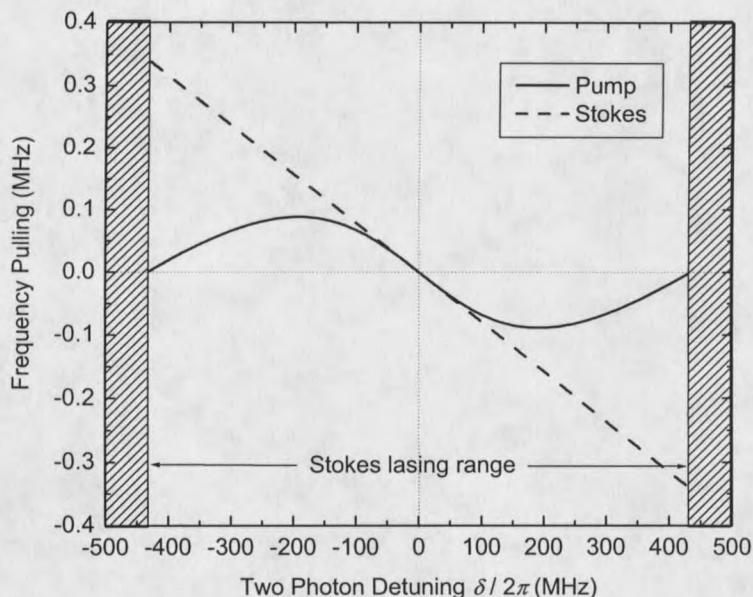


Figure 5 Theoretical calculation of the amount of frequency-pulling ϕ as a function of two-photon-detuning δ in a cw vibrational Raman laser. Solid line: pump; dashed line: Stokes. Parameters used are: $\lambda_p = 792$ nm; $\lambda_s = 1180$ nm; $\alpha_g = 1.5 \times 10^{-9}$ cm/W (line-center value for 10 atm H₂ at 25°C); mirror transmittance = 0.9999; mirror absorption = 30×10^{-6} ; cavity length = 7.62 cm; and pumping rate is at four times the line-center threshold. In the two shaded areas, the Stokes laser is below threshold.

In reality, the cavity is frequency-locked to the pump laser. Usually the pump laser is frequency tuned and the locking servos are able to follow and maintain the locking. Once the system is tuned off the line-center ($\delta \neq 0$), the PZT servo will find a ω_{cp} value to compensate the frequency-pulling in Eq. (2.78a), while the lasing Stokes frequency ω_s will adjust itself to satisfy Eq. (2.78b).

In terms of pump and Stokes powers

It is necessary to write the intracavity field equations in terms of measurable powers so that we can compare the experimental data with the theory. From Eqs. (2.12)

and (2.62) one can see that $E_q(t)$ represents the peak field-amplitude of the intracavity standing-wave in space (i.e., at the center of the TEM₀₀ transverse profile and at the antinodes of the standing-wave along the longitudinal direction). The intracavity light intensity (optical power per unit area, or power density, on the plane perpendicular to the z -axis) is calculated by [34, page 50]

$$I_q = \frac{v_q \epsilon_q}{2} |E_q(t) u_q(\mathbf{r})|^2, \quad (2.79)$$

where $v_q = c/n_q$ is the intracavity light speed and $\epsilon_q = n_q^2 \epsilon_0$ is the dielectric permeability of the intracavity medium. The intracavity power along the longitudinal direction can be calculated (we use Π to denote the intracavity power and use P to denote the power outside the cavity):

$$\begin{aligned} \Pi'_q(z, t) &= \int_0^\infty r dr \int_0^{2\pi} d\phi I_q \\ &= \frac{\pi w_{0q}^2 n_q}{4} \sqrt{\frac{\epsilon_0}{\mu_0}} |E_q(t)|^2 \frac{\sin^2(k_q z)}{1 + (2z/b_q)^2}, \end{aligned} \quad (2.80)$$

where $w_{0q} = \sqrt{b_q/k_q}$ is the radius at the beam waist. If the beam inside the cavity is collimated ($z \ll b_q$), the peak intracavity power along the longitudinal direction (at the antinode planes of the standing-wave) is given by

$$\begin{aligned} \Pi_q(t) &= \frac{\pi w_{0q}^2 n_q}{4} \sqrt{\frac{\epsilon_0}{\mu_0}} |E_q(t)|^2 \\ &= \frac{\pi b_q}{4 \omega_q \mu_0} |E_q(t)|^2. \end{aligned} \quad (2.81)$$

A standing-wave consists of two counter-propagating equal-amplitude traveling-waves and the peak-amplitude ratio between the standing and traveling waves is 2:1. Therefore the optical power of the traveling-waves (or so-called cavity circulating power) is

equal to $\frac{1}{4}\Pi_q(t)$.

Using the relation Eq. (2.81), one can convert Eqs. (2.69) into

$$\dot{\Pi}_p(t) + \gamma_{cp}\Pi_p(t) = -\frac{8\omega_p\mu_0 k_p}{\pi b k_s}G(\delta)\Pi_s(t)\Pi_p(t) + \gamma_{ep}\sqrt{\Pi_p(t)P_{ep}(t)}, \quad (2.82a)$$

$$\dot{\Pi}_s(t) + \gamma_{cs}\Pi_s(t) = \frac{8\omega_p\mu_0}{\pi b}G(\delta)\Pi_p(t)\Pi_s(t). \quad (2.82b)$$

The steady-state solutions are

$$\Pi_{p,ss} = \frac{\pi b}{4\omega_p\mu_0} \frac{\gamma_{cs}}{2G(\delta)}, \quad (2.83)$$

$$\Pi_{s,ss} = \frac{\pi b}{4\omega_p\mu_0} \frac{k_s}{k_p} \frac{1}{2G(\delta)} \left[\gamma_{ep}\sqrt{\frac{P_{ep}}{\Pi_{p,ss}}} - \gamma_{cp} \right]. \quad (2.84)$$

The threshold pump power is given by

$$P_{ep,th} = \left(\frac{\gamma_{cp}}{\gamma_{ep}} \right)^2 \Pi_{p,ss} = \frac{(\ln \sqrt{R_{1p}R_{2p}})^2}{4T_{1p}} \Pi_{p,ss} \quad (2.85)$$

Note again that $\Pi_p(t)$ and $\Pi_s(t)$ are the peak intracavity powers along the longitudinal direction (at the antinodes of the standing-wave). Because the cavity circulating power is equal to $\frac{1}{4}\Pi_q(t)$, the time-averaged powers measured just outside the cavity mirrors take the following forms [23, 21]:

$$\text{Reflected pump : } P_{1p} = R_{1p}P_{ep} + \frac{1}{4}T_{1p}\Pi_p - \sqrt{R_{1p}P_{ep}}\sqrt{T_{1p}\Pi_p}, \quad (2.86a)$$

$$\text{Transmitted pump : } P_{2p} = \frac{1}{4}T_{2p}\Pi_p, \quad (2.86b)$$

$$\text{Front Stokes : } P_{1s} = \frac{1}{4}T_{1s}\Pi_s, \quad (2.86c)$$

$$\text{Back Stokes : } P_{2s} = \frac{1}{4}T_{2s}\Pi_s. \quad (2.86d)$$

Here “front” means the side at which the pump laser enters the cavity; then the other side of the cavity is named “back”. The first equation shows that the total reflected pump field is an interference between the first reflection and the cavity leakage field.

Numerical time-dependent solution

For the time-dependent solution to the cw Stokes laser, we choose to numerically solve the complex field equations (2.67) using MATHEMATICA. [35] (The code is given in Appendix B). This work was first done by Brasseur [23, 21].

We numerically solve Eqs (2.67) for the vibrational transition of 792→1180 nm. Therefore the gain and the linewidth used are $\alpha_g = 1.5 \times 10^{-9} \text{cm/W}$ (line-center value for 10 atm H_2 at 25°C)[2] and $\gamma_{abv}/2\pi = 250 \text{ MHz}$ (HWHM; for 10 atm H_2 at 25°C)[3]. The following cavity parameters are used: $R = 0.9999$ (mirror reflectance) and $A = 30 \times 10^{-6}$ (mirrors’ power loss) for both mirrors at both wavelengths; $L = 7.62 \text{ cm}$ (cavity length); $r = 50 \text{ cm}$ (mirrors’ radius of curvature) for both mirrors. In addition, we choose the reference frequency $\omega_{p(s)} = \omega_{cp(s)}/n_{p(s)}$ to simplify the calculation.

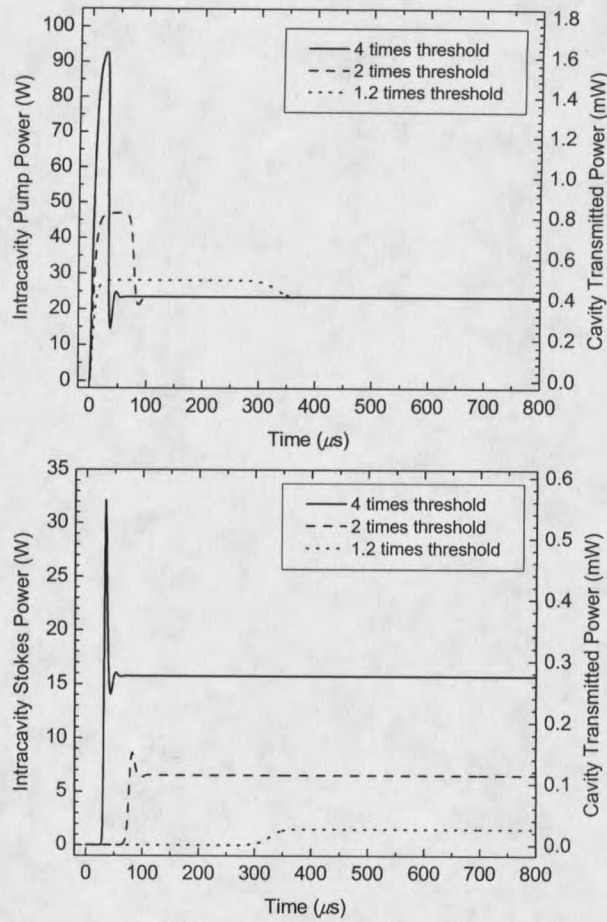


Figure 6 Numerical simulation of the “turn-on” behavior in a cw vibrational Raman laser at different pumping rates. The pump (top) and the Stokes (bottom) powers are plotted as functions of time. The solid line is at a pumping rate of 4 times the threshold; the dashed line is at 2 times the threshold; and the dotted line is at 1.2 times the threshold. All the curves are at the Raman gain line-center (i.e., the two-photon-detuning $\delta = 0$). The left horizontal axis is the intracavity spatial peak power and the right axis is the cavity transmitted power (single end).

The first time-dependent result is given in Fig. 6. The field amplitudes of the pump and the Stokes are numerically calculated as functions of time. We then convert them into optical powers using Eq. (2.81). Three cases of different pumping rates (all on the Raman resonance) are calculated and plotted. It can be seen that at low pumping rate of 1.2 times the threshold, the laser turns on smoothly and slowly with

nearly no relaxation oscillations; whereas at 4 times the threshold, there is a large overshoot followed by some oscillations.

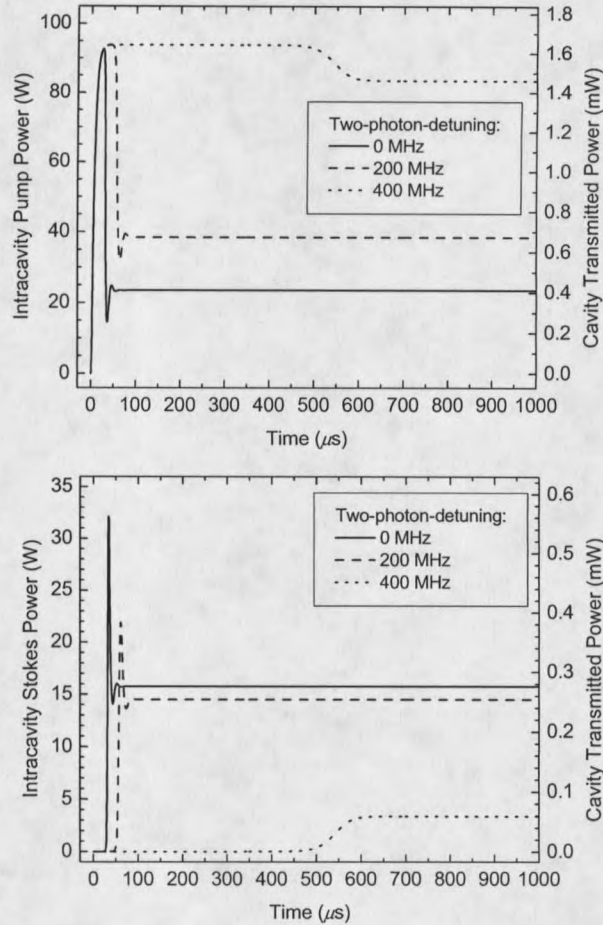


Figure 7 Numerical simulation of the “turn-on” behavior in a cw vibrational Raman laser at different detunings. The pump (top) and the Stokes (bottom) powers are plotted as functions of time. The solid line is when the two-photon-detuning $\delta/2\pi = 0$; the dashed line is when $\delta/2\pi = 200$ MHz; and the dotted line is when $\delta/2\pi = 400$ MHz. All the curves are at the pumping rate of 4 times the line-center threshold. The left horizontal axis is the intracavity spatial peak power and the right axis is the cavity transmitted power (single end).

Fig. 7 gives another comparison of the “turn-on” behaviors. This time, while the input pump power is fixed at 4 times the line-center threshold, the field amplitudes

are calculated at three different two-photon-detunings. Similar to Fig. 6, as the laser is detuned away from the Raman resonance by 400 MHz, it starts smoothly and slowly due to the weaker pumping rate (the threshold increases as detuned away); whereas as the laser is on or near the Raman resonance (now it is pumped harder), there are dramatic dynamics before steady state is achieved.

Fig. 6 and Fig. 7 explain our experimental experiences. If the pumping rate is high, it is difficult to stabilize the pump laser to the cavity because of the dramatic turn-on dynamics of the Stokes generation. The way to make the cw Raman laser run is to lock the pump laser and the cavity together at the low pumping rate or even below the threshold. Then the steady-state lasing can be approached at high pumping rates by slowly increasing the pump power or tuning to the line-center.

It is interesting to note that, when we numerically solve the differential field equations, an initial condition of nonzero Stokes power must be chosen to make the Stokes laser oscillate. This can be viewed as the requirement of the stimulated Raman scattering: some seeding Stokes photons are necessary for the Stokes amplification. In our cw Raman laser, the Stokes oscillation is "self-seeded" from the spontaneous Raman scattering. In the above numerical solutions, we have chosen the circulating power in a single-photon cavity (~ 0.3 nW) as the initial condition.

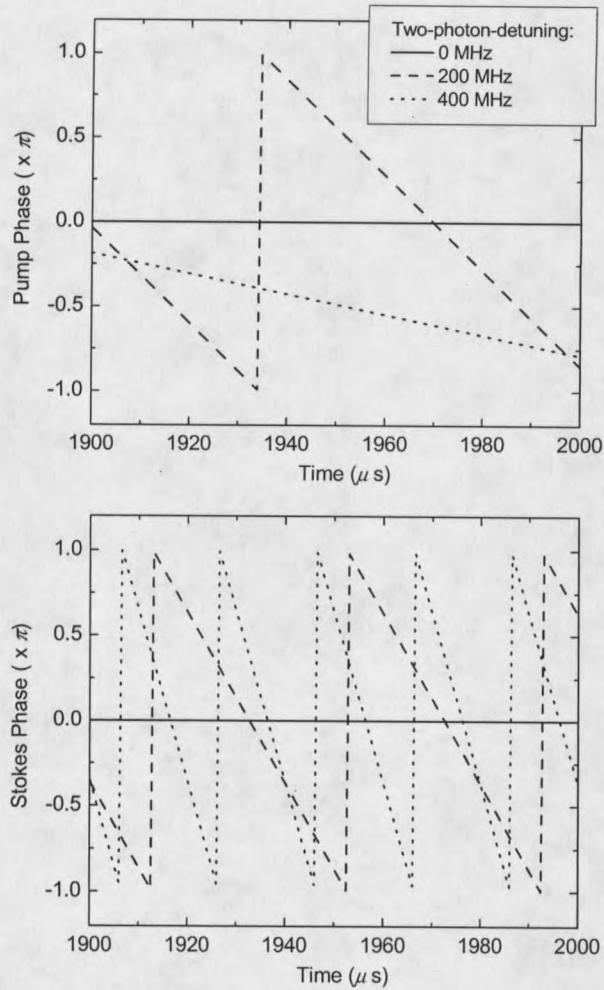


Figure 8 After the cw Raman laser in Fig. 7 grows into steady-state (note the horizontal time scale), the calculated phase evolutions of the pump (top) and the Stokes (bottom) beams are shown for different detunings. The slope of the phase curve gives the amount of frequency-pulling.

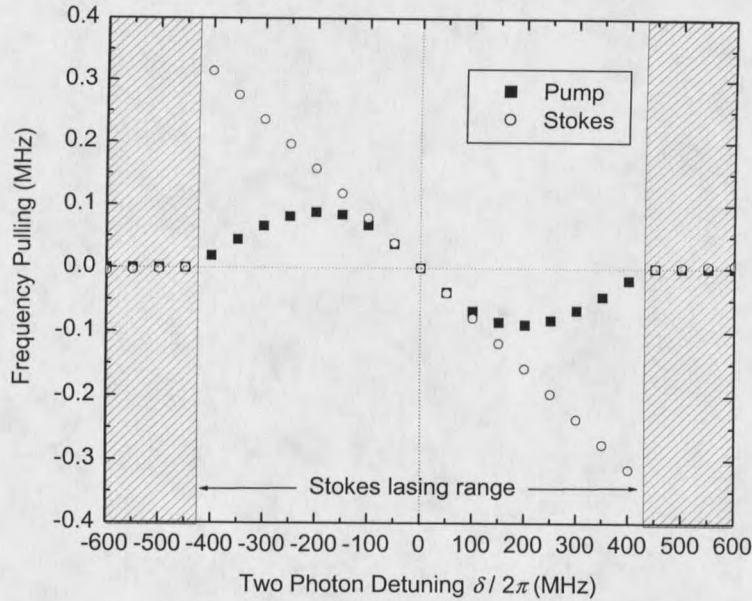


Figure 9 The slopes of the phase curves in Fig. 7 as functions of the two-photon-detunings. This numerical calculation agrees with the theoretical plot in Fig. 5.

Numerically solving the complex field equations (2.67) can also give the phase dynamics of the pump and the Stokes fields. Fig. 8 shows that at steady-state, if the two-photon-detuning is zero, the phases of the two fields are constantly zero with time, meaning $\omega_{p(s)} = \omega_{cp(s)}/n_{p(s)}$ or no frequency pulling caused by the two-photon dispersion. However, if the Stokes resonance is detuned away from the Raman line-center, the phases of both the pump and Stokes fields change linearly with time, or $\dot{\phi}_{p(s)} = \text{constant}$, in steady state. The slope of the phase curve $\dot{\phi}_{p(s)}$ gives the amount of frequency-pulling. Clearly, Fig. 8 shows that this slope is dependent on the two-photon-detuning. We numerically calculate the slope at different two-photon-detunings and plot the dependence in Fig. 9. We obtained the same result from the analytic steady-state solutions plotted in Fig. 5. This agreement proves the

correctness of our numerical time-dependent solutions.

The Anti-Stokes Emission

We consider three fields in this section: $q = 0$ (pump), $q = -1$ (Stokes), and $q = 1$ (anti-Stokes), as exactly shown in Fig. 2. In this situation, besides the two-photon Raman interactions, there also exists a four-wave mixing process, by which the Stokes and anti-Stokes fields can be strongly coupled. To develop the theory, we assume a triple-resonance condition (i.e., all the three fields are resonant with the cavity), although in reality this condition will be experimentally difficult due to dispersion effects. At the end of this section we will estimate the dispersion and discuss the methods to compensate it.

Complex field equations

Using the subscripts p , s , and a to represent the pump, Stokes, and anti-Stokes fields respectively, from Eq. (2.14) we have three field equations:

$$\begin{aligned} \dot{E}_p(t) + \left[\frac{\gamma_{cp}}{2} - i(\omega_p - \omega_{cp}) \right] E_p(t) = \frac{\gamma_{ep}}{2} E_{ep}(t) \\ + i \frac{\omega_p}{2\epsilon_0 V_p} \iiint_{\text{cavity}} dx dy dz P_p(\mathbf{r}, t) u_p^*(\mathbf{r}), \end{aligned} \quad (2.87a)$$

$$\dot{E}_s(t) + \left[\frac{\gamma_{cs}}{2} - i(\omega_s - \omega_{cs}) \right] E_s(t) = i \frac{\omega_s}{2\epsilon_0 V_s} \iiint_{\text{cavity}} dx dy dz P_s(\mathbf{r}, t) u_s^*(\mathbf{r}), \quad (2.87b)$$

$$\dot{E}_a(t) + \left[\frac{\gamma_{ca}}{2} - i(\omega_a - \omega_{ca}) \right] E_a(t) = i \frac{\omega_a}{2\epsilon_0 V_a} \iiint_{\text{cavity}} dx dy dz P_a(\mathbf{r}, t) u_a^*(\mathbf{r}). \quad (2.87c)$$

The three polarization terms are given by Eq. (2.38):

$$P_p(\mathbf{r}, t) = 2N\hbar [a_p E_p(t) u_p(\mathbf{r}) + d_0 \rho_{ba}(\mathbf{r}, t) E_s(t) u_s(\mathbf{r}) + d_0 \rho_{ab}(\mathbf{r}, t) E_a(t) u_a(\mathbf{r})], \quad (2.88a)$$

$$P_s(\mathbf{r}, t) = 2N\hbar [a_s E_s(t) u_s(\mathbf{r}) + d_0 \rho_{ab}(\mathbf{r}, t) E_p(t) u_p(\mathbf{r})], \quad (2.88b)$$

$$P_a(\mathbf{r}, t) = 2N\hbar [a_a E_a(t) u_a(\mathbf{r}) + d_0 \rho_{ba}(\mathbf{r}, t) E_p(t) u_p(\mathbf{r})], \quad (2.88c)$$

where we have made the approximation that $d_p \approx d_s \approx d_0$ and both d 's are real. We again take the fact that the population is nearly undepleted from the ground state so that the population equation (2.40a) can be dropped. The steady-state coherence Eq. (2.45b) now has the form

$$\begin{aligned} \rho_{ab} &= \frac{i\Omega_{ab}D}{\gamma_{ab} - i\delta} \\ &= i\frac{d_0}{2}D \frac{E_s(t)u_s(\mathbf{r})E_p^*(t)u_p^*(\mathbf{r}) + E_p(t)u_p(\mathbf{r})E_a^*(t)u_a^*(\mathbf{r})}{\gamma_{ab} - i\delta}, \end{aligned} \quad (2.89)$$

where the relative Stark shift, $\Omega_{aa} - \Omega_{bb}$ has been ignored. With Eqs. (2.88) and (2.89) (again using the adiabatic following approximation), Eqs. (2.87) become

$$\begin{aligned} \dot{E}_p + \left[\frac{\gamma_{cp}}{2} - i(\omega_p - \omega_{cp}) \right] E_p &= \frac{\gamma_{ep}}{2} E_{ep} + i\omega_p \frac{N\hbar a_p V_p}{\epsilon_0 V_p} E_p \\ &+ \omega_p \frac{N\hbar d_0^2 D}{2\epsilon_0} \frac{1}{\gamma_{ab} + i\delta} \frac{1}{V_p} (V_{ps} |E_s|^2 E_p + V_{\text{FWM}} E_p^* E_s E_a) \\ &- \omega_p \frac{N\hbar d_0^2 D}{2\epsilon_0} \frac{1}{\gamma_{ab} - i\delta} \frac{1}{V_p} (V_{pa} |E_a|^2 E_p + V_{\text{FWM}} E_p^* E_s E_a), \end{aligned} \quad (2.90a)$$

$$\begin{aligned} \dot{E}_s + \left[\frac{\gamma_{cs}}{2} - i(\omega_s - \omega_{cs}) \right] E_s &= i\omega_s \frac{N\hbar a_s V_s}{\epsilon_0 V_s} E_s \\ &- \omega_s \frac{N\hbar d_0^2 D}{2\epsilon_0} \frac{1}{\gamma_{ab} - i\delta} \frac{1}{V_s} (V_{ps} |E_p|^2 E_s + V_{\text{FWM}} E_p E_p^* E_a), \end{aligned} \quad (2.90b)$$

$$\begin{aligned} \dot{E}_a + \left[\frac{\gamma_{ca}}{2} - i(\omega_a - \omega_{ca}) \right] E_a = i\omega_a \frac{N\hbar a_a}{\epsilon_0} \frac{V_a}{V_a} E_a \\ + \omega_a \frac{N\hbar d_0^2 D}{2\epsilon_0} \frac{1}{\gamma_{ab} + i\delta} \frac{1}{V_a} (V_{pa} |E_p|^2 E_a + V_{\text{FWM}} E_p E_p E_s^*), \end{aligned} \quad (2.90c)$$

where the cavity's single mode-volumes V_p , V_s and V_a and the Raman overlap mode-volumes V_{ps} and V_{pa} are given by

$$V_{p(s,a)} = 2\pi \int_{-L/2}^{L/2} dz \int_0^\infty r dr |u_{p(s,a)}|^2 = 2\pi \frac{L}{8} \frac{b}{k_{p(s,a)}}, \quad (2.91a)$$

$$V_{ps(pa)} = 2\pi \int_{-L/2}^{L/2} dz \int_0^\infty r dr |u_p|^2 |u_{s(a)}|^2 = \frac{2\pi}{16} \frac{b^2}{k_p + k_{s(a)}} \tan^{-1} \left(\frac{L}{b} \right). \quad (2.91b)$$

There is also a four-wave-mixing (FWM) mode-volume V_{FWM} that is given by the integral

$$V_{\text{FWM}} = 2\pi \int_{-L/2}^{L/2} dz \int_0^\infty r dr u_p^2 u_s^* u_a^*. \quad (2.92)$$

The integral is difficult to calculate unless we use the collimated-beam-approximation so that the phase of the intracavity wavefront has no z -dependence:

$$u_q(r, z) = e^{-r^2 k_q / b} \sin(k_q z). \quad (2.93)$$

With this approximation we can calculate that

$$V_{\text{FWM}} = 2\pi \frac{1}{8} \frac{b}{\sum k} \frac{\sin(\Delta k L / 2)}{\Delta k}, \quad (2.94)$$

where $\sum k = 2k_p + k_s + k_a$ and $\Delta k = 2k_p - k_s - k_a$. We substitute this result along with Eqs. (2.91) (applying the approximation Eq.(2.66)) to obtain

$$\begin{aligned} \dot{E}_p + \left\{ \frac{\gamma_{cp}}{2} - i \left[\left(\frac{N\hbar a_p}{\epsilon_0} + 1 \right) \omega_p - \omega_{cp} \right] \right\} E_p = \frac{\gamma_{ep}}{2} E_{ep} \\ + \omega_p \frac{N\hbar d_0^2 D}{2\epsilon_0} \frac{1}{\gamma_{ab} + i\delta} \frac{1}{2} \left[\frac{k_p}{k_p + k_s} |E_s|^2 E_p + \frac{k_p}{\sum k} \frac{\sin(\Delta k L / 2)}{\Delta k L / 2} E_p^* E_s E_a \right] \\ - \omega_p \frac{N\hbar d_0^2 D}{2\epsilon_0} \frac{1}{\gamma_{ab} - i\delta} \frac{1}{2} \left[\frac{k_p}{k_p + k_a} |E_a|^2 E_p + \frac{k_p}{\sum k} \frac{\sin(\Delta k L / 2)}{\Delta k L / 2} E_p^* E_s E_a \right], \end{aligned} \quad (2.95a)$$

$$\dot{E}_s + \left\{ \frac{\gamma_{cs}}{2} - i \left[\left(\frac{N\hbar a_s}{\epsilon_0} + 1 \right) \omega_s - \omega_{cs} \right] \right\} E_s = -\omega_s \frac{N\hbar d_0^2 D}{2\epsilon_0} \frac{1}{\gamma_{ab} - i\delta} \frac{1}{2} \left[\frac{k_s}{k_p + k_s} |E_p|^2 E_s + \frac{k_s}{\sum k} \frac{\sin(\Delta k L/2)}{\Delta k L/2} E_p E_p E_s^* \right], \quad (2.95b)$$

$$\dot{E}_a + \left\{ \frac{\gamma_{ca}}{2} - i \left[\left(\frac{N\hbar a_a}{\epsilon_0} + 1 \right) \omega_a - \omega_{ca} \right] \right\} E_a = \omega_a \frac{N\hbar d_0^2 D}{2\epsilon_0} \frac{1}{\gamma_{ab} + i\delta} \frac{1}{2} \left[\frac{k_a}{k_p + k_a} |E_p|^2 E_a + \frac{k_a}{\sum k} \frac{\sin(\Delta k L/2)}{\Delta k L/2} E_p E_p E_s^* \right]. \quad (2.95c)$$

Let us write these equations in simpler forms. First, as discussed in page 32, the reference frequencies $\omega_{p(s,a)}$ can be arbitrarily chosen. Thus we can choose them to make $(N\hbar a_q/\epsilon_0 + 1)\omega_q - \omega_{cq} = 0$ ($q = p, s, a$). Second, we define a coupling coefficient

$$C_c = \frac{k_p + k_s}{\sum k} \frac{\sin(\Delta k L/2)}{\Delta k L/2}, \quad (2.96)$$

and use the gain factor $G(\delta)$ defined by Eq. (2.65):

$$G(\delta) = -\frac{1}{4} \omega_s \frac{N\hbar d_0^2 D}{\epsilon_0} \frac{\gamma_{ab}}{\gamma_{ab}^2 + \delta^2} \frac{\lambda_p}{\lambda_p + \lambda_s} \frac{\tan^{-1}(L/b)}{L/b} \approx -\frac{1}{4} \omega_s \frac{N\hbar d_0^2 D}{\epsilon_0} \frac{\gamma_{ab}}{\gamma_{ab}^2 + \delta^2} \frac{\lambda_p}{\lambda_p + \lambda_s}. \quad (2.97)$$

Eqs. (2.95) then become

$$\dot{E}_p + \frac{\gamma_{cp}}{2} E_p = \frac{\gamma_{ep}}{2} E_{ep} - \frac{\omega_p k_p}{\omega_s k_s} G(\delta) \left(1 - \frac{i\delta}{\gamma_{ab}} \right) [|E_s|^2 E_p + C_c E_p^* E_s E_a] + \frac{\omega_p k_p}{\omega_s k_s} G(\delta) \left(1 + \frac{i\delta}{\gamma_{ab}} \right) \left[\frac{k_p + k_s}{k_p + k_a} |E_a|^2 E_p + C_c E_p^* E_s E_a \right], \quad (2.98a)$$

$$\dot{E}_s + \frac{\gamma_{cs}}{2} E_s = G(\delta) \left(1 + \frac{i\delta}{\gamma_{ab}} \right) [|E_p|^2 E_s + C_c E_p E_p E_a^*], \quad (2.98b)$$

$$\dot{E}_a + \frac{\gamma_{ca}}{2} E_a = -\frac{\omega_a k_a}{\omega_s k_s} G(\delta) \left(1 - \frac{i\delta}{\gamma_{ab}} \right) \left[\frac{k_p + k_s}{k_p + k_a} |E_p|^2 E_a + C_c E_p E_p E_s^* \right]. \quad (2.98c)$$

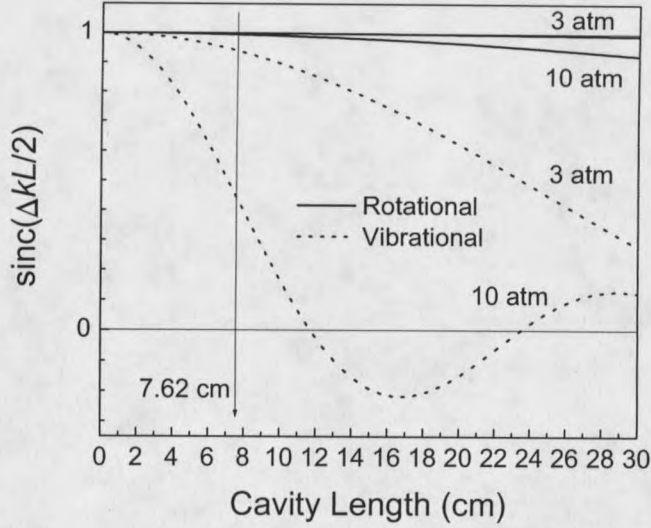


Figure 10 The values of $\text{sinc}(\Delta kL/2) = \frac{\sin(\Delta kL/2)}{\Delta kL/2}$ as a function of cavity length. We plotted for $\lambda_p = 792$ nm, $\lambda_s = 830$ nm in the rotational transition and $\lambda_s = 1180$ nm in the vibrational transition at two different H_2 pressures. When the H_2 pressure is 10 atm (3 atm), $\Delta k \approx -4.6 \text{ m}^{-1}$ (-1.4 m^{-1}) for the rotational transition and $\Delta k \approx -54 \text{ m}^{-1}$ (-16 m^{-1}) for the vibrational transition. 7.62 cm (3 in) is the cavity length we have used in the demonstrated cw Stokes laser systems.

Note that E_p , E_s and E_a are all complex fields. We separate them into their amplitudes and phases in the forms

$$E_p(t) = |E_p(t)|e^{-i\phi_p(t)}, \quad E_{ep}(t) = |E_{ep}(t)|e^{-i\phi_p(t)}; \quad (2.99a)$$

$$E_s(t) = |E_s(t)|e^{-i\phi_s(t)}. \quad (2.99b)$$

$$E_a(t) = |E_a(t)|e^{-i\phi_a(t)}. \quad (2.99c)$$

Substituting them into Eqs. (2.98), the real parts give equations for field amplitudes:

$$\begin{aligned}
|\dot{E}_p| + \frac{\gamma_{cp}}{2}|E_p| = \frac{\gamma_{ep}}{2}|E_{ep}| - \frac{\omega_p k_p}{\omega_s k_s} G(\delta) \left[|E_s|^2 |E_p| - \frac{k_p + k_s}{k_p + k_a} |E_a|^2 |E_p| \right] \\
- 2 \frac{\omega_p k_p}{\omega_s k_s} C_c G(\delta) |E_p| |E_s| |E_a| \frac{\delta}{\gamma_{ab}} \sin(\Delta\phi), \quad (2.100a)
\end{aligned}$$

$$\begin{aligned}
|\dot{E}_s| + \frac{\gamma_{cs}}{2}|E_s| = G(\delta) |E_p|^2 |E_s| \\
+ C_c G(\delta) |E_p| |E_p| |E_a| \left[\cos(\Delta\phi) + \frac{\delta}{\gamma_{ab}} \sin(\Delta\phi) \right], \quad (2.100b)
\end{aligned}$$

$$\begin{aligned}
|\dot{E}_a| + \frac{\gamma_{ca}}{2}|E_a| = - \frac{\omega_a k_a}{\omega_s k_s} G(\delta) \frac{k_p + k_s}{k_p + k_a} |E_p|^2 |E_a| \\
- \frac{\omega_a k_a}{\omega_s k_s} C_c G(\delta) |E_p| |E_p| |E_s| \left[\cos(\Delta\phi) - \frac{\delta}{\gamma_{ab}} \sin(\Delta\phi) \right]. \quad (2.100c)
\end{aligned}$$

The imaginary parts give equations for the frequency pulling:

$$\begin{aligned}
\dot{\phi}_p = - \frac{\omega_p k_p}{\omega_s k_s} G(\delta) \left[|E_s|^2 + \frac{k_p + k_s}{k_p + k_a} |E_a|^2 \right] \frac{\delta}{\gamma_{ab}} \\
- 2 \frac{\omega_p k_p}{\omega_s k_s} C_c G(\delta) |E_s| |E_a| \frac{\delta}{\gamma_{ab}} \cos(\Delta\phi), \quad (2.101a)
\end{aligned}$$

$$\dot{\phi}_s = - G(\delta) |E_p|^2 \frac{\delta}{\gamma_{ab}} - C_c G(\delta) |E_p| |E_p| \frac{|E_a|}{|E_s|} \left[\frac{\delta}{\gamma_{ab}} \cos(\Delta\phi) - \sin(\Delta\phi) \right], \quad (2.101b)$$

$$\begin{aligned}
\dot{\phi}_a = - \frac{\omega_a k_a}{\omega_s k_s} G(\delta) \frac{k_p + k_s}{k_p + k_a} |E_p|^2 \frac{\delta}{\gamma_{ab}} \\
- \frac{\omega_a k_a}{\omega_s k_s} C_c G(\delta) |E_p| |E_p| \frac{|E_s|}{|E_a|} \left[\frac{\delta}{\gamma_{ab}} \cos(\Delta\phi) + \sin(\Delta\phi) \right], \quad (2.101c)
\end{aligned}$$

where $\Delta\phi = 2\phi_p - \phi_s - \phi_a$ is the phase difference between the three waves.

Analytic steady-state solution for zero two-photon-detuning

When the two-photon-detuning $\delta = 0$, the Raman-induced dispersion equals zero and thus the frequency pulling $\dot{\phi}_p = \dot{\phi}_s = \dot{\phi}_a = 0$ (later our numerical solution will confirm this). Under this condition, from Eqs. (2.101) it is easy to see

$$\sin(\Delta\phi) = \sin(2\phi_p - \phi_s - \phi_a) = 0. \quad (2.102)$$

This still leaves an uncertainty of whether $\cos(\Delta\phi) = 1$ or -1 . Let us examine Eq. (2.100c) at steady state. Since the field amplitude $|E_a|$ is non-negative, $\cos(\Delta\phi) = -1$ ($+1$) is then required when $C_c > 0$ (< 0), or

$$\Delta\phi = 2\phi_p - \phi_s - \phi_a = \begin{cases} (\text{odd integer}) \times \pi, & \text{if } C_c > 0; \\ (\text{even integer}) \times \pi, & \text{if } C_c < 0. \end{cases} \quad (2.103)$$

Therefore under the condition of zero two-photon-detuning, the field amplitude equations at steady state have the form

$$\frac{\gamma_{cp}}{2}|E_p| = -\frac{\omega_p k_p}{\omega_s k_s} G(\delta) \left(|E_s|^2 |E_p| - \frac{k_p + k_s}{k_p + k_a} |E_a|^2 |E_p| \right) + \frac{\gamma_{ep}}{2} |E_{ep}(t)|, \quad (2.104a)$$

$$\frac{\gamma_{cs}}{2}|E_s| = G(\delta) (|E_p|^2 |E_s| - |C_c| |E_p| |E_p| |E_a|), \quad (2.104b)$$

$$\frac{\gamma_{ca}}{2}|E_a| = -\frac{\omega_a k_a}{\omega_s k_s} G(\delta) \left(\frac{k_p + k_s}{k_p + k_a} |E_p|^2 |E_a| - |C_c| |E_p| |E_p| |E_s| \right). \quad (2.104c)$$

From Eqs. (2.104b) and (2.104c), we can eliminate $|E_p|^2$ to obtain

$$|C_c| \left(\frac{|E_a|}{|E_s|} \right)^2 - \left(\frac{\gamma_{cs} \omega_a k_a k_p + k_s}{\gamma_{ca} \omega_s k_s k_p + k_a} + 1 \right) \frac{|E_a|}{|E_s|} + \frac{\gamma_{cs} \omega_a k_a}{\gamma_{ca} \omega_s k_s} |C_c| = 0. \quad (2.105)$$

Let ξ denote the ratio $|E_a|/|E_s|$. Eq. (2.105) has two roots:

$$\xi_{\pm} = \frac{1}{2|C_c|} \left(\frac{\gamma_{cs} \omega_a k_a k_p + k_s}{\gamma_{ca} \omega_s k_s k_p + k_a} + 1 \right) \pm \frac{1}{2|C_c|} \sqrt{\left(\frac{\gamma_{cs} \omega_a k_a k_p + k_s}{\gamma_{ca} \omega_s k_s k_p + k_a} + 1 \right)^2 - 4 \frac{\gamma_{cs} \omega_a k_a}{\gamma_{ca} \omega_s k_s} C_c^2}. \quad (2.106)$$

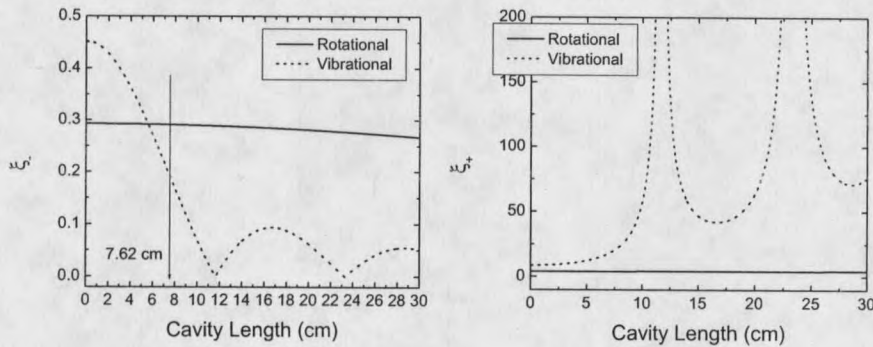


Figure 11 Values of ξ 's are calculated as function of cavity length (left: ξ_- , right: ξ_+). ξ_+ is always larger than 1. 7.62 cm (3 in) is the cavity length we have used in the demonstrated systems. Parameters used for calculation are: $\lambda_p = 792$ nm, $\lambda_s = 830$ nm, $\lambda_a = 757$ nm (rotational), $\lambda_s = 1180$ nm, $\lambda_a = 596$ nm (vibrational), reflectance and absorption are 0.9999 and 30 ppm for both mirrors and all wavelengths, mirror radius of curvature is 50 cm, H_2 pressure is 10 atm, and $\Delta k \approx -4.6$ m $^{-1}$ for the rotational transition, $\Delta k \approx -54$ m $^{-1}$ for the vibrational transition.

We discard the root ξ_+ since it corresponds to $|E_a/E_s| > 1$ which is physically impossible. We find that ξ_- is a constant that is not dependent on the pumping rate (i.e., the amplitude ratio of the anti-Stokes and Stokes fields is only dependent on their wavelengths and cavity's properties). Eq.(2.104b) can be written in term of ξ_- in the form

$$|E_p| = \sqrt{\frac{\gamma_{cs}}{2G(\delta)(1 - \xi_-|C_c|)}}. \quad (2.107)$$

Comparing with Eq.(2.70), we find that when the Stokes–anti-Stokes coupling is present, the pump light is clamped at a higher value or equivalently, the steady-state Stokes gain $G(\delta)$ is decreased by $(1 - \xi_- |C_c|)$ (note that $0 \leq \xi_- \leq 1$ and $0 \leq |C_c| \leq 1$).

From Eq.(2.104a) we can solve for $|E_s|$ and $|E_a|$:

$$|E_s| = \sqrt{\frac{\omega_s k_s}{\omega_p k_p} \frac{\gamma_{ep} |E_{ep}| / |E_p| - \gamma_{cp}}{2G(\delta) [1 - \xi_-^2 (k_p + k_s) / (k_p + k_a)]}}, \quad (2.108)$$

$$|E_a| = \xi_- |E_s|. \quad (2.109)$$

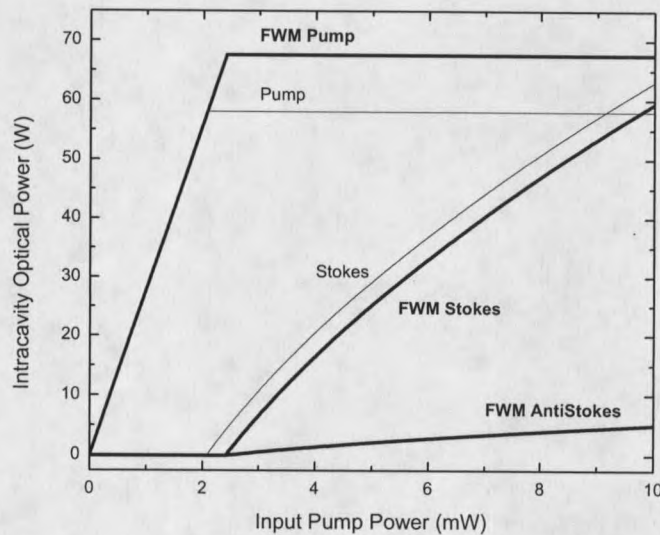


Figure 12 Theoretical plots for the rotational Raman laser (steady-state and zero two-photon-detuning). Thin curves are for the usual Stokes laser while thick curves are when there is four-wave mixing coupling between the Stokes and anti-Stokes. About 8.5% power conversion from Stokes to anti-Stokes, or 3.5% peak power conversion from the input pump to the anti-Stokes can be achieved. Same parameters are used for calculation as in Fig. 11.

Numerical solution

For the general case when the two-photon-detuning $\delta \neq 0$, we numerically solve Eqs. (2.98) using MATHEMATICA [35].

We numerically solve Eqs. (2.98) for the rotational transition pumped by a 792 nm laser (Stokes: 830 nm, anti-Stokes: 757 nm). We choose the rotational instead of a vibrational transition because (1) the rotational transition is easier to be phase-matched (see Fig. 10); and (2) high-finesse mirror coating at wavelengths of the pump, the rotational Stokes and anti-Stokes is easier (see Chapter 4). Therefore generating a cw rotational anti-Stokes beam is easier and our numerical calculation is more practical. The rotational Raman gain and the linewidth used for the numerical calculation are $\alpha_g = 0.5 \times 10^{-9} \text{ cm/W}$ (line-center value for 10 atm H_2 at 25°C)[4, 5, 6] and $\gamma_{abv}/2\pi = 500 \text{ MHz}$ (HWHM; for 10 atm H_2 at 25°C)[7]. The following cavity parameters are used: $R = 0.9999$ (mirror reflectance) and $A = 30 \times 10^{-6}$ (mirrors' power loss) for both mirrors at all three wavelengths; $L = 7.62 \text{ cm}$ (cavity length); $r = 50 \text{ cm}$ (mirrors' radius of curvature) for both mirrors. In addition, we choose the reference frequency $\omega_{p(s,a)} = \omega_{cp(s,a)}/n_{p(s,a)}$ to simplify the calculation.

The first time-dependent result is given in Fig. 13. Assuming the input pump power is four times the line-center threshold ($= 2.4 \text{ mW}$), the field amplitudes of the pump, the Stokes, and the anti-Stokes waves are calculated as functions of time. We convert them into optical powers using Eq. (2.81) and then plot in Fig. 13. Three cases of different Raman detunings (all at 4 times the line-center threshold) are calculated and plotted. It can be seen that, as the laser is detuned away from the Raman

resonance by 800 MHz, it turns on smoothly and slowly due to the weaker pumping rate (the threshold increases as detuned away); whereas when the laser is on or near the Raman resonance (now it is pumped harder), there are dramatic dynamics before the steady state for all three waves.

We are interested in steady-state tuning characteristics — optical powers of the three fields as functions of the two-photon-detuning. Although it is difficult to do the analytic steady-state solutions in the case of $\delta \neq 0$, we can obtain them from the time-dependent numerical results (i.e., picking the values after the steady-state is reached). Using this method, the steady-state tuning results are plotted in Fig. 14.

Since we directly solve the complex field equations, besides field amplitudes we also obtain the solutions to the phases. Fig. 15 shows that, at steady state, the phases of the three fields change linearly with time. The slopes of the linear changes give the amounts of frequency-pulling. Fig. 16 plots the steady-state frequency-pullings of the three fields as functions of the two-photon-detuning after we calculate the slopes in Fig. 15.

Although Fig. 15 shows that the individual phases of the three fields change linearly with time at steady-state, we find that the phase difference, $\Delta\phi = 2\phi_p - \phi_s - \phi_a$, will settle down to a constant after the steady state is reached (like the field amplitudes), see Fig. 17. We see that only when the two-photon-detuning is zero, $\Delta\phi = \pi$; when we detune away from the Raman line-center, $\Delta\phi$ is close to, but not exactly equal to π . Going back to Eqs. (2.100) and (2.101), this means that only

when the two-photon-detuning $\delta = 0$, the equations of the amplitudes and the phases are de-coupled and the analytic solution is possible.

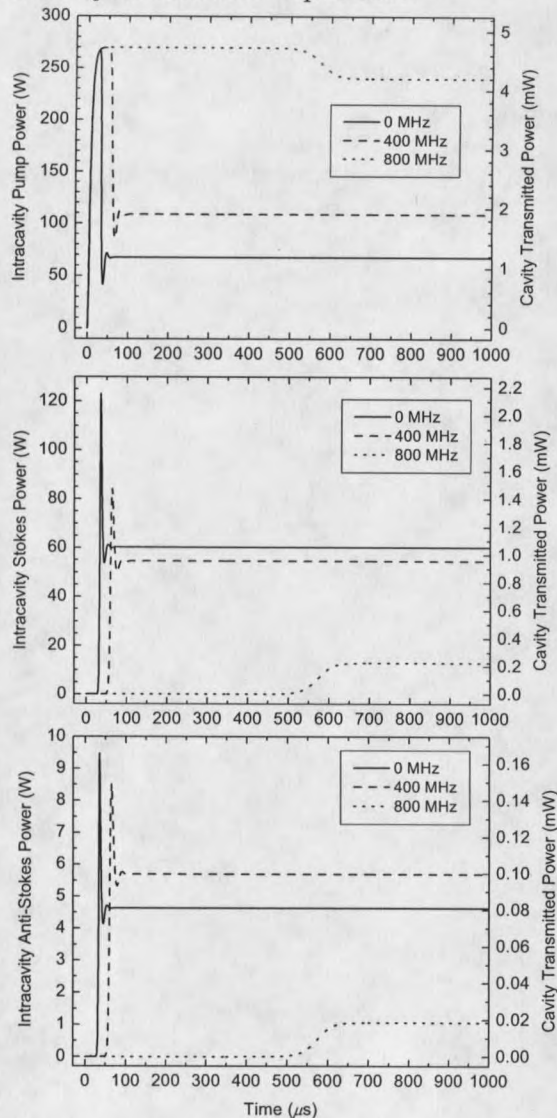


Figure 13 Numerical simulation of the “turn-on” behavior in a cw rotational Raman laser with anti-Stokes emission at different Raman detunings. The pump (top), Stokes (middle), and anti-Stokes (bottom) powers are plotted as functions of time. They are all pumped at 4 times the line-center threshold ($= 2.4 \text{ mW}$). The solid line, the dashed line, and the dotted line are when the two-photon-detuning $\delta/2\pi = 0 \text{ MHz}$, $= 400 \text{ MHz}$, and $= 800 \text{ MHz}$ respectively. The left horizontal axis is the intracavity spatial peak power and the right axis is the cavity transmitted power (single end).

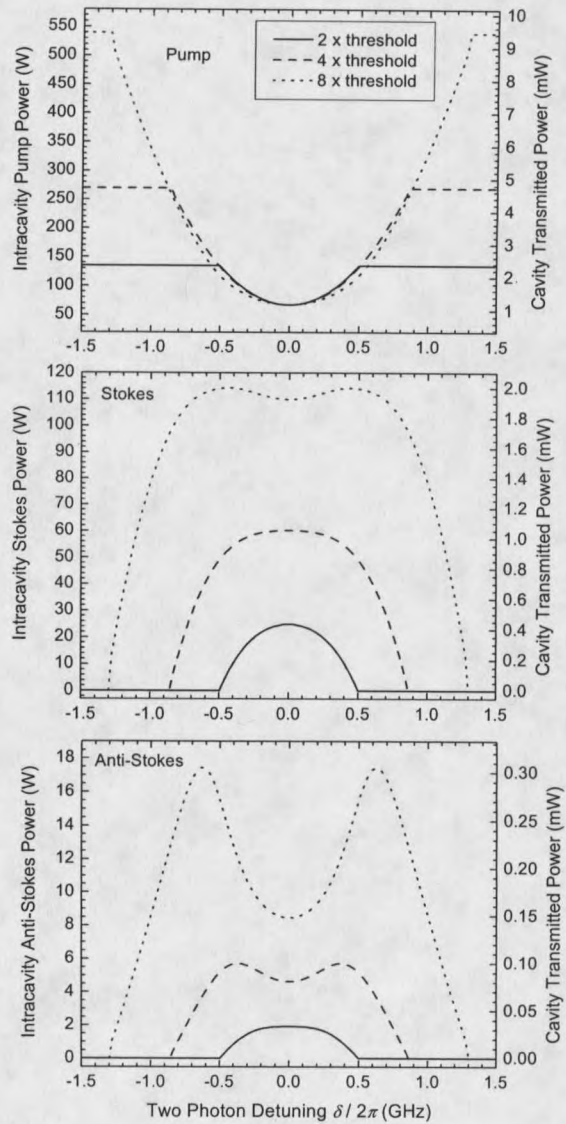


Figure 14 The steady-state powers of pump (top), Stokes (middle), and anti-Stokes (bottom) are numerically calculated as functions of the two-photon-detuning. The solid line, the dashed line, and the dotted line are when the pumping-rate is equal to $2\times$, $4\times$, and $8\times$ the line-center threshold ($= 2.4$ mW) respectively. The left horizontal axis is the intracavity spatial peak power and the right axis is the cavity transmitted power (single end).

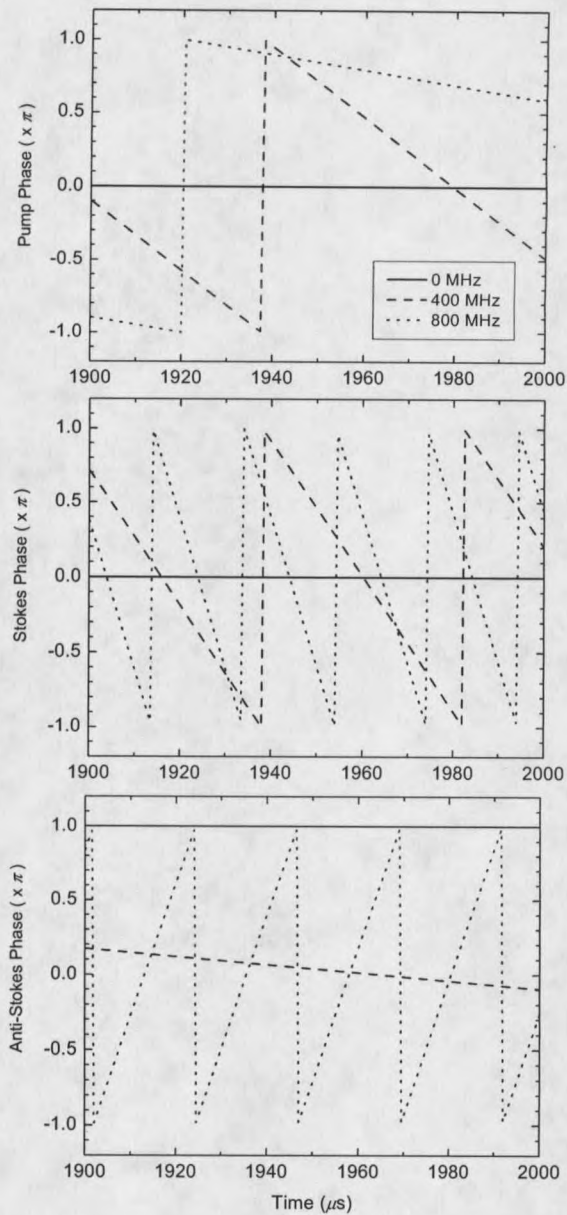


Figure 15 The numerically calculated steady-state phase evolutions in a cw rotational Raman laser with anti-Stokes emission at different Raman detunings. The pump (top), the Stokes (middle), and the anti-Stokes (bottom) phases are plotted as functions of time. They are all pumped at 4 times the line-center threshold ($= 2.4 \text{ mW}$). The solid line, the dashed line, and the dotted line are when the two-photon-detuning $\delta/2\pi = 0 \text{ MHz}$, $= 400 \text{ MHz}$, and $= 800 \text{ MHz}$ respectively.

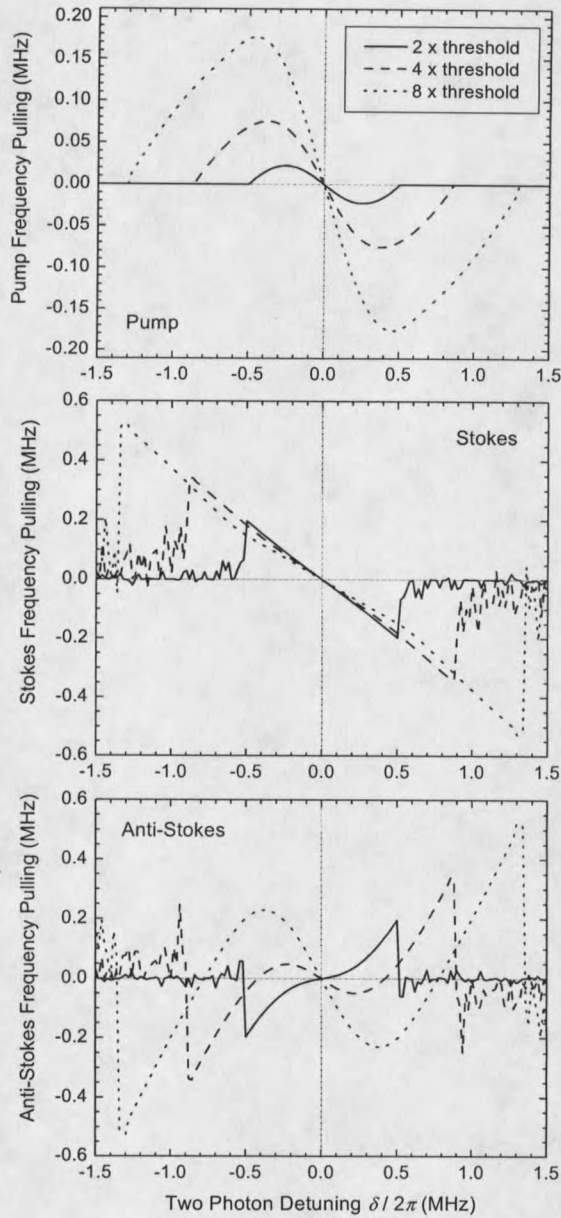


Figure 16 The numerically calculated steady-state frequency-pullings of pump (top), Stokes (middle), and anti-Stokes (bottom) as functions of two-photon-detuning. The solid line, the dashed line, and the dotted line are when the pumping-rate is equal to $2\times$, $4\times$, and $8\times$ the line-center threshold ($= 2.4$ mW) respectively. The random noise-like curves are when the laser is below threshold.

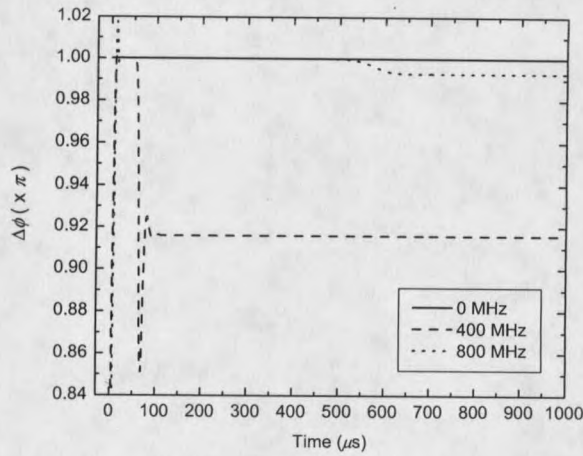


Figure 17 The numerically calculated phase difference, $\Delta\phi = 2\phi_p - \phi_s - \phi_a$, as a function of time. The solid line, the dashed line, and the dotted line are when the two-photon-detuning $\delta/2\pi = 0$ MHz, $= 400$ MHz, and $= 800$ MHz respectively. They are all pumped at 4 times the line-center threshold ($= 2.4$ mW).

Furthermore, we collect the steady-state values of $\Delta\phi$ from the results shown in

Fig. 17 and then plot these values in Fig. 18.

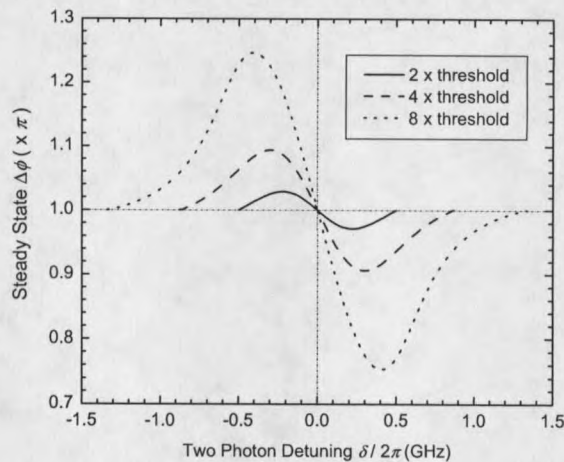


Figure 18 The numerically calculated steady-state values of the phase difference, $\Delta\phi = 2\phi_p - \phi_s - \phi_a$, as a function of two-photon-detuning. The solid line, the dashed line, and the dotted line are when the pumping-rate is equal to $2\times$, $4\times$, and $8\times$ the line-center threshold ($= 2.4$ mW) respectively.

Bad news: the dispersion

So far, using the triple-resonance cavity enhancement to generate cw anti-Stokes light seems to be a promising new method of frequency up-conversion: the threshold is below 10 mW and the power conversion efficiency can reach 3.5% for the rotational transition (see Fig. 12). This only requires the cavity mirrors to have a reflectance of 0.9999 and absorption of 30 parts per million — practically realizable in the mirror coating with a wavelength bandwidth of 80 nm (to cover the range from the rotational Stokes to anti-Stokes in H_2). However, the above prediction is based on the theoretical work assuming that all three fields are resonant with the cavity. The question is: can this condition be realized in reality?

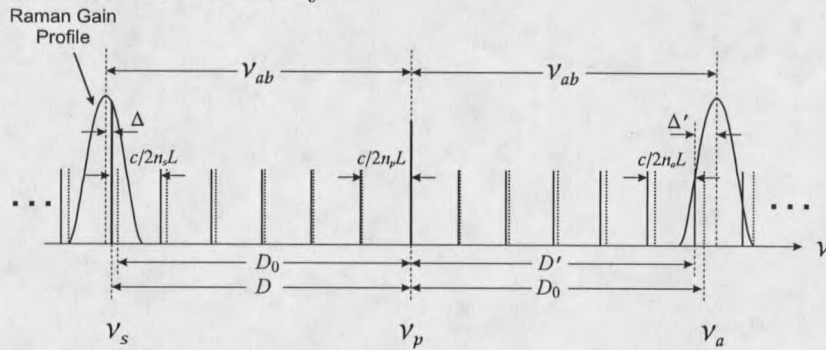


Figure 19 Illustration of (single-photon) dispersion effect in a high-finesse Raman cavity. Solid vertical lines represent actual cavity longitudinal modes (the taller and thicker solid lines means the oscillating modes); dotted vertical lines are “conceptual” and are drawn equally spaced — they are the longitudinal modes assuming that the intracavity refractive index is a constant n_p . Using these modes as a reference, the actual cavity mode-spacings will be larger at lower frequencies and smaller at higher frequencies. ν_{ab} is the Raman shift; Δ is the Raman detuning of the lasing Stokes mode; Δ' is the detuning of the anti-Stokes resonance. The anti-Stokes mode cannot oscillate unless $\Delta' = -\Delta$.

Using Fig. 19, let us analyze if all three fields can be simultaneously resonant

with the cavity. Because of the frequency-dependent refractive index in H_2 (i.e., dispersion), the cavity longitudinal mode-spacing (or free-spectral-range) $c/2nL$ is also frequency dependent. Specifically, we have $c/2n_sL > c/2n_pL > c/2n_aL$ since $n_s < n_p < n_a$. If, starting from the pump frequency ν_p we move along the frequency axis to the left, then the actual cavity modes (solid lines) will be seen ahead of the reference pump modes (dashed lines). When we reach the Stokes frequency range ν_s , the pump modes have accumulated a distance of D_0 :

$$D_0 = N_c \times \frac{c}{2n_pL}, \quad (2.110)$$

where N_c is the total number of cavity longitudinal modes in the Raman shifting range of ν_{ab} ; for our 3 inch cavity and the rotational transition $\nu_{ab} = 586.9 \text{ cm}^{-1}$, $N_c = 8956$ (Fig. 19 only shows 7 modes for illustration). Meantime, the actual cavity modes have accumulated a distance of D :

$$\begin{aligned} D &= \frac{c}{2(n_p - \Delta n)L} - \frac{c}{2(n_p - 2\Delta n)L} - \dots - \frac{c}{2(n_p - N\Delta n)L} \\ &= \frac{c}{2L} \sum_{m=1}^{N_c} \frac{1}{n_p - m\Delta n}, \end{aligned} \quad (2.111)$$

where Δn is the refractive index change per free-spectral-range (we assume the dispersion between ν_s and ν_p is linear, see Fig. 20).

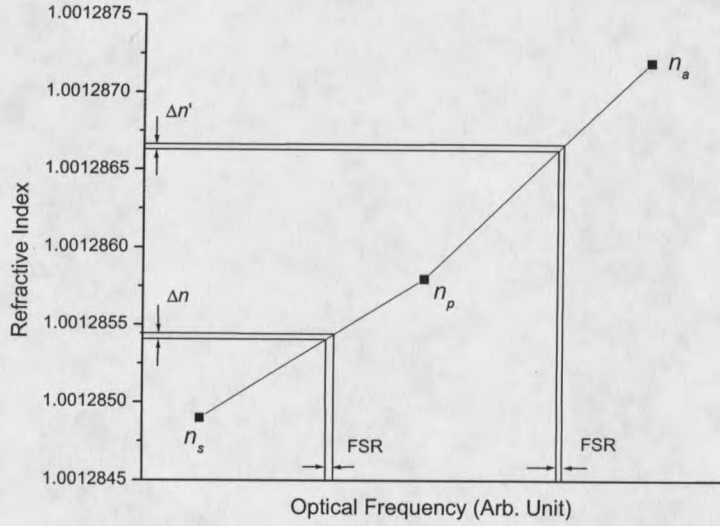


Figure 20 Dispersion in Raman cavity. Refractive index values are for rotational Raman transition (pump = 792 nm, Stokes = 830 nm, and anti-Stokes = 757 nm) in 10 atm H₂ at room temperature. Δn and $\Delta n'$ are the average index changes per free-spectral-range.

Similarly, at the anti-Stokes side,

$$D' = \frac{c}{2L} \sum_{m=1}^{N_c} \frac{1}{n_p + m\Delta n'} \quad (2.112)$$

Therefore, instead of having a two-photon-detuning Δ , the anti-Stokes resonance now has a detuning Δ' from the Raman gain line-center and from the above formulas we have

$$\begin{aligned} |\Delta'| - |\Delta| &= (D - D_0) + (D_0 - D') \\ &= \frac{c}{2L} \sum_{m=1}^{N_c} \left(\frac{1}{n_p - m\Delta n} - \frac{1}{n_p + m\Delta n'} \right). \end{aligned} \quad (2.113)$$

This is the amount of frequency offset brought by the dispersion; the anti-Stokes cavity resonance cannot oscillate unless this offset equals zero (i.e., $\Delta' = -\Delta$). Table 1 gives several values of this offset in various conditions calculated by Eq. (2.113).

Type of transition	H ₂ pressure	Refractive indexes	Dispersion Offset
Rotational $\lambda_p = 792$ nm $\lambda_s = 830$ nm $\lambda_a = 757$ nm	10 atm	$n_s = 1.0012849$ $n_p = 1.0012858$ $n_a = 1.0012872$	20.2 MHz
	1 atm	$n_s = 1.0001285$ $n_p = 1.0001286$ $n_a = 1.0001287$	2.03 MHz
Vibrational $\lambda_p = 792$ nm $\lambda_s = 1180$ nm $\lambda_a = 596$ nm	10 atm	$n_s = 1.0012765$ $n_p = 1.0012858$ $n_a = 1.0012956$	168 MHz
	1 atm	$n_s = 1.0001276$ $n_p = 1.0001286$ $n_a = 1.0001296$	16.8 MHz

Table 1 Calculated frequency-offset values of the anti-Stokes cavity resonance caused by the dispersion (all for room temperature). Refractive indexes of H₂ are estimated by curve-fitting the published values given in reference [1], page 6-95.

From Table 1, we see that the (single-photon) dispersion results in frequency-offsets on the anti-Stokes cavity modes that are larger than the usual linewidth of the high-finesse cavity (~ 10 kHz–1 MHz). One might think that the frequency-pullings induced by the two-photon dispersion (see Fig. 16) can compensate these frequency-offsets by appropriately detuning away from the Raman line-center. Unfortunately, the two-photon frequency-pullings are still too small (< 1 MHz). Therefore the anti-Stokes modes are not able to oscillate in the cavity; in other words, the triple-resonance condition we relied on to derive the theory cannot be reached.

However, we have noted that it is possible to fabricate broadband, high-reflectivity, and dispersion-compensating mirrors [36]. These so-called “chirped” mirrors allow for longer wavelengths penetrating deeper into the mirror. Therefore this is a way for us

to compensate for the dispersion so that the pump, Stokes and anti-Stokes fields can have the same effective cavity length, or the same mode-spacing. If this is true, then in Fig. 19, the Stokes and anti-Stokes modes will be symmetrically positioned away from the pump mode in frequency, and the triple-resonant condition can be achieved.

This entire analysis on the dispersion effect was considered by Roos [24] and is presented here under his permission.

CHAPTER 3

DIODE-PUMPED CW VIBRATIONAL RAMAN LASER

We present in this chapter the experimental achievements of the diode-pumped cw vibrational Raman laser.

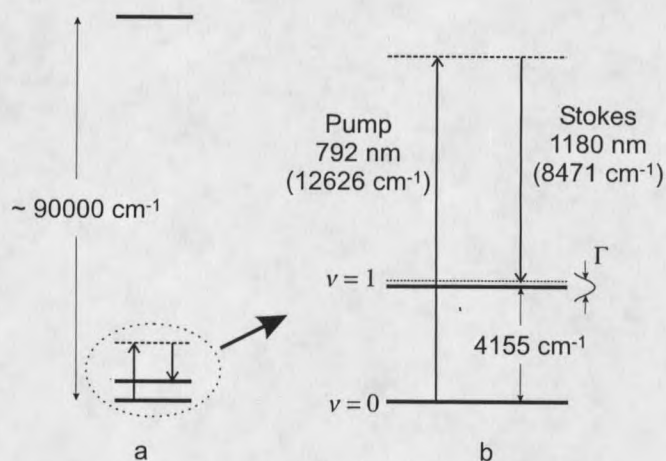
System Overview and CharacteristicsVibrational Raman transition in H₂

Figure 21 Energy level diagram for the cw vibrational Raman laser in H₂. Spectral distances between levels and laser frequencies are drawn to scale. a, Three levels from bottom to top are (thick solid lines): the ground state, the first vibrational state, and the first excited electronic state. Distance between the ground state and the first electronic state is about 90,000 cm⁻¹. b, Zoomed-in diagram showing the two-photon Raman process. The incident pump photon transfers population from the ground state (the vibrational quantum number $v = 0$) to the vibrational state $v = 1$ producing a Stokes photon with a frequency shift of 4155 cm⁻¹.

We use diatomic hydrogen gas (H₂) at room temperature as the Raman gain

medium. The vibrational Raman transition in H_2 has a frequency shift of 4155 cm^{-1} from $v = 0$ to $v = 1$ level (labeled as $Q_{01}(1)^1$), as shown in Fig. 21. There are other vibrational transitions, as well. But they have less gain than the $Q_{01}(1)$ and these Stokes wavelengths are not covered by the cavity's high-finesse bandwidth so will not lase in our cw Raman system.

The vibrational Raman gain linewidth was studied by Bischel and Dyer [3]. They gave a best-fit formula for the FWHM Raman linewidth in MHz^2 for temperature between 77-500 K, densities of 1-50 amagats³:

$$\Gamma(\rho, T) = \frac{309}{\rho} \left[\frac{T}{298} \right]^{0.92} + [51.8 + 0.152(T - 298) + 4.85 \times 10^{-4}(T - 298)^2]\rho, \quad (3.1)$$

where ρ is the H_2 density in amagats, T is the temperature in Kelvin. We plot linewidth vs. pressure at the temperature of 298 K in Fig. 22.

¹ In $Q_{01}(1)$, Q denotes a pure vibrational Raman transition; the subscript 01 means from $v = 0$ to $v = 1$ level; and the number 1 in the parenthesis tells the initial rotational J level (since this is a pure vibrational transition, the initial and final J are equal)

² In this and the next chapters, the units of all the quantities associated with frequency or rate are Hz instead of rad/sec we used in the last chapter. Consequently the notations are changed from the last chapter (in parentheses): ν (ω) for optical frequency; Γ ($2\gamma_{ab}$) for FWHM Raman linewidth; Δ (δ) for two-photon-detuning, etc.

³ Amagat is a density unit for gas. It is defined as the molar density at 0°C and 1 atm pressure. For H_2 , 1 amagat = $4.4587 \times 10^{-5} \text{ mole/cm}^3 = \rho_A$. For an actual gas,

$$P/\rho = A + B\rho_A + C\rho_A^2 + \dots,$$

where P is pressure in atm, ρ is the molar density in amagat, and A , B , and C are constants. For H_2 at 25°C , $A = 1.09086$, $B = 0.6606 \times 10^{-3}$ and $C = 2.521 \times 10^{-6}$. Thus for converting between pressure in atm and density in amagat for H_2 at 25°C , approximately 1 amagat \leftrightarrow 1.091 atm, or 1 atm \leftrightarrow 0.917 amagat (at 0°C , approximately 1 amagat \leftrightarrow 0.999 atm). Reference: [1, page 4-158,165].

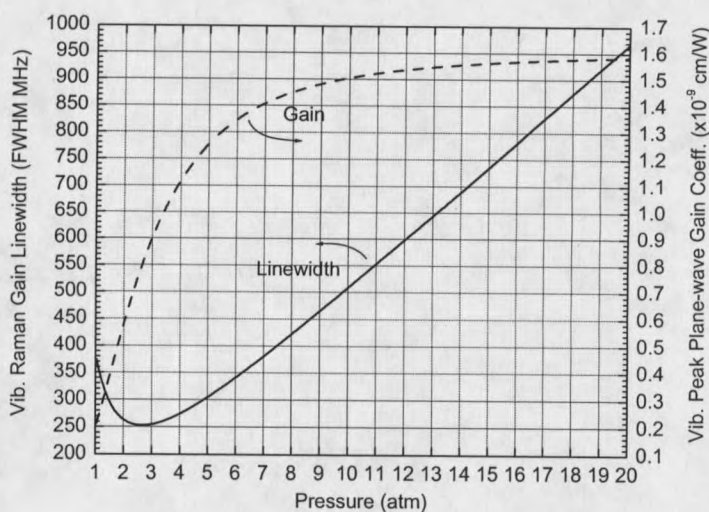


Figure 22 Vibrational Raman gain linewidth and peak plane-wave gain coefficient in H_2 as functions of pressure at $25^\circ C$. A pump wavelength of 792 nm is used in calculating the gain coefficient.

From Fig. 22, we see that at 298 K, above a high-pressure limit of 5~6 atm, the gain linewidth roughly linearly increases with the pressure. This is mainly caused by homogeneous pressure-broadening (the Raman coherence is damped by collisional dephasing) and the line-shape is close to a pure Lorentzian. When the pressure is neither high nor low (1 to 5 atm in Fig. 22), the linewidth is at a minimum. This is caused by the effect known as Dicke narrowing [37] or motional narrowing [38]. In this pressure region, the mean-free-path is comparable or a little less than a wavelength; the Doppler effect is restrained but the collisional dephasing is also not strong. Hence the linewidth is narrow in this region. Below a low-pressure limit of ~ 1 atm (not shown in Fig. 22), the gain linewidth will not be dependent on pressure. That is

the Doppler-broadened (inhomogeneous) region and the line-shape is close to a pure Gaussian.

The plane-wave Raman gain coefficient was measured by Bischel and Dyer [2] and an empirical formula to calculate the peak Raman gain as a function of wavelength and density at room-temperature (298 K) was given by

$$\alpha_g = 9.37 \times 10^6 \times \frac{52\rho}{\Gamma} \frac{K_B}{0.658} (\nu_p - 4155) \times (7.19 \times 10^9 - \nu_p^2)^{-2}, \quad (3.2)$$

where ρ is the density in amagats, Γ is the Raman linewidth given by Eq. (3.1), K_B is the Boltzmann population factor equal to 0.658 at 298 K for the $J = 1$ level in H_2 , and ν_p is the pump laser frequency in cm^{-1} . We plot this gain coefficient as a function of H_2 pressure in Fig. 22 (pump wavelength: 792 nm). Above a high-pressure limit of 7~8 atm, the peak Raman gain is nearly independent of pressure.

Threshold and steady-state power dependence

The power dependence equations given in this section were originally developed by Roos in Ref. [39].

The Stokes lasing threshold has been calculated in Chapter 2. When the input pump power P_{ep} is equal to or larger than

$$\begin{aligned} P_{th} &= \frac{\pi bc}{8\omega_p \mu_0 L G(\delta)} \frac{1}{4T_{1p}} \frac{(\ln \sqrt{R_{1p} R_{2p}})^2}{(-\ln \sqrt{R_{1s} R_{2s}})} \\ &= P_0 \frac{(\ln \sqrt{R_{1p} R_{2p}})^2}{4T_{1p}} \left(-\ln \sqrt{R_{1s} R_{2s}} \right) \end{aligned} \quad (3.3)$$

there will be Stokes generation (for notations please see Chapter 2). Here P_0 is defined

by

$$P_0 = \frac{\lambda_p + \lambda_s}{2\alpha_g \arctan(L/b)}, \quad (3.4)$$

which has a unit of power. Since the cavity finesse is related to the mirror reflectance R (assuming identical front and back mirrors) by

$$\mathcal{F} = \frac{\pi\sqrt{R}}{1-R}, \quad (3.5)$$

the threshold can be written in the form

$$P_{th} \approx \frac{\pi^2}{4} \frac{P_0}{\mathcal{F}_p \mathcal{F}_s} \quad (3.6)$$

when the approximation $R \approx 1$ is used. From this equation, P_0 is approximately the threshold pump power if without the cavity enhancement⁴.

From Chapter 2, the spatial peak intracavity powers (at the antinodes of the standing-wave), or four times the cavity circulating powers, are given by

(Intracavity pump:)

$$\Pi_p = \begin{cases} \frac{4T_{1p}}{(1-\sqrt{R_{1p}R_{2p}})^2} P_{ep}, & \text{if } P_{ep} < P_{th}; \\ (-\ln \sqrt{R_{1s}R_{2s}}) P_0, & \text{if } P_{ep} \geq P_{th}. \end{cases} \quad (3.7)$$

(Intracavity Stokes:)

$$\Pi_s = \begin{cases} 0, & \text{if } P_{ep} < P_{th}; \\ \frac{\lambda_p}{\lambda_s} \left[2\sqrt{\frac{T_{1p}}{(-\ln \sqrt{R_{1s}R_{2s}})} P_0 P_{ep}} - (-\ln \sqrt{R_{1p}R_{2p}}) P_0 \right], & \text{if } P_{ep} \geq P_{th}. \end{cases} \quad (3.8)$$

4

This statement can be justified by reference [33]. It can be seen that for a focused Gaussian pump beam, $P_0/2$ represents the pump power that gives an unity exponential-gain-coefficient.

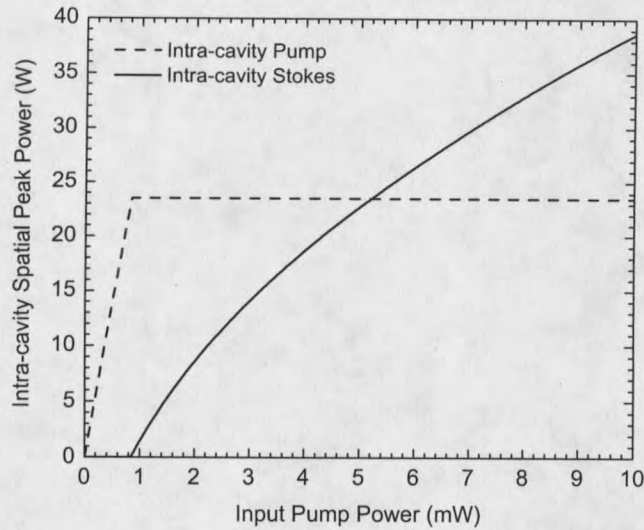


Figure 23 Theoretically calculated intra-cavity pump and Stokes spatial peak powers as functions of input pump power. This is calculated for the vibrational Stokes emission (1180 nm) pumped by 792 nm laser and the Stokes cavity resonance is in the gain line-center. Cavity finesse is assumed to be 31,400 ($R = 0.9999$) at both wavelengths.

In Fig. 23 we plot these two intracavity powers as functions of the input pump power using the following practical parameters: $R_{1p} = R_{2p} = R_{1s} = R_{2s} = 0.9999$ (cavity finesse: 31,400 at both wavelengths), $A_{1p} = A_{2p} = A_{1s} = A_{2s} = 30 \times 10^{-6}$ (mirrors' power loss), $L = 7.62$ cm, $b = 26.5$ cm (or mirrors' radius of curvature = 50 cm), $\lambda_p = 792$ nm, $\lambda_s = 1180$ nm, $\alpha_g = 1.5 \times 10^{-9}$ cm/W (line-center value for 10 atm H_2 at 25°C). We see from Fig. 23 the basic behavior of the cw Raman laser: after the threshold is reached the Stokes power starts to grow while the pump power clamps. The threshold in Fig. 23 is about 840 μ W; while if without the cavity enhancement the threshold $P_0 \approx 230$ kW. This shows the significance of the cavity enhancement's

ability to lower the Raman threshold.

From Fig. 23 we see that tens of watts is the typical intra-cavity spatial peak power (also circulating power) of the cw Raman laser. Due to the mirrors' absorption, there is heating of the mirrors' coating surfaces. A concern is then whether the intra-cavity laser power can damage the cavity mirrors. Barnes *et al.* has achieved $\sim 3 \text{ MW/cm}^2$ intra-cavity intensity without permanent mirror damage [40]. We use mirrors from the same manufacturer (Research Electro-optics) and we estimate that $0.5 \sim 1 \text{ MW/cm}^2$ is our safety limit given our higher reflectivity (>0.9999 vs. Barnes' 0.9995) and our double-wavelength coating. For the cavity parameters used in the calculations for Fig. 23, the beam areas on the mirror surfaces are approximately $1.1 \times 10^{-3} \text{ cm}^2$ (pump) and $1.7 \times 10^{-3} \text{ cm}^2$ (Stokes). If we take the circulating power to be 100 W, then the light intensities on the mirror surfaces are 91 kW/cm^2 (pump) and 59 kW/cm^2 (Stokes). Therefore we are well within the mirror-damage safety limit.

Knowing the intra-cavity power, the optical power measured just outside the cavity mirrors can be calculated (see Chapter 2) and is given by the following forms:

(Reflected pump:)

$$P_{1p} = \begin{cases} \left[\sqrt{R_{1p}} - \frac{T_{1p}\sqrt{R_{2p}}}{1-\sqrt{R_{1p}R_{2p}}} \right]^2 P_{ep}, & \text{if } P_{ep} < P_{th}; \\ \left[\frac{\sqrt{\frac{1}{4}T_{1p}(-\ln\sqrt{R_{1s}R_{2s}})P_0 - \sqrt{R_{1p}P_{ep}}}}{\sqrt{R_{1p}}} \right]^2, & \text{if } P_{ep} \geq P_{th}. \end{cases} \quad (3.9)$$

(Transmitted pump:)

$$P_{2p} = \begin{cases} \frac{T_{1p}T_{2p}}{(1-\sqrt{R_{1p}R_{2p}})^2} P_{ep}, & \text{if } P_{ep} < P_{th}; \\ \frac{1}{4}T_{2p}(-\ln\sqrt{R_{1s}R_{2s}})P_0, & \text{if } P_{ep} \geq P_{th}. \end{cases} \quad (3.10)$$

(Front(back) Stokes:)

$$P_{1s(2s)} = \begin{cases} 0, & \text{if } P_{ep} < P_{th}; \\ \frac{1}{4} T_{1s(2s)} \frac{\lambda_p}{\lambda_s} \left[2 \sqrt{\frac{T_{1p} P_0 P_{ep}}{(-\ln \sqrt{R_{1s} R_{2s}})}} + \ln \sqrt{R_{1p} R_{2p} P_0} \right], & \text{if } P_{ep} \geq P_{th}. \end{cases} \quad (3.11)$$

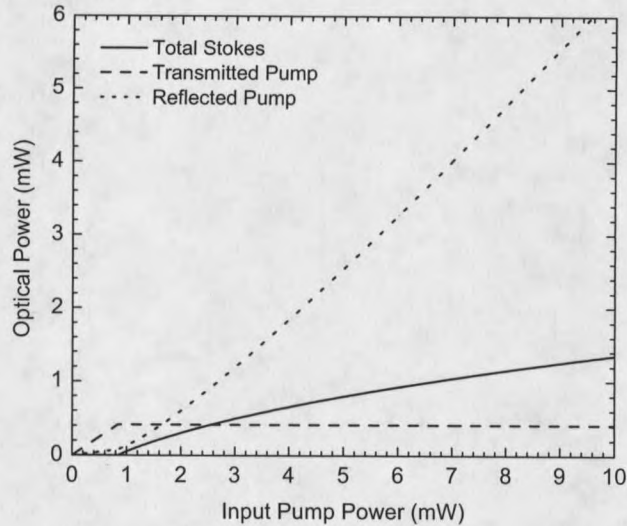


Figure 24 Theoretically calculated optical powers measured outside the cavity as functions of input pump power. The calculation parameters are the same as used in Fig.23. We add the Stokes powers in front and back of the cavity to obtain the total Stokes power.

We plot them as functions of input pump power in Fig. 24 using the same parameters as used in Fig. 23. One can see that the Stokes power grows and the transmitted pump clamps after the threshold; this is the same dependence as with the intra-cavity power. However, the reflected pump power grows quickly as the input pump increases. Certainly this is not a very efficient system in regards to Stokes conversion: a large percent of the pump photons are reflected away from the cavity and cannot contribute to the Stokes conversion. Next we will discuss the method of improving the Stokes conversion efficiency.

Stokes conversion efficiency and cavity impedance-matching

We define a photon conversion efficiency of the cw Raman laser:

$$\eta = \frac{\lambda_s P_{1s} + P_{2s}}{\lambda_p P_{ep}}. \quad (3.12)$$

Using the same parameters as used in Fig. 23, we plot η as a function of input pump power in Fig. 25.

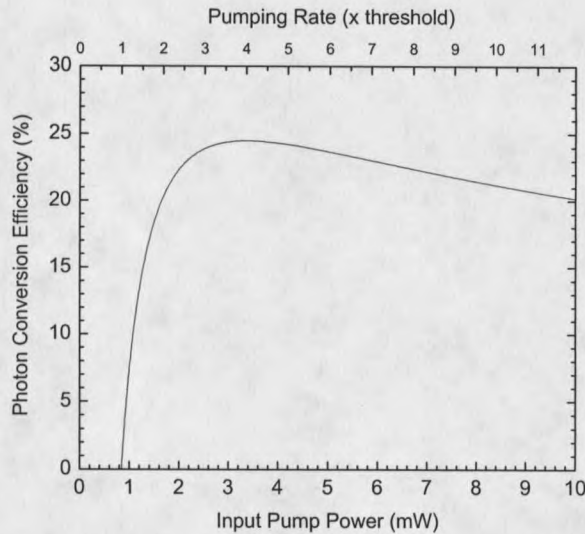


Figure 25 Theoretically calculated photon conversion efficiency as a function of input pump power. The top x axis labels the pumping rate normalized to the laser threshold. Parameters for calculation are the same as used in Fig.23. Photon conversion efficiency reaches the maximum value at 4 times threshold.

The rather low conversion efficiency (maximum value $\sim 25\%$) in Fig. 25 is directly linked to the high reflected pump power as shown in Fig. 24. As shown in Fig. 26, when the input pump laser is resonant with the cavity, the total reflected pump field is a destructive interference between the directly-reflected pump field from the front

mirror (labeled as field 2) and the cavity leakage field out of the front mirror (labeled as field 3). In general, for a symmetric cavity ($R_{1p} = R_{2p}$) without intra-cavity Raman medium, the fields 2 and 3 have the same amplitude. The total reflected pump field is therefore zero; the cavity is termed “impedance-matched” [41]. However, when the intra-cavity pump field is depleted due to the Raman conversion, the field 3 becomes smaller. Therefore the total reflected pump field is no longer zero (impedance-mismatched). The more the pump laser is converted into the Stokes, the higher is the total reflected pump power.

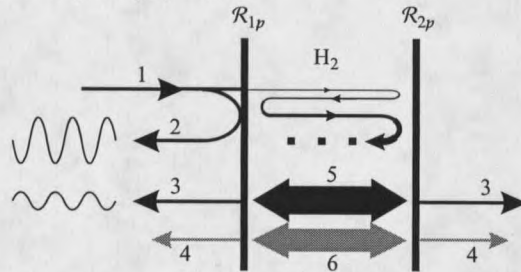


Figure 26 Various optical fields associated with a high-finesse Raman cavity. Field 1: input pump; 2: directly-reflected pump field from the front mirror; 3: cavity leakage pump field; 4: cavity leakage Stokes field; 5: intra-cavity pump field; 6: intra-cavity Stokes field. Field 2 and 3 have 180° phase difference; thus the total reflected pump field is the destructive interference between these two fields.

The way to achieve impedance-matching of the Raman active cavity is to decrease the front mirror’s reflectance at the pump wavelength (therefore increasing the transmittance). In this way the cavity-leakage pump field from the front mirror has larger amplitude and at some point above the Raman threshold the field 2 and 3 in Fig. 26 will be perfectly destructive-interferenced, which results in zero reflected

pump field. In the impedance-matched condition, all the pump light can enter the cavity for Stokes conversion and the conversion efficiency is improved. This idea has been realized theoretically in the field of intra-cavity second-harmonic generation (SHG) [41] in 1966. Later, by use of this concept, $> 80\%$ conversion efficiency has been demonstrated in SHG[42] and optical parametric oscillator[43] systems.

To confirm this impedance-matching concept, we recalculate Eq. (3.9) through Eq. (3.12) using the same parameters as used in Figs. 23-25 except that the front mirror's reflectance is lowered to 0.998. The results are plotted in Fig. 27. In Fig. 27a, the reflected pump power starts to drop once the threshold is reached; the pump field is reaching impedance-matched condition. In Fig. 27b, a maximum photon conversion efficiency of $\sim 66\%$ is reached at four times threshold. Compared with the symmetric pump cavity (Fig. 24 and 25), in this case of asymmetric pump cavity, the threshold has 4-fold increase due to its smaller finesse but the Stokes conversion is more efficient.

In Fig. 25 and 27b, we note that the maximum conversion efficiency happens at 4 times threshold. Mathematically, this behavior can be proved by differentiating Eq. (3.12) (plugging in Eq. (3.11)) with respect to the input pump power P_{ep} and equating to zero[39]. Substituting $P_{ep} = 4P_{th}$, Eq. (3.3) and Eq. (3.11) into Eq. (3.12), we find that the maximum photon conversion efficiency is given by

$$\eta_{\max} = \frac{1}{4} \frac{(T_{1s} + T_{2s})T_{1p}}{\ln \sqrt{R_{1s}R_{2s}} \cdot \ln \sqrt{R_{1p}R_{2p}}} \quad (3.13)$$

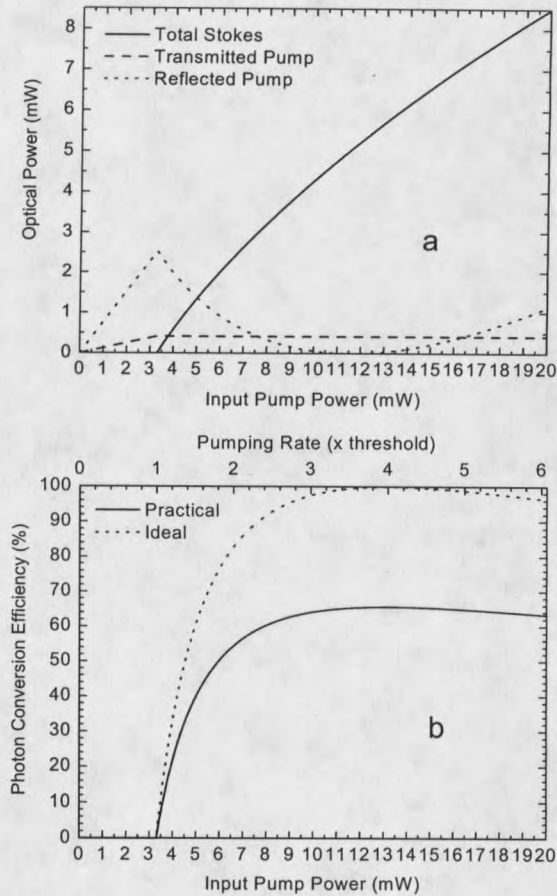


Figure 27 Behaviors of asymmetric pump cavity ($R_{1p} = 0.998$, $R_{2p} = 0.9999$) predicted by the theory. a, Stokes and pump fields as functions of input pump power; b, photon conversion efficiency as a function of input pump power. Above the threshold (3.3 mW), the reflected pump power decreases to approach the impedance-matched condition. The Stokes photon conversion efficiency reaches a maximum value of $\sim 66\%$ at four times threshold. Ideally, if we let all the mirror losses be zero and $R_{2p} = 1$, 100% photon conversion efficiency can be reached (dotted line in b).

Eq. (3.13) tells us that the maximum photon conversion efficiency is only determined by the cavity mirrors' reflectance and transmittance. Furthermore, from Eq. (3.13), it can be shown [39, 44] that in the case of $R_{1p} = R_{2p}$, $\eta_{\max} \rightarrow 50\%$ in the limit of small mirror losses. We name this type of cavity as "symmetric pump cavity". On the other hand, in the case of $R_{1p} < R_{2p}$ ("asymmetric pump cavity"),

$\eta_{\max} \rightarrow 100\%$ when $R_{2p} \rightarrow 1$ and the mirror losses are small.

Tuning characteristics

As introduced in Chapter 1, the cavity's high-finesse bandwidth covers both the pump and the Stokes wavelengths. Therefore the cw Raman laser is a double-cavity-resonance system as illustrated in Fig. 28. The pump laser is always stabilized to a cavity longitudinal mode by the locking electronics; the Stokes field will then build automatically on the cavity resonance nearest to its gain line-center. In this subsection we study the behavior of the Stokes output when the pump laser's frequency is continuously tuned [45].

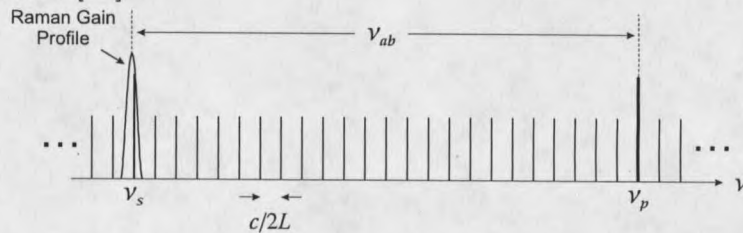


Figure 28 Picture of cavity longitudinal modes in a cw Raman laser and how the Stokes field chooses a lasing mode. Frequency distance ν_{ab} between pump and Stokes gain line-center is the Raman shift. $c/2L$ is the cavity longitudinal mode spacing or the free-spectral-range (c : light speed, L : cavity length). This cavity mode picture was first viewed by Roos.

When the pump laser's frequency is tuned, the cavity's length is also tuned by the locking electronics to maintain the pump resonance. The Stokes' frequency is then automatically changed to satisfy the new cavity resonance. If the pump frequency is tuned by $\delta\nu_p$, the Raman gain line-center is also moved by the same amount since

the Raman shift ν_{ab} is a fixed value. The Stokes resonance, however, is tuned by a smaller amount:

$$\delta\nu_s = \frac{\lambda_p}{\lambda_s} \cdot \delta\nu_p, \quad (3.14)$$

where λ_p and λ_s are the pump and Stokes wavelength respectively. The Stokes tuning relative to the Raman gain line-center, or the two-photon detuning, as a function of $\delta\nu_p$ is then given by

$$\begin{aligned} \Delta(\delta\nu_p) &= \Delta_0 + \delta\nu_s - \delta\nu_p \\ &= \Delta_0 - \left(1 - \frac{\lambda_p}{\lambda_s}\right)\delta\nu_p, \end{aligned} \quad (3.15)$$

where Δ_0 is the initial two-photon detuning (i.e., before the amount of $\delta\nu_p$ is tuned). Based on above analysis and the picture given in Fig. 29, one can imagine that as the pump frequency is tuned, the Stokes resonance can be “scanned” through the entire Raman gain profile.

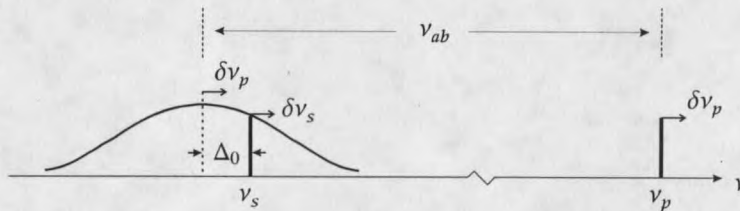


Figure 29 Tuning picture of the cw Raman laser. Initially the Stokes cavity resonance ν_s has an arbitrary detuning of Δ_0 away from the Raman gain line-center. As the pump frequency ν_p is tuned by $\delta\nu_p$, the Stokes gain line-center is tuned by the same amount. However the frequency change of the Stokes cavity resonance is smaller: $\delta\nu_s < \delta\nu_p$. Thus in this picture the Stokes resonance will be tuned closer to the Raman gain line-center.

Eq. (3.15) is for one Stokes resonance (longitudinal mode). If we label all the

Stokes longitudinal modes by i , then for an arbitrary i th mode, Eq. (3.15) can be modified as

$$\Delta^i(\delta\nu_p) = \Delta_0^i - \left(1 - \frac{\lambda_p}{\lambda_s}\right)\delta\nu_p, \quad (3.16)$$

where the initial detunings Δ_0^i for these modes are separated by the Stokes longitudinal mode-spacing (or cavity free-spectral-range (FSR) at the Stokes wavelength):

$$\Delta_0^i = \Delta_0^{i-1} + \text{FSR}. \quad (3.17)$$

As derived in Chapter 2, the Raman plane-wave gain coefficient is a function of the two-photon detuning and has a Lorentzian lineshape:

$$\alpha_g(\Delta) = \alpha_g(0) \frac{(\Gamma/2)^2}{(\Gamma/2)^2 + \Delta^2}, \quad (3.18)$$

where values of the peak gain $\alpha_g(0)$ and the FWHM linewidth Γ have been given in Fig. 22. Substituting Eq. (3.16) into (3.18) we obtain the plane-wave gain coefficient associated with a Stokes cavity resonance as the function of the pump frequency tuning:

$$\alpha_g^i(\delta\nu_p) = \alpha_g(0) \frac{(\Gamma/2)^2}{(\Gamma/2)^2 + \left[\Delta_0^i - \left(1 - \frac{\lambda_p}{\lambda_s}\right)\delta\nu_p\right]^2}. \quad (3.19)$$

Again, here the superscript i means the gain "seen" by the i th Stokes longitudinal mode. Using the values for 792 nm pump laser and for 10 atm H_2 at room temperature: $\alpha_g(0) = 1.5 \times 10^{-9}$ cm/W, $\Gamma = 500$ MHz, $\lambda_s = 1180$ nm and assuming $\Delta_0^i = 0$ when $\delta\nu_p = 0$, we plot Eq. (3.19) in Fig. 30.

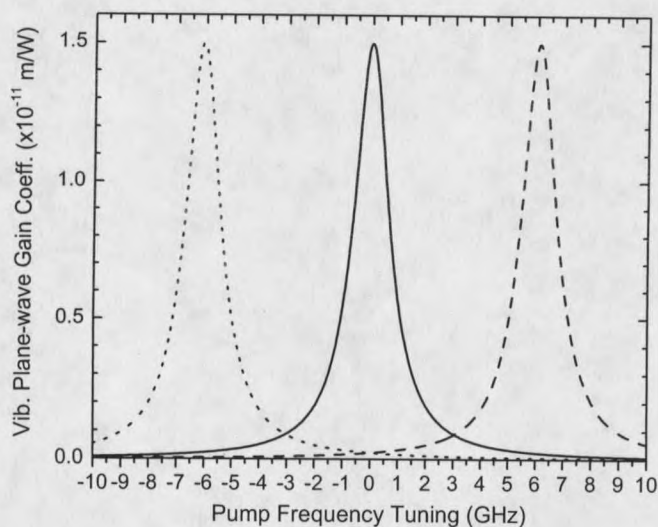


Figure 30 The gain “seen” by three adjacent longitudinal Stokes modes as the pump laser’s frequency is tuned. The Stokes longitudinal mode-spacing is assumed to be 2 GHz. For the center Stokes mode, we assume its initial detuning $\Delta_0 = 0$ when $\delta\nu_p = 0$.

Three Stokes longitudinal modes (i and $i \pm 1$) are calculated and plotted in Fig. 30; their mode-spacing is assumed to be 2 GHz. It can be seen that when one Stokes mode is on the gain line-center, we need to tune the pump frequency by 6 GHz to move the next Stokes resonance to the line-center.

The tuning characteristics of the cw Raman laser can be obtained by substituting Eq. (3.19) into Eq. (3.4) and then into Eqs. (3.9) through (3.11). We plot these pump and Stokes powers as functions of the pump frequency tuning in the case of symmetric pump cavity (Fig. 31) and in the case of asymmetric pump cavity (Fig. 32). Both figures plot for only one Stokes longitudinal mode, which is assumed to be on the gain line-center when the pump frequency tuning is zero.

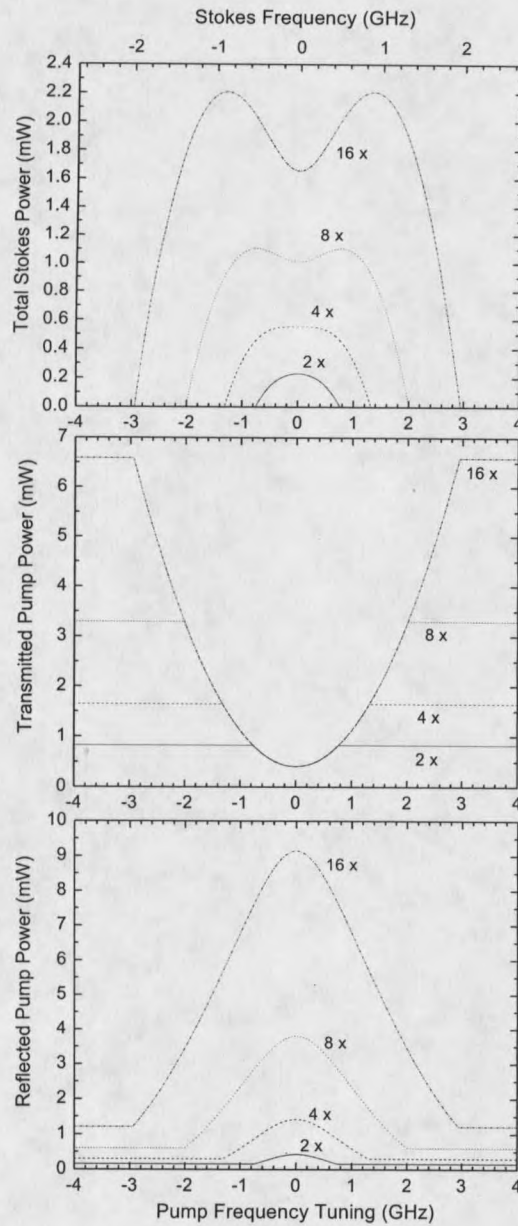


Figure 31 Tuning characteristics of the cw Raman laser in symmetric pump cavity. We calculate the total Stokes power (top), the transmitted pump power (middle) and the reflected pump power (bottom) as functions of the pump frequency tuning. Four different pumping rates, 2 \times , 4 \times , 8 \times , and 16 \times the line-center threshold are plotted. Parameters used for calculation are the same as those used in Fig. 24 and 25.

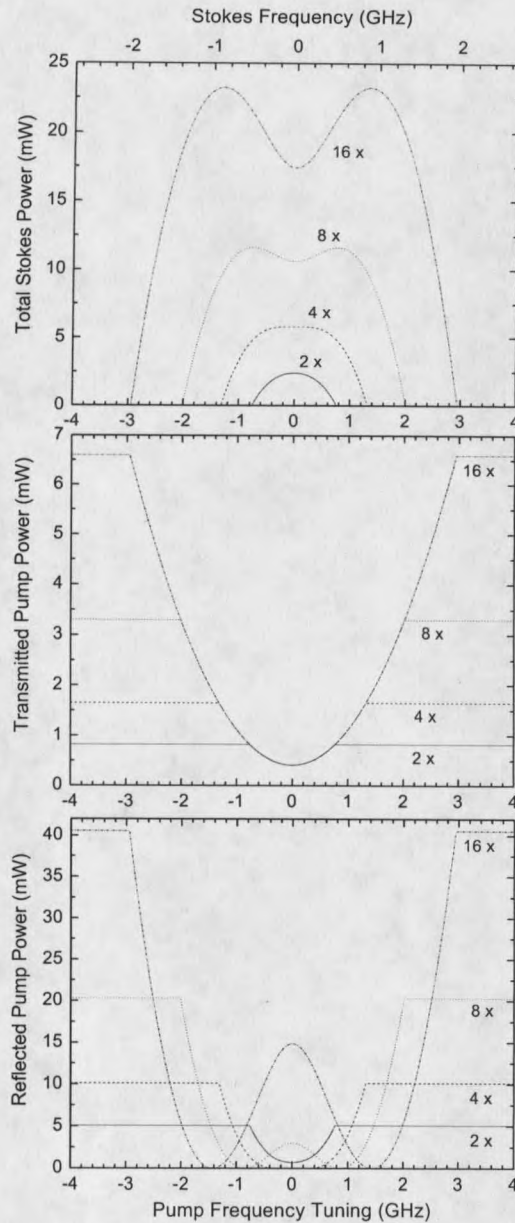


Figure 32 Tuning characteristics of the cw Raman laser in asymmetric pump cavity. Parameters used for calculation are the same as those used in Fig. 27.

Let us address some tuning characteristics of the cw Raman laser. For the output Stokes power, (1) it reaches maximum when the Stokes resonance is on the gain line-center when the pumping rate is equal or smaller than four times the line-center's

threshold; however (2) the Stokes power has a dip on the gain line-center when the pumping rate is greater than four times line-center threshold. This effect is due to the fact that the Stokes conversion efficiency reaches a maximum at a pumping rate of four times threshold. When the pumping rate is greater than this, detuning away from the line-center decreases the pumping rate (increases the threshold) and the Stokes conversion is counterintuitively increased.

For the transmitted pump powers, no matter how large the pumping rate is, they are all depleted to the same value as long as the laser is above threshold. This agrees with the clamping effect in Fig. 24. For the reflected pump powers, in the case of the symmetric pump cavity, they rise when the Stokes resonance is tuned toward the gain line-center due to the increasing impedance-mismatch. In the case of the asymmetric pump cavity, on the contrary, the reflected pump powers drop on the way tuning toward the line-center and reach zero whenever the impedance-mismatch is realized (happens at *about* four times threshold).

It is useful to find the maximum continuous-tuning range of the Stokes output at a given pumping-rate. From Eq. (3.3) and Eq. (3.18), we obtain

$$P_{\text{th}}(\Delta) = P_{\text{th}}(0) \frac{(\Gamma/2)^2 + \Delta^2}{(\Gamma/2)^2}, \quad (3.20)$$

where $P_{\text{th}}(0)$, referred to as "line-center threshold", is the Stokes threshold when $\Delta = 0$ (i.e., when the Stokes resonance is at the gain line-center). This equation tells us that as the Stokes resonance is tuned away from the line-center, the Stokes threshold rises. If initially the Stokes resonance is at the gain line-center and we start

to detune it, the Stokes output will not be turned off until the input pump power is equal to the threshold [$P_{ep} = P_{th}(\Delta)$]. At this time we obtain half of the maximum continuous-tuning range. Substituting this condition into Eq. (3.20), dividing both sides by $P_{th}(0)$ and then solving for Δ , we obtain

$$\Delta_{\max} = \frac{\Gamma}{2} \sqrt{\mathcal{R}(0) - 1}, \quad (3.21)$$

where $\mathcal{R}(0) = P_{ep}/P_{th}(0)$ is the pumping rate relative to the line-center threshold. Δ_{\max} is the two-photon-detuning corresponding to half of the maximum Stokes continuous-tuning range. Using Eqs. (3.14) and (3.15), we obtain that the maximum Stokes continuous-tuning range is given by

$$\delta\nu_{s,\max} = \frac{\Gamma}{\lambda_s/\lambda_p - 1} \sqrt{\mathcal{R}(0) - 1}. \quad (3.22)$$

For the 792→1180 nm vibrational transition, the FWHM linewidth $\Gamma = 500$ MHz, at 4 times the line-center threshold, the maximum Stokes continuous-tuning range is calculated to be 1.77 GHz.

Experiments

In this section we will present the experiments on the diode-pumped cw vibrational Raman lasers (CWWRL).

ECDL pumped, widely tunable

In this experiment, the pump laser is a home-made external-cavity diode laser (ECDL) (designed and made by Gregg Switzer). A 100 mW diode laser with a center

wavelength of 792 nm (SDL-5410) is placed in a Littman-style external cavity [46]. The output of the laser is a single-longitudinal mode with 50 dB side-mode suppression ratio. The output wavelength can be tuned over an 18 nm range from 789 to 807 nm by adjustment of the external-cavity length (rough tuning by hand-adjusting a screw or fine tuning by changing the voltage applied on a piezo-electric transducer (PZT) stack). The tuning capability is not perfect: mode-hops occur for roughly every 20 GHz continuous tuning because the front-facet of the diode is not anti-reflection coated. However this limited continuous tuning range is more than sufficient for tuning over the entire vibrational Raman gain linewidth.

The high-finesse cavity (HFC) is a non-confocal type Fabry-Perot cavity. The two mirrors have a radius of curvature of 50 cm and the mirror-spacing is three inches (7.62 cm) separated by 3 PZT tubes. The cavity's free-spectral-range is thus $\text{FSR} = 1.97 \text{ GHz}$ and the confocal parameter is $b = 26.5 \text{ cm}$. The mirror reflectance and absorption quoted by the manufacturer (Research ElectroOptics, Inc.) are $R = 0.99995$ and $A < 15 \times 10^{-6}$ respectively at both the pump (792 nm) and the vibrational Stokes (1180 nm) wavelengths. The HFC is enclosed within a hermetically sealed container that can hold at least 10 atm of H_2 gas.

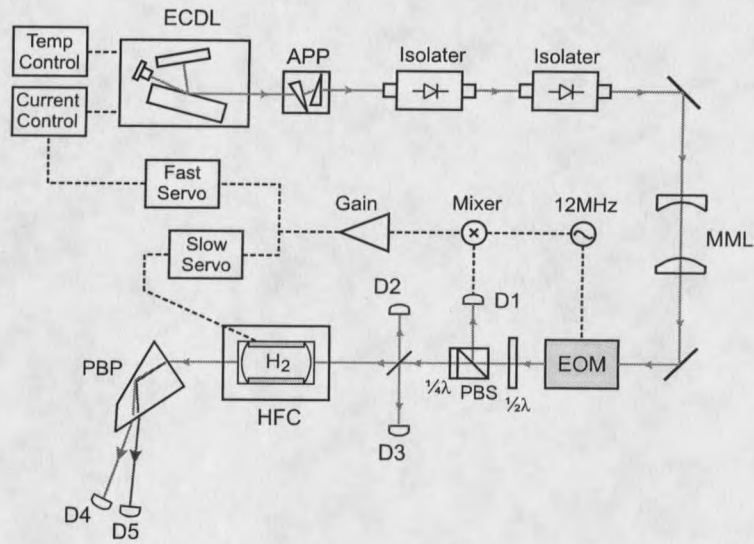


Figure 33 Experimental setup of the ECDL-pumped vibrational Raman laser. ECDL: external-cavity diode laser; APP: anamorphic prism pair; MML: mode-matching lenses; EOM: electrooptic modulator; $\frac{\lambda}{2}$: half-wave plate; PBS: polarizing beam splitter; $\frac{\lambda}{4}$: quarter-wave plate; HFC: high-finesse cavity; PBP: Pellin-Broca prism.

Figure 33 illustrates the experimental setup. An anamorphic prism pair is used right after the ECDL to correct the diode laser's elliptical spatial profile. Two Faraday isolators are used to minimize optical feedback to the ECDL (total isolation is about 60 dB). The laser beam is mode-matched into the HFC by two mode-matching lenses [47]. A beam splitter with 5% reflectance is used before the cavity to monitor the input pump power (detector D3) and the reflected pump power (detector D2). Two other detectors, D4 and D5, are put behind the cavity along with a Pellin-Broca prism to measure the powers of the transmitted pump and the output Stokes.

The rest of the optics and all the electronics are for stabilizing the laser to a resonance of the cavity. We use the Pound-Drever-Hall (PDH) locking technique [48]. An electro-optic modulator (EOM) is driven by a home-made rf sine-wave generator (see

Appendix A); this adds 12 MHz frequency side-bands on the optical carrier frequency. There are a quarter-wave plate and a polarizing beam splitter (PBS) in tandem placed before the HFC. This allows for a photodetector (labeled D1) to receive the reflected light from the front mirror of the HFC. When the laser frequency is near the cavity resonance, the beat signal between the reflected sidebands and the reflected carrier is an amplitude-modulated (AM) sine-wave oscillating at 12 MHz, whose amplitude contains the resonance information, i.e., which side the carrier frequency is relative to the cavity resonance and how far it is from the resonance. The photo-detector D1 receives this AM 12-MHz signal and sends it to an electronic mixer (Mini-Circuits, ZRPD-1). The mixer amplitude-demodulates this signal by multiplying it with the original "clean" 12 MHz sine-wave which drives the EOM. Therefore the mixer produces a dc voltage fluctuation; its sign tells which side the laser's frequency is relative to the cavity resonance and its amplitude tells how far the laser is from the cavity resonance. This signal is named as the error signal. Appendix A gives mathematical details of how the error signal is produced.

Obtaining the error signal, we are able to stabilize the laser's frequency to a resonance of the cavity. Two electronic servos receive the error signal. The fast servo feeds the error signal back to the ECDL's current controller for fast corrections to the laser's frequency (from dc to ~ 1.4 MHz). At the same time the slow servo sends feedback to the HFC's PZT to adjust the cavity length slowly (from dc to ~ 1.5 kHz). With appropriate servo responses [49, Chapter 27] the ECDL and the HFC can be

locked stably.

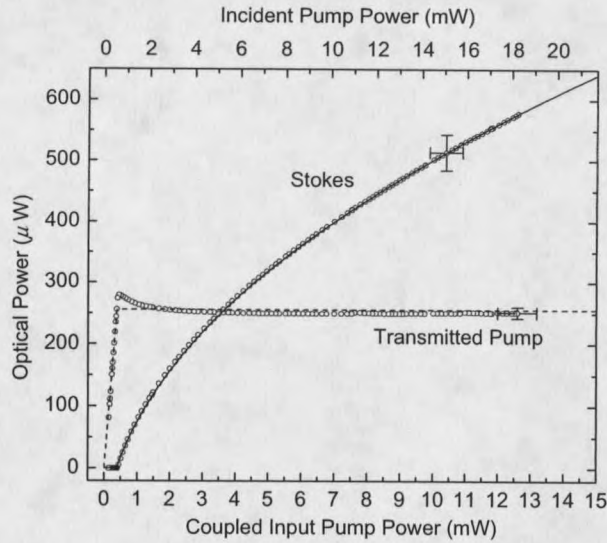


Figure 34 Experimental data of the ECDL-pumped vibrational Raman laser. The Stokes power and the transmitted pump power are measured as functions of the input pump power. The lines are the theoretical fits.

Experimental data of the ECDL-pumped vibrational Raman laser are shown in Fig. 34-36. Fig. 34 shows the total Stokes power and the transmitted pump power as functions of the input pump power. The cavity coupling efficiency is estimated to be approximately 70%. The threshold is measured to be $550 \pm 30 \mu\text{W}$ of the incident pump power, or $385 \pm 30 \mu\text{W}$ of the coupled input pump power. The curves in Fig. 34 are the theory fits using Eq.(3.10) and (3.11). The following parameters are used for the fitting: $R_{1p} = 0.99995$, $R_{2p} = 0.99994$, $R_{1s} = 0.99991$, $R_{2s} = 0.99991$, $A_{1p} = 9 \times 10^{-6}$, $A_{2p} = 11 \times 10^{-6}$, $A_{1s} = 61 \times 10^{-6}$, $A_{2s} = 61.7 \times 10^{-6}$, and $\alpha_g = 1.53 \times 10^{-9} \text{cm/W}$ (the H_2 pressure is approximately 10 atm).

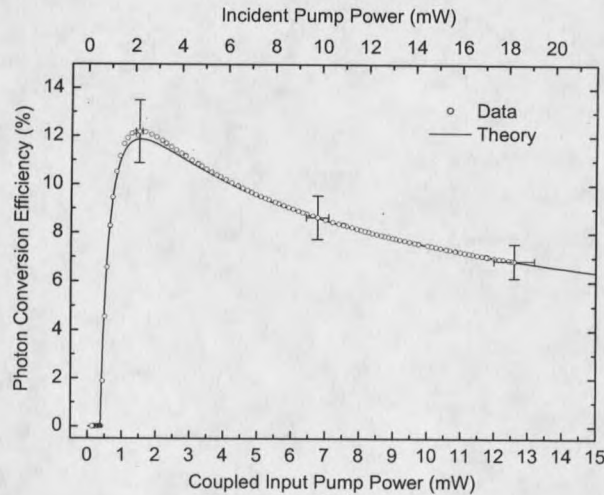


Figure 35 Photon conversion efficiency as a function of input pump power. The maximum efficiency is $(12.0 \pm 1.3)\%$ occurring at four times threshold.

Photon conversion efficiency as a function of the input pump power is shown in Fig. 35. The maximum efficiency is $(12.0 \pm 1.3)\%$ occurring at four times threshold. The reason for this rather low efficiency is due to the use of a symmetric pump cavity, as discussed in the last section.

This cw Raman laser exhibits wide discrete tunability in the near infrared. The ECDL's 789-807 nm wavelength range results in vibrational Stokes emissions from 1174-1214 nm. This gives a 40 nm wavelength tuning range. Fig. 36 shows the wavelength measurements of the pump and Stokes beams. When we set the pump laser at three different wavelengths (top): 789, 798, and 807 nm, we obtain the Stokes wavelengths (bottom) at 1174, 1194, and 1214 nm, respectively.

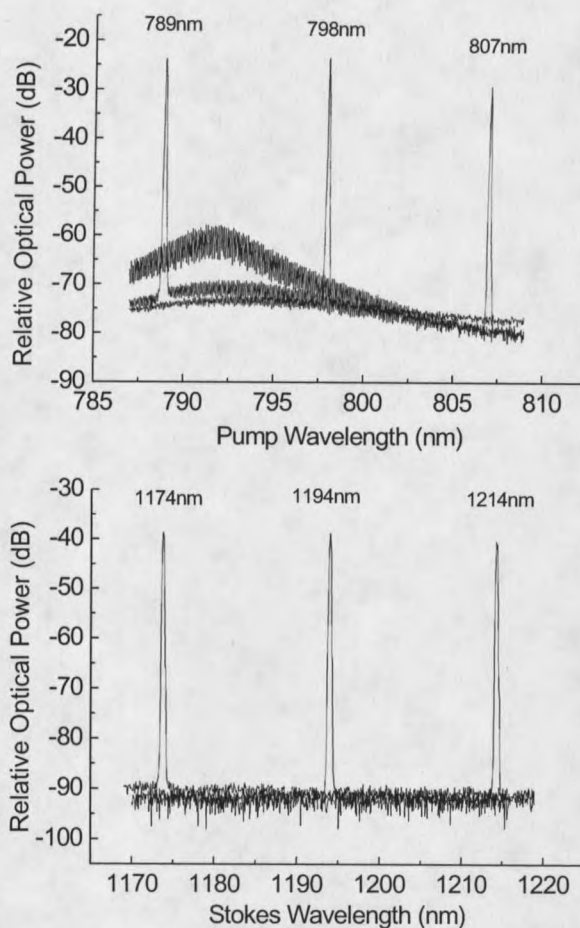


Figure 36 Tunability of the ECDL-pumped vibrational Raman laser. The 18 nm wavelength of the pump beam (top) results in a 40 nm discretely tunable Stokes beam (bottom). The wavelength measurements were taken with a HP optical spectrum analyzer (resolution: 0.1 nm).

It should be noted that a full-range continuous tuning of the Stokes emission is not possible due to the double-resonance requirement. The Stokes output can be continuously tuned in GHz range and is measured in Fig. 37. About 1.3 GHz continuous tuning range is obtained. We note the sharp turn-off of the (vibrational) Stokes output at about ± 1 GHz; this is due to the emission of the rotational Stokes and will be presented in Chapter 3.

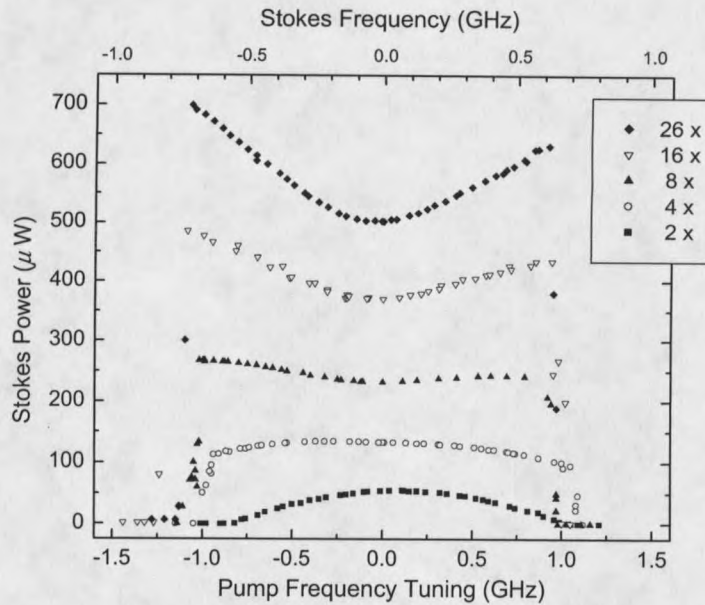


Figure 37 Continuous tuning of the ECDL-pumped vibrational Raman laser. The Stokes power is measured when the pump frequency is tuned (bottom horizontal axis; the Stokes frequency change is shown by the top horizontal axis). We take the measurements at five different pumping rates: 2 \times , 4 \times , 8 \times , 16 \times , and 26 \times the line-center threshold. The Stokes can be continuously tuned by about 1.3 GHz.

Highly efficient cw vibrational Raman laser

The previous ECDL-pumped system exhibits only $\sim 12\%$ photon conversion efficiency. This is because a symmetric pump cavity is used and a large percentage of the pump light is reflected from the cavity (impedance-mismatched) when there is intra-cavity Stokes conversion. To make the Stokes conversion more efficient, one can use an impedance-matched cavity (i.e., zero reflection from the cavity) for the pump field so that all the pump light can enter the cavity for conversion. As shown in an

earlier section in this Chapter (page 72), if the front cavity mirror has an appropriately lower reflectance at the pump wavelength than the back mirror (named as an asymmetric pump cavity), the maximum Stokes photon conversion efficiency can be greatly improved.

However, an asymmetric pump cavity has lower finesse at the pump wavelength thus the Stokes threshold is higher than the symmetric cavity. Due to its limited output power, the ECDL used in Fig. 33 needs to be amplified or replaced by a higher power source. We choose to use the diode-laser injection-locking technique [50]. The ECDL is used as the master laser while a high power free-running diode is used as the slave laser. By means of injection locking, the slave laser's output can preserve the spectral quality of the ECDL but offers higher output power [51]. Two experiments using two different slave diodes have been performed by us: the first one uses a single-mode 100 mW diode; then the second one uses a multi-mode 1.2 W broad-area diode laser (BADL). The first experiment⁵ reaches a photon-conversion-efficiency of $(66 \pm 8)\%$ which gives a peak Stokes output power of 16 mW. The details of this experiment have been given in Ref. [52] and [20]. In this thesis, we will give the details and results of the second experiment: using an injection-locked BADL to pump a highly efficient cw vibrational Raman laser.

5

The very first high conversion efficiency Stokes generation was actually obtained by Roos in his passive-locking cw Raman experiment [19].

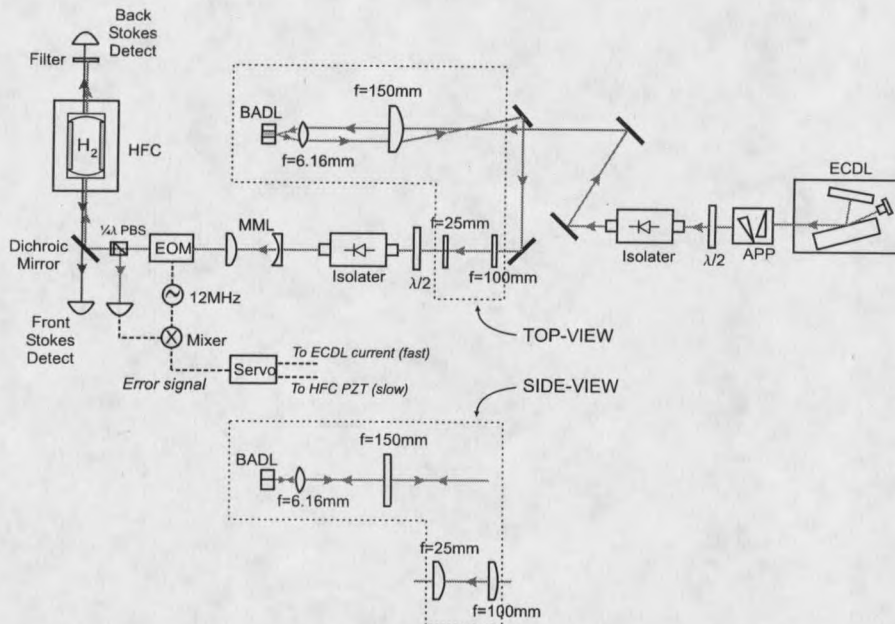


Figure 38 Experimental setup of a highly efficient cw vibrational Raman laser. The pump laser is a broad-area diode laser (BADL) injection-locked by an external-cavity diode laser (ECDL). APP: anamorphic prism pair; $\lambda/2$: half-wave plate; MML: mode-matching lenses; EOM: electrooptic modulator; PBS: polarizing beam splitter; $\lambda/4$: quarter-wave plate; HFC: high-finesse cavity.

Fig. 38 illustrates the experimental setup. The BADL has a front facet size of $100 \times 1 \mu\text{m}$, a free-running output power of 1.2 W and a center wavelength of 795 nm (SDL-2360). To overcome both the spectral and spatial multi-mode properties of a BADL, we injection-lock the BADL (slave) by the output beam from a ECDL (master). The ECDL used here is the same one used in the last section (Fig. 33). Its output beam is first sent through an anamorphic prism pair to circularize its elliptical spatial profile. Then an isolator is used to minimize the optical feedback; a half-wave plate is placed before the isolator's front polarizer for adjusting the injection power. To achieve the best injection-locking, as shown in Fig. 39, the master beam should be

injected into one edge of the BADL front facet by an incident angle of $3-4^\circ$ and the beam waist diameter should be $1/2$ width of the front facet area on the facet plane (i.e., in this case, $50 \times 1 \mu\text{m}$) [8, 9].

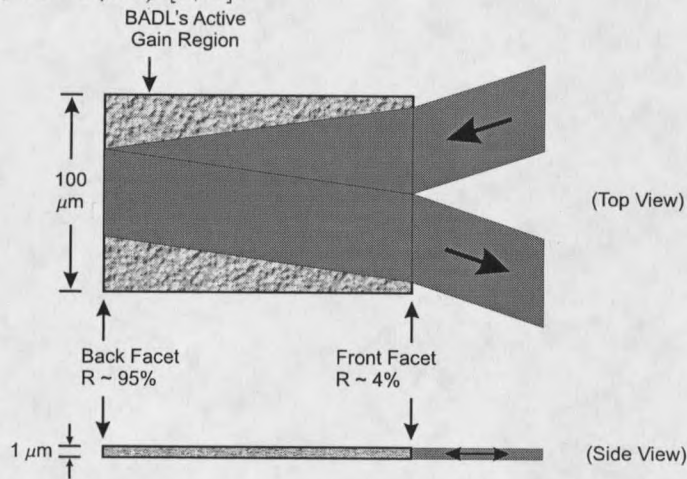


Figure 39 Geometry of the injection into the slave BADL diode. The BADL's facet size is $100 \times 1 \mu\text{m}$. It has been experimentally discovered [8, 9] that the best injection-locking performance is achieved when (1) the master beam is injected into one edge of the BADL front facet by an incident angle of $3-4^\circ$ and (2) the beam waist diameter is $1/2$ width of the front facet area ($50 \times 1 \mu\text{m}$).

These requirements are fulfilled by using a spherical lens of $f=6.16 \text{ mm}$ and a cylindrical lens of $f=150 \text{ mm}$ placed in front of the BADL. For adjusting the injection angle and position, the cylindrical lens is mounted on a translation stage while the BADL and the spherical lens together are placed on a tip-tilt stage. The output beam from the BADL passes through the spherical and the cylindrical lenses again and is picked off by a mirror. Two other cylindrical lenses are used to circularize and collimate the output beam. After an isolator the output beam is finally coupled into the asymmetric pump cavity by use of two mode-matching spherical lenses.

To examine the spectral quality of the output beam from the injection-locked BADL, we send the beam into an optical spectrum analyzer (OSA). Fig. 40a shows the OSA measurements.

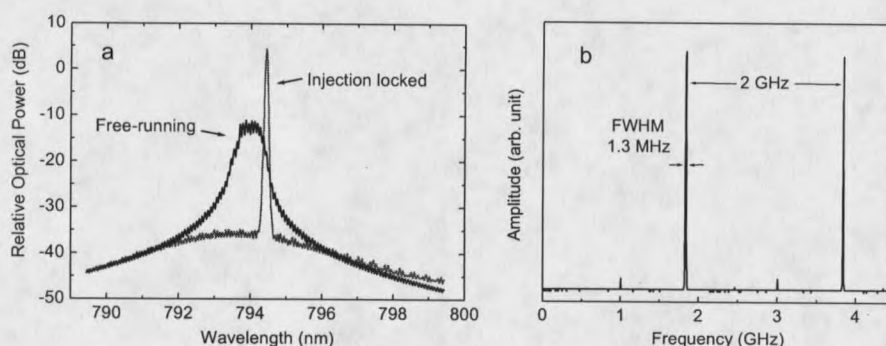


Figure 40 BADL injection-locking results. a, Spectra of BADL's output measured by an optical spectrum analyzer (resolution 0.1 nm) when free-running and injection-locked. b, When injection-locked, the transmitted signal from the scanning Raman HFC (without H_2). The HFC's free-spectral-range is 2 GHz; its linewidth is ~ 1 MHz.

When the BADL is free running without injection, the output has about 2 nm linewidth. After injection-locked by the ECDL, this linewidth is greatly narrowed and has approximately 40 dB side-mode suppression ratio. To examine the linewidth with higher resolution, we measure the signal from the scanned Raman HFC (without H_2 inside). The oscilloscope trace is plotted in Fig. 40b and shows ~ 1.3 MHz FWHM linewidth. This value is comparable to the calculated cavity linewidth (~ 1 MHz FWHM); hence it could still be limited by the resolution of the HFC.

For the spatial beam quality of the injection-locked BADL output, the quantitative measurement such as the M^2 coefficient is not performed. But a coupling efficiency of about 36% is achieved when the output beam is coupled into a single-mode fiber. We also measured $(35\pm 3)\%$ coupling efficiency when the beam is mode-matched into the HFC.

The maximum power from the ECDL that can be used for injection-locking is about 19 mW. With this amount of power injected we obtained ~ 160 mW output from the BADL. This gives a gain factor of about 8, which could be improved with the use of more appropriate lenses and their alignment.

As in the experiment of sole-ECDL pumping (Fig. 33), the same Pound-Drever-Hall locking scheme is used here to stabilize the pump laser's frequency to a resonance of the HFC. The error signal is fed back to slowly correct the cavity mirror-spacing and fastly control the ECDL's supplying current. About 6 atm H_2 gas is filled in the HFC. The pump wavelength 794 nm is shifted to the vibrational Stokes wavelength 1185 nm. When the Stokes cavity resonance is fine-tuned to the Raman gain line-center, the Stokes threshold is measured to be (18.5 ± 2) mW of the coupled input pump power (the cavity coupling efficiency is estimated to be $(35\pm 3)\%$).

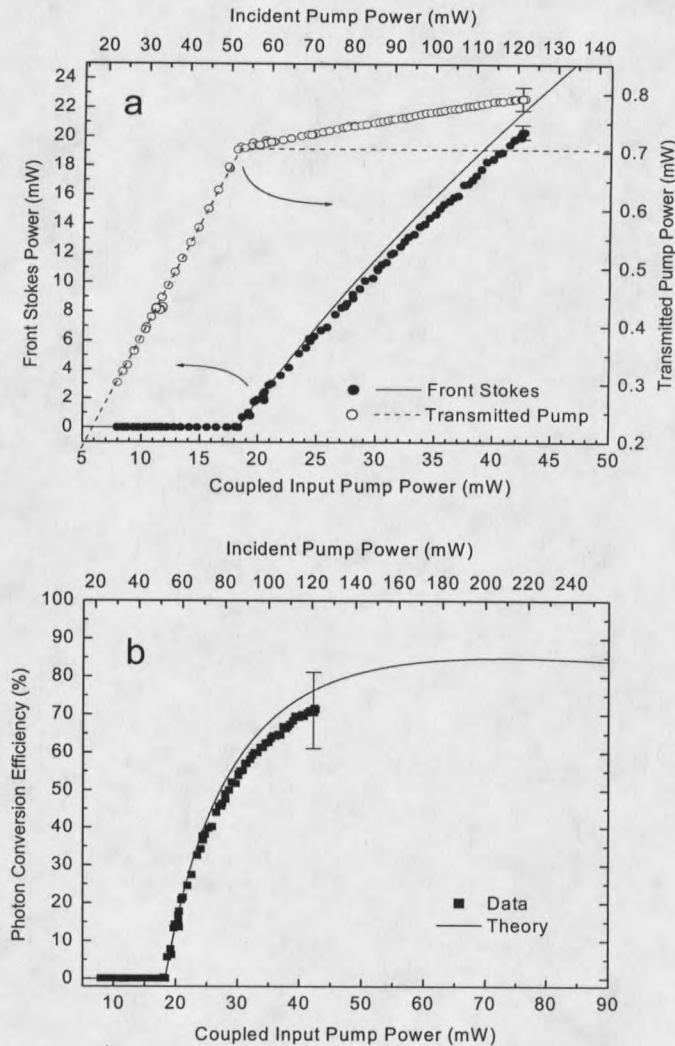


Figure 41 Experimental data of the BADL-pumped vibrational Raman laser. a, The Stokes power and the transmitted pump power are measured as functions of the input pump power. b, Photon conversion efficiency as a function of the input pump power. Curves are the theoretical fits. The deviations between the data and the theory are caused by the thermal lens effect of the Raman gas [10].

Fig. 41a shows the system's output vs. input curves. The output Stokes power in front of the cavity and the transmitted pump power are measured as functions of the input pump power. A peak value of (20.4 ± 0.4) mW Stokes power is obtained. The photon conversion efficiency (front Stokes vs. coupled input pump) is calculated

and is plotted in Fig. 41b. Its peak value reaches $(71 \pm 10)\%$. Since the cavity has an asymmetric mirror transmittance at the Stokes wavelength, only 5% of the total generated Stokes power is in the back of the cavity. If we consider the total Stokes power at both ends of the HFC, the peak value is (21.6 ± 0.5) mW and the peak photon conversion efficiency (total Stokes vs. coupled input pump) reaches $(74 \pm 10)\%$. The 10% uncertainty is mainly due to the uncertainty of the cavity coupling efficiency.

The curves in Fig. 41 are the theoretical fits using Eqs.(3.10) and (3.11). Following parameters are used for the fitting: $R_{1p} = 0.9973$, $R_{2p} = 0.99994$, $R_{1s} = 0.9993$, $R_{2s} = 0.99993$, $A_{1p} = 40 \times 10^{-6}$, $A_{2p} = 32 \times 10^{-6}$, $A_{1s} = 30 \times 10^{-6}$, $A_{2s} = 32 \times 10^{-6}$, and $\alpha_g = 1.35 \times 10^{-9}$ cm/W (the H_2 pressure is approximately 6 atm). There are deviations between the data and the theory: although the theory predicts that the transmitted pump power should remain constant once the system reaches its threshold, the measured value actually rises as the pumping rate increases. The Stokes generation also departs from the theoretical $\sqrt{P_{ep}}$ dependence [Eq. (3.11)], and less Stokes power is produced than predicted. The cause of the observed deviations from the theory is the thermal lens effect of the Raman gas. Because of the nature of the inelastic Raman process, Stokes generation causes heat deposition in the Raman gas and thus changes the refractive index in the cavity. As shown in Ref. [53] the refractive index of H_2 decreases as a function of Stokes field intensity. As a result, the pump beam suffers defocusing — we have measured that beam waists of both the pump and the Stokes light grow slightly with increased Stokes power [10]. Because

of this effect, both the effective Raman gain and the cavity coupling efficiency are reduced and therefore less Stokes power is generated.

Fig. 41b predicts that $> 80\%$ efficiency at a single end of the cavity could be reached if we had higher pump power. The limited pump power from the BADL slave in this experiment is due to the limited power from the master laser and the imperfect injection coupling. Circularization and collimation of the BADL's output beam could also be improved by better beam-shaping techniques so the HFC coupling efficiency can be higher.

The system has some tuning capability. About 1 GHz continuous tuning of the Stokes frequency can be obtained when the ECDL's frequency is tuned. Large-range discrete tuning is also possible but is inconvenient here since a large change of the master laser's frequency causes steering of the BADL's output beam [8]. This is a disadvantage of using an injection-locked BADL to pump any laser system if large tuning is desired.

CHAPTER 4

DIODE-PUMPED CW ROTATIONAL RAMAN LASER

We present in this chapter the experimental achievements of the diode-pumped cw rotational Raman laser.

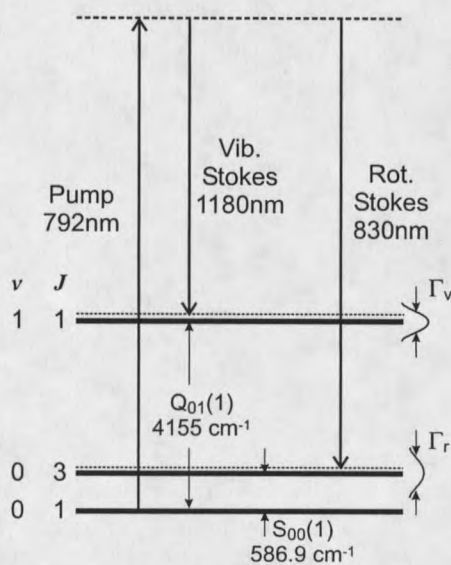
Rotational Raman Transition in H₂Introduction

Figure 42 Energy levels in H₂ showing transitions for both vibrational (1180nm) and rotational (830 nm) Stokes pumped with 792 nm. At room temperature of 300 K and a H₂ pressure of 10 atm, the FWHM Raman gain linewidth of the vibrational transition $Q_{01}(1)$ is $\Gamma_v = 0.5 \text{ GHz}$ and the rotational transition $S_{00}(1)$ has $\Gamma_r = 1.02 \text{ GHz}$.

Fig. 42 shows the energy level diagram in H₂ molecules. The vibrational levels are denoted by quantum number v and the rotational levels are denoted by quantum

number J . At thermal equilibrium and temperature of 300 K, about 67% of the total population is in the $v = 0, J = 1$ level while no more than 14% is in other single states (table 6 in Ref. [38]). So the state $v = 0, J = 1$ is the ground state of our cw Raman laser system. The selection rules for the two-photon Raman transitions are [38]:

$$\Delta v = \pm 1, \quad \Delta J = 0; \quad (\text{pure vibrational transition})$$

$$\Delta v = \pm 1, \quad \Delta J = \pm 2; \quad (\text{vibrational-rotational transition})$$

$$\Delta v = 0, \quad \Delta J = \pm 2. \quad (\text{pure rotational transition})$$

The transitions associated with the cw Raman laser in this thesis are the pure vibrational $Q_{01}(1)$ ($v = 0 \rightarrow 1, J = 1 \rightarrow 1$) and the pure rotational $S_{00}(1)$ ($v = 0 \rightarrow 0, J = 1 \rightarrow 3$), as shown in Fig. 42. The $Q_{01}(1)$ transition with a 4155 nm^{-1} shift gives us the cw vibrational Raman laser; this has been presented in the last Chapter. In this Chapter, we will discuss the cw rotational Raman laser based on the $S_{00}(1)$ transition with a 586.9 nm^{-1} shift.

Rotational Raman linewidth

The rotational Raman gain linewidth of H_2 was studied by Herring, Dyer, and Bischel [7]. The linewidth depends on temperature and H_2 density. It was shown that for densities above a certain cutoff density, the Raman line-shape is Lorentzian (due to pressure-broadening) with a FWHM linewidth Γ_r that can be expressed as

$$\Gamma_r = \frac{A}{\rho} + B\rho, \quad (4.1)$$

where ρ is H_2 density in amagat and the coefficients A and B depend on temperature. For $S_{00}(1)$ transition at 295 K, $A = 6.15\text{MHz}\cdot\text{amagat}$, $B \approx 110\text{MHz}/\text{amagat}$ [7]. That cutoff density for $S_{00}(1)$ transition at 295 K is 0.134 amagat (0.146 atm). Below this cutoff density, Eq. (4.1) cannot be applied; the rotational linewidth is dominated by Doppler broadening and the linewidth should be constant in density.

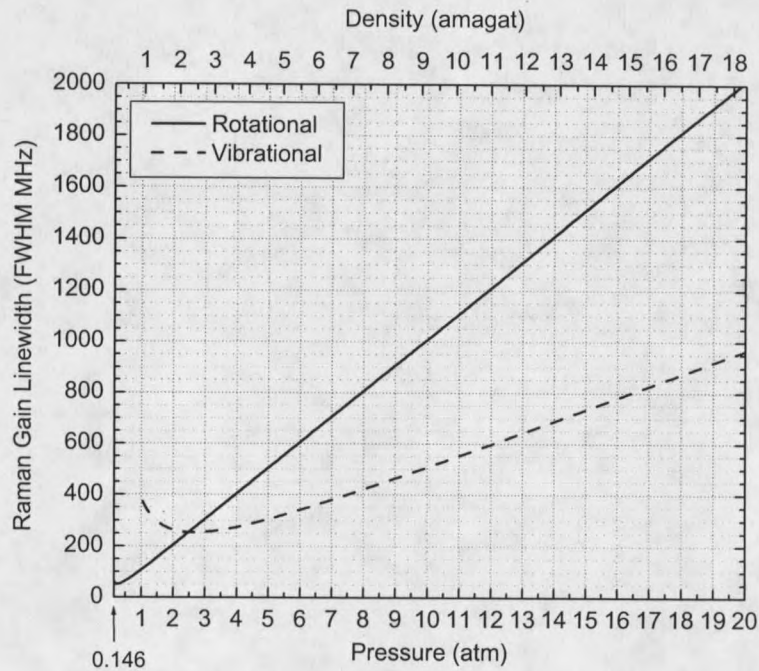


Figure 43 Rotational and vibrational Raman linewidth in H_2 as functions of pressure or density at 295 k. 0.146 atm (0.134 amagat) is the cutoff pressure (density) for the rotational transition, below this density, the rotational linewidth is dominated by Doppler-broadening and Eq. (4.1) cannot be applied. The cutoff density for the vibrational transition is 1 amagat.

From Eq. (4.1), we calculate the linewidth Γ_r as a function of density and then convert density (in amagats) to pressure (in atm) for H_2 at 295 k. The result is plotted in Fig. 43 in a pressure range from 0.146 atm (corresponds to the cutoff density) to

20 atm. For comparison, the vibrational linewidth is also plotted: the rotational transition has a wider linewidth than the vibrational at high pressures.

Rotational Raman gain

The plane-wave gain coefficient for the $S_{00}(1)$ transition in H_2 has not been directly measured. We will have to use some other published data to calculate it. We start from the equation given by Carlsten et al [4]: the peak plane-wave gain coefficient for the rotational transition from level J to level $J + 2$ and for a circularly polarized pump beam is expressed by the form

$$\alpha_g = \frac{8 \pi^2 \omega_s}{5 c^2 n_s^2} \frac{(J+1)(J+2)}{(2J+1)(2J+3)} \frac{(\gamma_{\nu, J; \nu, J+2})^2}{h \Gamma_r / 2} \Delta N, \quad (4.2)$$

where ω_s is the Stokes frequency in radian·Hz, n_s is the refractive index at the Stokes wavelength, $\gamma_{\nu, J; \nu, J+2}$ is the off-diagonal element of the molecular anisotropic polarizability [54, page 42], Γ_r is the rotational Raman linewidth (FWHM), and ΔN is the number density difference between the initial state J and the final state $J + 2$.

First, to find ΔN , it is given by [4]

$$\Delta N = N(J) - \frac{2J+1}{2(J+2)+1} N(J+2), \quad (4.3)$$

where $N(J)$ is the population density in rotational level J . Reference [38] gives the population distribution for H_2 : at a temperature of 300 K, $N(1)/N_{\text{Total}}=0.6675$ and $N(3)/N_{\text{Total}}=0.0812$. Here the total number density N_{Total} counting all the H_2

molecules is

$$\begin{aligned} N_{\text{Total}} &= \rho \cdot \rho_A \cdot N_A = \rho \times 4.4587 \times 10^{-5} \times 6.022 \times 10^{23} \\ &= \rho \times 2.685 \times 10^{19} \text{ (cm}^{-3}\text{)}, \end{aligned} \quad (4.4)$$

where ρ is the H_2 density in amagat, ρ_A is the amagat unit for H_2 : 1 amagat = 4.4587×10^{-5} mole/ cm^3 [1], $N_A = 6.022 \times 10^{23}$ mole $^{-1}$ is Avogadro's number. Thus the number density difference between the initial state $J=1$ and the final state $J+2=3$ as a function of density ρ (in amagat) is given by

$$\begin{aligned} \Delta N(\rho) &= \left(0.6675 - 0.0812 \cdot \frac{2 \cdot 1 + 1}{2 \cdot 3 + 1} \right) \cdot N_{\text{Total}} \\ &= \rho \times 1.699 \times 10^{19} \text{ (cm}^{-3}\text{)}. \end{aligned} \quad (4.5)$$

For other parameters, the rotational linewidth (FWHM) Γ_r is given by Eq. (4.1); the polarizability in the $S_{00}(1)$ transition, $\gamma_{0,1;0,3}^2 = 0.129 \times 10^{-48}$ cm^6 at 488 nm [5]. To convert into the value for our 792 nm pump wavelength, the frequency dependence of the gain can be approximated by [6]

$$\alpha_g \propto \frac{\nu_s}{(\nu_i^2 - \nu_p^2)^2}, \quad (4.6)$$

where ν_s and ν_p are the Stokes and pump frequency respectively, $\nu_i = 8.48 \times 10^4$ cm^{-1} for H_2 is an average transition frequency to excited states.

Knowing these parameters, we are able to give a formula for calculating the peak Raman plane-wave gain coefficient (unit: cm/W) for the rotational transition $S_{00}(1)$

as a function of wavelength and density at room-temperature (295-300 K):

$$\alpha_g = 2.427 \times 10^8 \times \frac{\rho}{\Gamma_r} (\nu_p - 586.9) \times (7.19 \times 10^9 - \nu_p^2)^{-2}, \quad (4.7)$$

where ρ is the density in amagats, Γ_r is the Raman linewidth in MHz given by Eq. (4.1), and ν_p is the pump laser frequency in cm^{-1} .

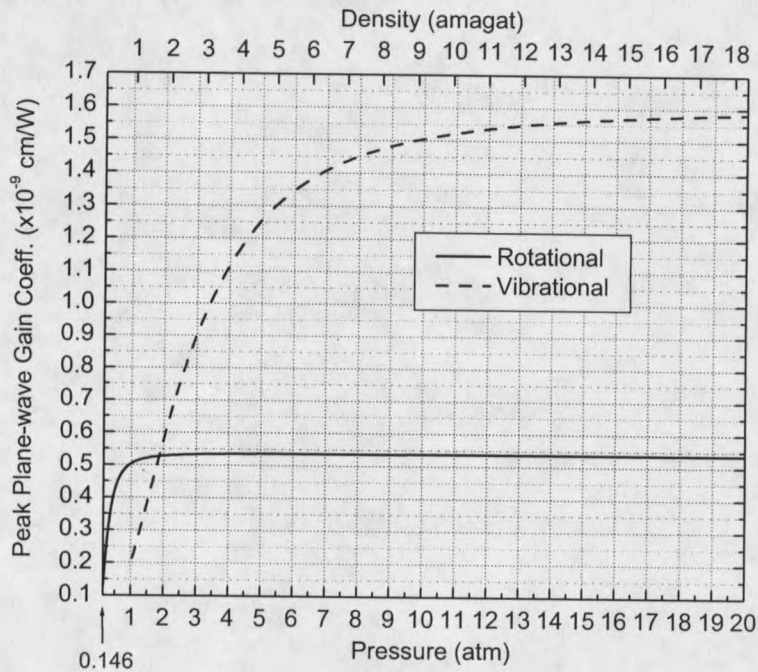


Figure 44 Rotational and vibrational Raman gain in H_2 as functions of pressure or density at room-temperature (295-300 K). Both are calculated for the pump wavelength of 792 nm. The rotational gain is for circularly polarized pump light and counter-circularly polarized Stokes output; while the vibrational gain is independent of pump polarization.

We plot this gain coefficient as a function of H_2 density or pressure in Fig.44 (pump wavelength: 792 nm). Above a high-pressure limit of 2~3 atm, the peak rotational Raman gain is nearly independent of pressure. For comparison, the vibrational gain

is also included.

Polarization dependence

For Raman transitions between purely rotational energy levels of an axially symmetric diatomic molecule such as H_2 , the strength of the Stokes emission is strongly dependent on the polarization of the pump beam. Note that Eq. (4.7) is for circularly polarized pump laser, and the rotational Stokes output is counter-rotating circularly polarized. This polarization condition results in the largest Raman gain. Table 2 gives the relative Raman gains for all the cases of polarizations [22].

Polarization	Pump	Stokes	Relative Gain
Linear	↑	↑	4
	↑	↓	3
Circular	⊙	⊙	1
	⊙	⊙	6

Table 2 Relative rotational Raman gains for different polarization conditions.

On the contrary, for vibrational transitions which involve a large isotropic polarizability, its gain is essentially independent of laser polarization.

Experiment

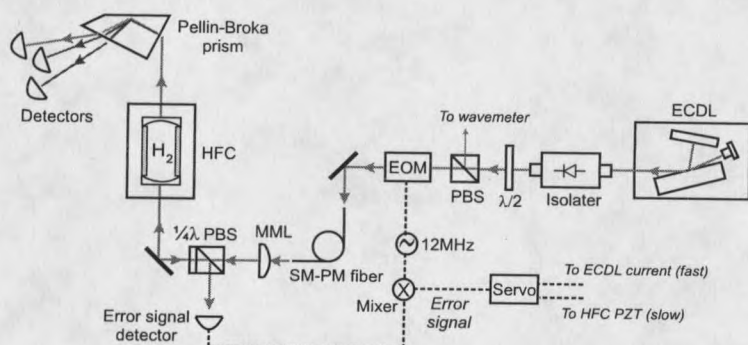


Figure 45 Experimental setup of the ECDL-pumped rotational Raman laser. ECDL: external-cavity diode laser; $\frac{\lambda}{2}$: half-wave plate; PBS: polarizing beam splitter; EOM: electrooptic modulator; SM-PM fiber: single-mode and polarization-maintaining fiber; MML: mode-matching lens; $\frac{\lambda}{4}$: quarter-wave plate; HFC: high-finesse cavity.

As shown in Fig. 45, the experimental setup for generating the rotational Stokes beam is basically identical to the setup used for ECDL-pumped vibrational Raman laser in Chapter 3: both the pump laser and the HFC are the same. This system was targeted for vibrational Stokes generation in H_2 [18] and worked as expected except for only one fact that the vibrational Stokes output exhibited sharp turn-off in the continuous-tuning measurements (see Fig. 46). The cause for that sharp turn-off, the rotational Stokes emission, was not discovered until two years later [11]. After this discovery, we obtained the complete continuous-tuning curve as shown in Fig. 46.

In Fig. 46, as the pump frequency is tuned, the system exhibits sharp switching between the vibrational and rotational Stokes emissions. Each of the two Stokes modes operates in a single longitudinal and spatial cavity mode. These behaviors indicate the homogeneous nature of the Raman gain medium (10 atm H_2).

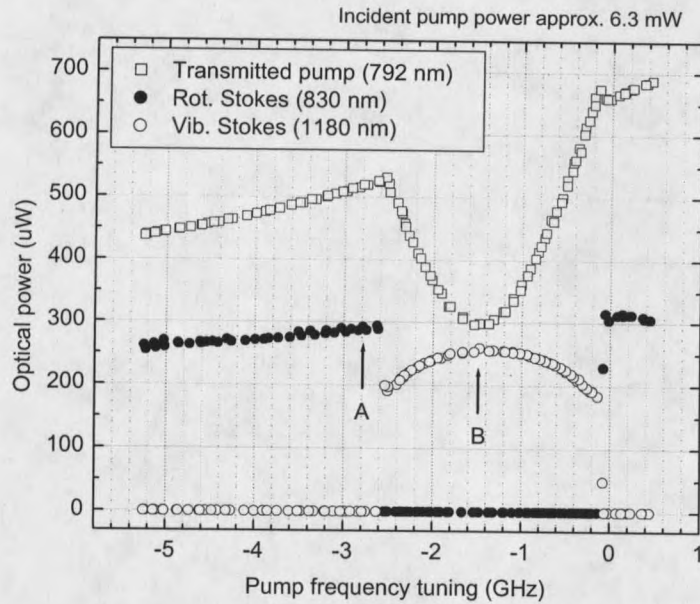


Figure 46 Continuous-tuning data measured from the setup in Fig. 45.

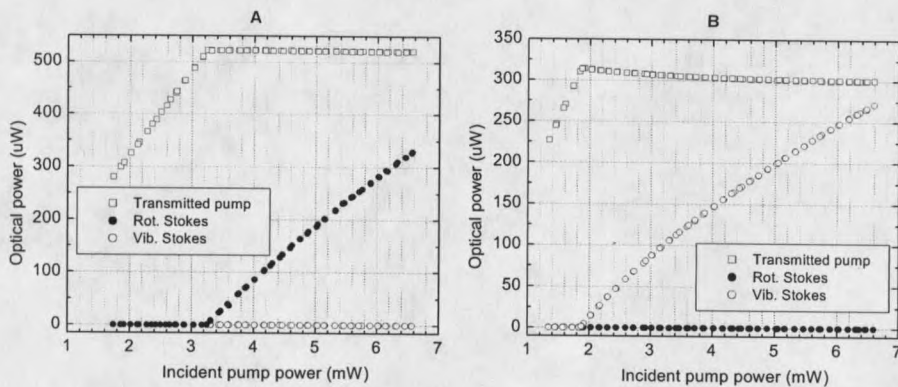


Figure 47 Power dependences measured from the setup in Fig. 45.

Fig. 47 shows the power dependences, i.e., when the pump frequency is tuned to point A and B respectively, we measure the optical powers of the rotational and vibrational Stokes as functions of the input pump power. It can be seen that in both cases the Stokes power grows and the transmitted pump power clamps after the

Raman threshold is reached.

The additional lasing of rotational Stokes at 830 nm indicates that the high-reflective mirror-coating at the 792 nm pump wavelength has a wide bandwidth. Fig. 48 is the mirror transmittance trace provided by the mirror-coating manufacturer (Research Electro-Optics, inc.). It shows that the high-reflective coating at the pump wavelength covers a wide range from ~ 750 nm to ~ 890 nm. This fact gives us an advantage of the cw rotational Raman laser: the bandwidth of a single-wavelength mirror coating can be sufficient to cover both the pump and rotational Stokes wavelengths, whereas the double-wavelength coating required for the vibrational cw Raman laser is far more expensive and difficult to manufacture.

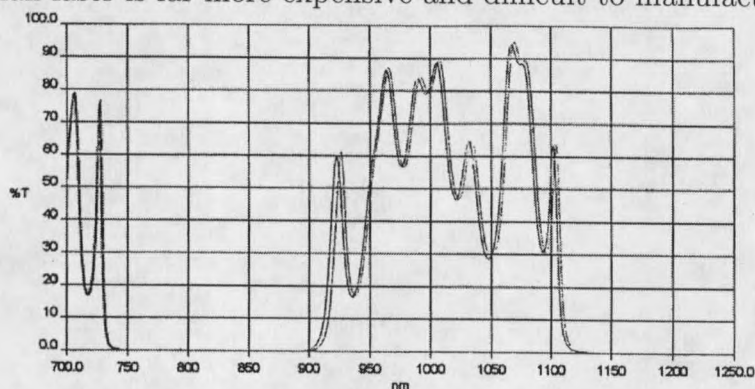


Figure 48 HFC-mirror transmittance trace provided by the mirror-coating manufacturer (Research Electro-Optics, inc.). The double-wavelength coating at 792 and 1180 nm is originally manufactured for the cw vibrational Raman laser, but the wide coating bandwidth also covers the rotational wavelength at 830 nm.

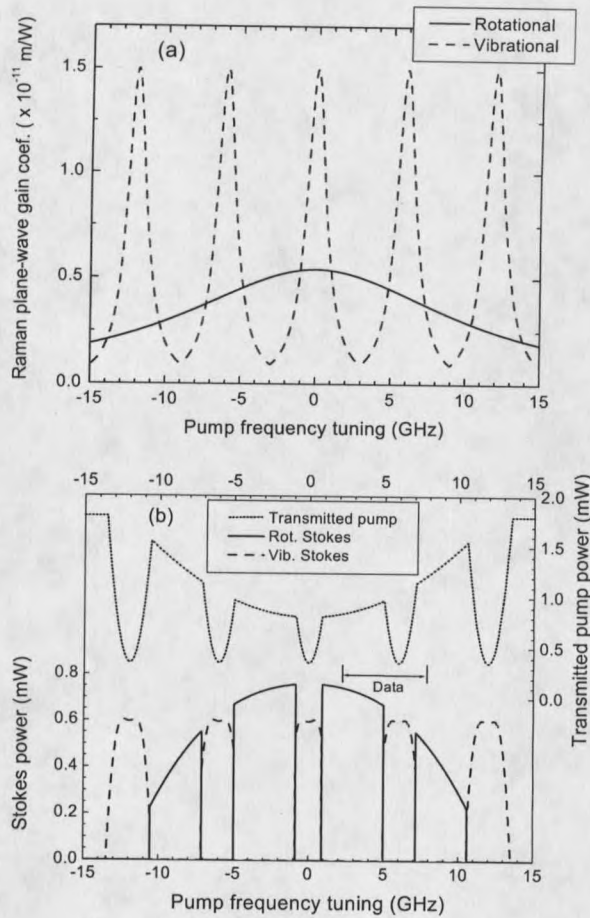


Figure 49 (a) The Raman plane-wave gain coefficients associated with the vibrational and rotational Stokes cavity modes as functions of the pump frequency tuning. The cavity resonances of both Stokes are assumed to be at the gain line-center when the relative pump frequency is zero (i.e., $\Delta_0=0$). (b) Based on these gain profiles, calculation of the power of the transmitted pump, the rotational Stokes, and the vibrational Stokes as functions of pump tuning. Parameters used for the calculation are: mirror reflectances: 0.9999; mirror absorptions: 40 ppm at all wavelengths and both mirrors; input pump power: 5 mW. The range shown is in qualitative agreement with the measure data presented in Fig. 46.

We can qualitatively explain the tuning behavior of this dual-Stokes cw Raman system. Using Eq. 3.19, we first plot in Fig. 49(a) the Raman gain “seen” by the cavity-resonances of the vibrational and rotational Stokes as functions of the pump frequency tuning. Because of the homogeneously broadened Raman gain, the Stokes

mode having the largest net gain (or lowest threshold) will oscillate. Based on this rule we calculate the powers of the transmitted pump, the vibrational Stokes, and the rotational Stokes as functions of the pump frequency tuning using Eqs. (3.4),(3.19),(3.10) and (3.11) and plot them in Fig. 49(b). One can see a qualitative agreement between the measurement (Fig. 46) and the theory, except that only an ~ 6 GHz range of the pump frequency can be tuned in the measurement because of the limited output range of the locking servo for the cavity piezoelectric transducer (PZT) of 0-150 V, which corresponds to a physical tuning range of $\sim 1.2 \mu\text{m}$ of the PZT tube between the cavity mirrors.

Compared to vibrational Stokes, the rotational Stokes has much wider continuous-tuning range. In Fig. 49, while just one rotational cavity resonance is tuned through its gain profile, we have seen five vibrational-Stokes resonances when the pump frequency is tuned by ± 15 GHz. The reason can be seen from Eq. (3.14), for rotational transition $\delta\nu_{rs} = 0.95 \cdot \delta\nu_p$ whereas for vibrational transition $\delta\nu_{vs} = 0.67 \cdot \delta\nu_p$. That is to say, for the same pump frequency tuning range of $\delta\nu_p$, the rotational-Stokes cavity resonance is almost tuned by the same amount of frequency whereas the vibrational-Stokes resonance is tuned by a much smaller amount. In other words, the relative tuning rate between the rotational-Stokes and pump resonances is slower than the case of vibrational-Stokes. Because of this difference in relative tuning-rate, the rotational-Stokes resonance will be "dragged" through the Raman gain profile much slower than the vibrational-Stokes resonance (see Fig. 29). Also, since the rotational Raman gain

linewidth itself is broader than the vibrational gain, the rotational-Stokes cavity resonance can therefore be continuously tuned by a wider range. Using Eq. (3.22), one can calculate that at four times the line-center threshold, the maximum Stokes continuous-tuning range for the 792→830 nm rotational transition is 36.8 GHz, whereas for the 792→1180 nm vibrational transition, it is only 1.77 GHz.

Besides the easier mirror-coating and wider continuous-tuning range, the cw rotational Raman laser has the third advantage compared to the vibrational Raman laser. The thermo-optic effects caused by heat deposition into the Raman gas are less of a problem for the rotational Raman transition because of its smaller photon energy shift, whereas it has been observed that in the high-power vibrational Raman laser thermo-optic effects can lower the conversion efficiency and cause instabilities [20, 10].

Etalon Effect of the Cavity Mirrors

In this section we will show the etalon effect of the cavity mirrors. This effect was first noticed by A. Hagenston, an undergraduate student working in the lab. When she did cavity ringdown experiments to measure the mirror reflectivities, non-random errors as large as 20% variation were obtained in the results. Later, we realized the reason: the front and back surfaces of an HFC mirror form an etalon as illustrated by Fig. 50. In all of the experiments in this thesis, the back surface of the mirror is neither wedged relative to the front surface nor anti-reflective coated. Therefore

the interference between the beams reflected from the two surfaces can modify the effective reflectance as a function of the laser frequency.

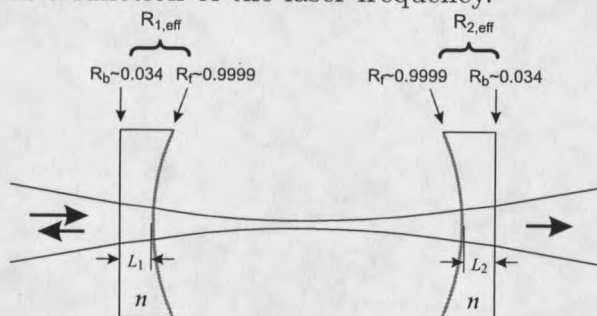


Figure 50 Illustration of the etalon effect of the HFC mirrors. The uncoated back surfaces have reflectances of about 0.034, given by the refractive index of fused silica: 1.4534 (800 nm) [1, page6-25].

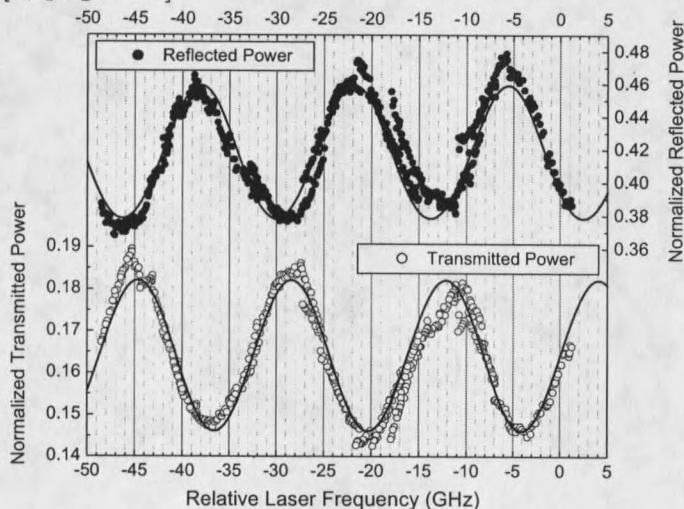


Figure 51 Cavity reflected and transmitted laser power (normalized to the coupled input power) as functions of the incident laser's frequency. The incident laser's power remains at ~ 5.3 mW and the cavity coupling efficiency is estimated to be $\sim 85\%$. The laser frequency is measured relative to 378 600.00 GHz by a Burleigh wavemeter with 10 MHz resolution. Because the two cavity mirrors are actually two etalons, the mirrors' effective reflectance is a function of the laser's frequency and this results in periodic reflected and transmitted laser power from the HFC. The curves are fittings assuming sinusoidal effective reflectances (see Fig. 52) of the HFC mirrors.

To measure this etalon effect, we use the setup of Fig. 45. The pump laser is stabilized to the HFC but there is no H_2 inside the HFC. The incident pump beam is linearly-polarized to eliminate possible birefringence on the HFC mirrors. We measure the reflected and the transmitted pump power from the HFC as the pump laser's frequency is tuned (the incident power stays the same). The data are plotted in Fig. 51. One can see oscillations of the reflected and the transmitted power as functions of the laser's frequency. The phase shift between the two oscillations is almost (but not exactly) π .

We can fit the data in Fig. 51 by choosing the following simple sinusoidal forms of the effective mirror-reflectances in the HFC:

$$R_{1,\text{eff}}(\nu) = R_{1f} \left[1 + 2.3 \times 10^{-6} \sin \left(\frac{2\pi}{16.253} \nu + 1.125\pi \right) \right], \quad (4.8a)$$

$$R_{2,\text{eff}}(\nu) = R_{2f} \left[1 + 2.3 \times 10^{-6} \sin \left(\frac{2\pi}{16.253} \nu + 0.8\pi \right) \right]. \quad (4.8b)$$

where ν is the laser's frequency and R_f is the reflectance of the mirror's front surface (coated side). The number 1 and 2 in the subscripts refer to the HFC's front and back mirrors respectively. To fit the data, we used $R_{1f} = 0.99994$ and $R_{2f} = 0.99995$; we also assumed power absorptions of $A_1 = 40.5 \times 10^{-6}$ and $A_2 = 24.5 \times 10^{-6}$ (independent of the laser's frequency) of the two mirrors. The sinusoidal amplitude in Eq. (4.8), 2.3×10^{-6} , is chosen to fit the data. The oscillation period in Eq. (4.8), 16.253 GHz, is obtained by calculation of the etalon's free-spectral-range: $c/2nL$, where c is the vacuum light speed, $n = 1.4534$ is the mirror's refractive index (fused

silica at 800 nm [1, page6-25]), and $L = 1/4$ inch is the mirror thickness. This oscillation period fits the data very well, confirming that the etalon effect is the cause of the oscillation. The extra phase difference (1.125π versus 0.8π) in the fitting formula is necessary to fit the non- π phase shift between the reflected and transmitted powers in the data. Later we will see that this phase difference is resulted from slightly different thicknesses of the two mirrors.

One can calculate theoretically the effective mirror reflectance based on a Fabry-Perot etalon model:

$$R_{\text{eff}}(\nu) = \left(\sqrt{R_f} - \frac{\sqrt{R_b} T_f \exp(4i\pi\nu n L/c)}{1 - \sqrt{R_b} \sqrt{R_f} \exp(4i\pi\nu n L/c)} \right)^2, \quad (4.9)$$

where R_f and $T_f (= 1 - R_f - A_f)$ are the reflectance and transmittance of the mirror's front surface (coated side) respectively, and R_b is the reflectance of the mirror's back surface (uncoated side). Using the same reflectances and absorptions for fitting, i.e., $R_{1f} = 0.99994$, $R_{2f} = 0.99995$, $A_1 = 40.5 \times 10^{-6}$, and $A_2 = 24.5 \times 10^{-6}$, we plot the theoretical effective mirror reflectances [Eq. (4.9)] and the assumed sinusoidal effective reflectances [Eq. (4.8)] together in Fig. 52.

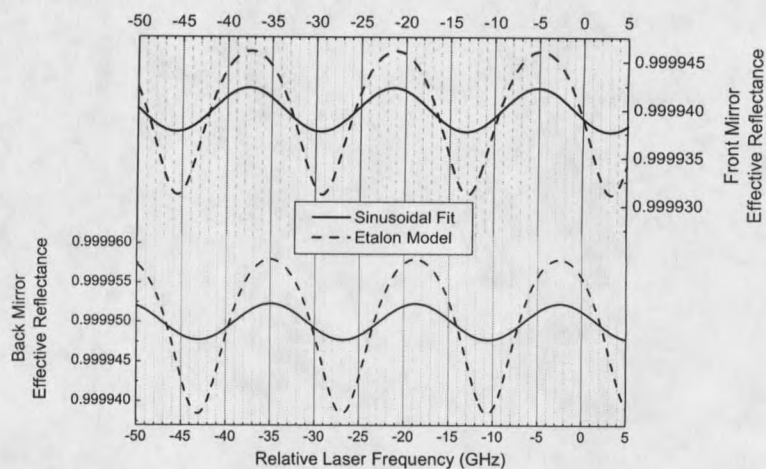


Figure 52 Comparison between the sinusoidal effective-reflectances which fit the data and the calculated effective-reflectances based on the etalon model.

We see that the calculated effective-reflectances based on the etalon model have larger oscillating amplitudes than the simple sinusoidal form used for fitting. This is because our calculation is based on “perfect” fabry-perot planar etalons and a plane-wave laser beam; whereas in reality, the front mirror-surface has a radius of curvature of 50 cm and the laser light is a fundamental Gaussian beam.

As mentioned earlier, to fit the non- π phase shift between the reflected and transmitted laser powers, we had to include an extra phase difference between the sinusoidal effective-reflectances of the two mirrors. The etalon model tells us that this phase difference is caused by a slightly different mirror-thicknesses. The thickness difference between the two mirrors turned out to be an integer number times ~ 40 nm.

CHAPTER 5

MODE-HOP HYSTERESIS IN THE ROTATIONAL RAMAN LASER

This chapter studies the mode-hop hysteresis observed in our cw rotational Stokes laser. After showing the experimental observation, we will give a physical picture showing qualitatively what causes the hysteresis. Based on this picture, we will set up a theoretical model and develop a semi-classical theory. Finally, we will see that the experimental data agrees well with our theory.

Experimental Observation and Qualitative Explanation

Let us consider, in our cw Raman laser, the case when more than one longitudinal Stokes modes are covered under the Raman gain profile and all have a sufficient gain to lase (i.e., gain $>$ loss)¹. The homogeneous gain nature of the Raman process in high-pressure H₂ ensures single-mode operation in favor of the mode having the highest gain. In other words, only the Stokes mode closest to the gain line-center is able to lase.

Then it is natural to think that at what is called by us the "symmetric point" — the two adjacent longitudinal modes of the Stokes lie symmetrically away from the gain line-center, which mode would lase? This condition can be experimentally

¹

Here we mean the small-signal gain or unsaturated gain. Once a Stokes mode lases at steady state, the small-signal gain has to be saturated so that the saturated gain = cavity loss.

achieved in a cw rotational Raman laser, because the linewidth of the rotational Raman gain (1 GHz FWHM) is wide enough to cover two adjacent longitudinal Stokes modes (mode-spacing 2 GHz). We find that the mode-hop between the two Stokes modes shows a hysteresis when we tune the pump frequency back and forth around the symmetric point, as shown in Fig. 53. The amount of hysteresis, denoted by H as shown in Fig. 53, is found to be larger at higher pumping rate. We also measure the transmitted pump and rotational Stokes powers as the pump frequency is tuned around the symmetric point. The data are given in Fig. 54. We see that the mode-hops are also accompanied by power discontinuities.

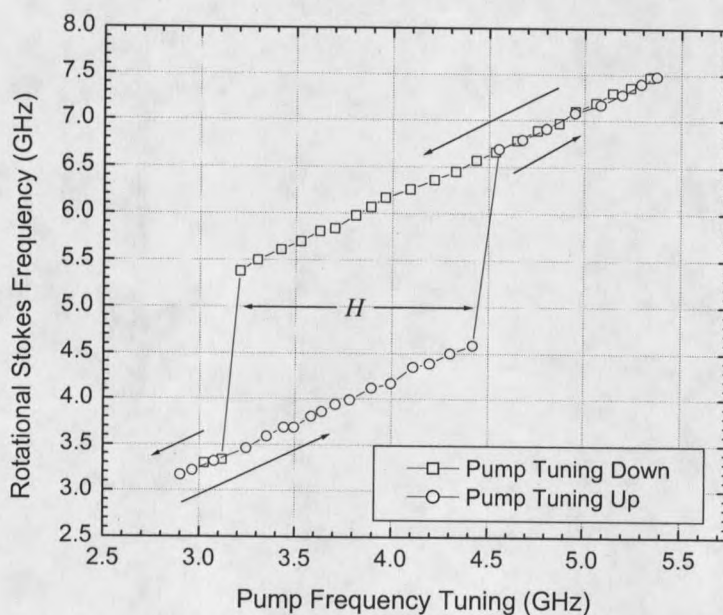


Figure 53 Experimental data showing the mode-hop hysteresis between the two adjacent rotational Stokes modes. Optical frequencies are measured by a Burleigh wavemeter with 10 MHz resolution. The pump frequency is measured relative to 378 350 GHz and the Stokes frequency is measured relative to 360 750 GHz.

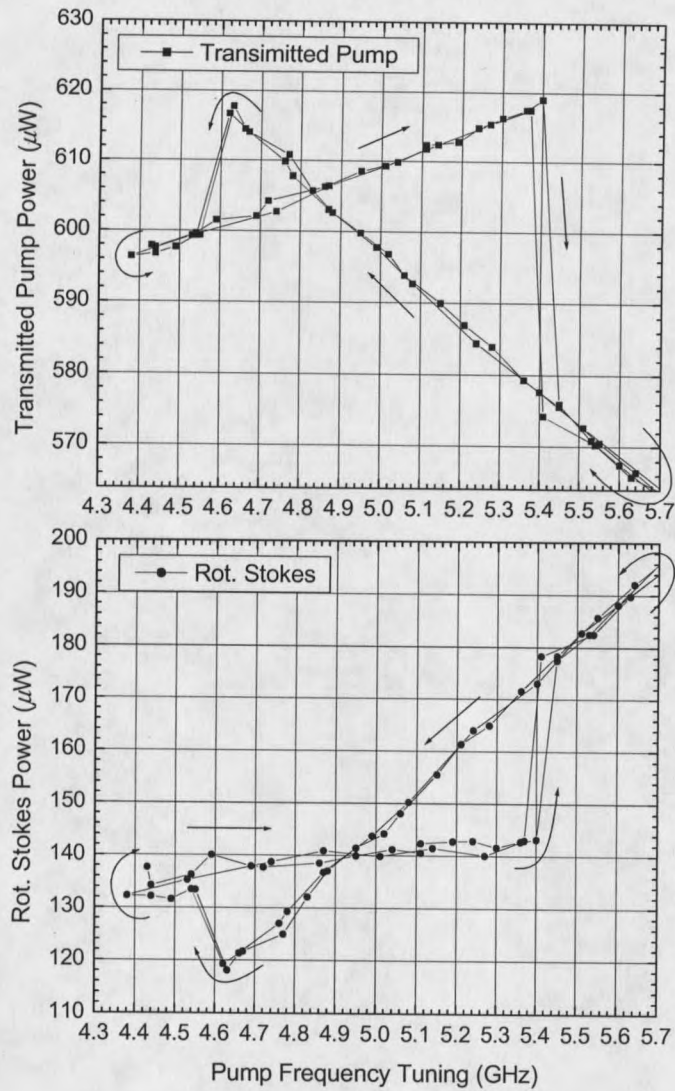


Figure 54 Transmitted pump power (top) and rotational Stokes power (bottom) as functions of pump frequency tuning show butterfly-like patterns. Power discontinuities indicate mode-hops. The input pump beam is circularly polarized and the rotational Stokes is counter-circularly polarized for both modes [11]. The pump frequency tuning is shown relative to 378 384 GHz. Back and forth tuning of the pump frequency is performed twice.

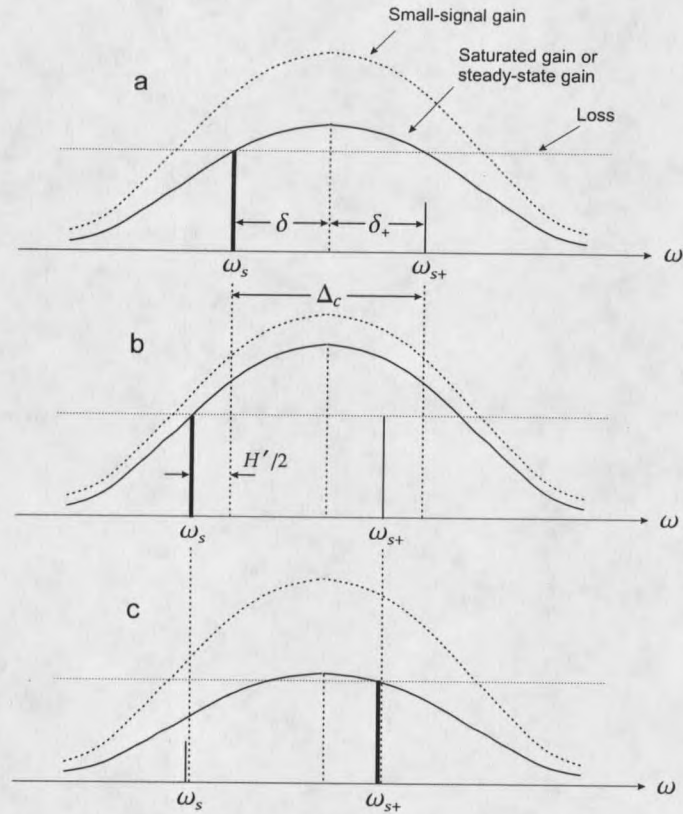


Figure 55 Picture showing how the mode-hop hysteresis happens. $\delta (< 0)$ and $\delta_+ (> 0)$ are the two-photon-detunings of the rotational Stokes modes ω_s and ω_{s+} respectively. $\Delta_c = \delta_+ - \delta$ is the longitudinal mode spacing of the two Stokes modes. The width of the rotational Raman gain linewidth is sufficient to cover the two adjacent longitudinal Stokes modes. a, The “symmetric point”, where the two Stokes modes lie symmetrically away from the line-center, $|\delta| = |\delta_+|$. The sub-threshold mode ω_{s+} loses some gain so it is below threshold. b, The mode-hop point, where $|\delta| > |\delta_+|$ and the mode ω_{s+} reaches the threshold since it is closer to the line-center and the lost gain is compensated. c, After the mode-hop, the steady-state gain is quickly saturated to a lower level so that the mode ω_{s+} sees equal gain and loss.

In order for the hysteresis to happen, the steady-state gain (saturated by the lasing mode) experienced by the sub-threshold Stokes mode must be somehow suppressed or “stolen”, so that at the symmetric point it is still below threshold, see Fig. 55a.

The mode-hop can happen only when we tune beyond the symmetric point to compensate the lost gain by making the sub-threshold mode closer to the line-center, see Fig. 55b. After the mode-hop, the original lasing mode becomes the sub-threshold mode and now its gain is suppressed, see Fig. 55c. If we tune the laser backwards, the same $a \rightarrow b \rightarrow c$ process happens at the other side of the gain profile and hence we see the hysteresis effect. We also notice the discontinuous change of the steady-state gain before and after the mode-hop (Fig. 55b and c) and this explains the power discontinuities at the mode-hop points measured in Fig. 54.

To the author's knowledge, the nearly same mode-hop hysteresis in single-mode lasers was observed before by Harris and Loudon *et al.* [55] in an argon-ion laser. They measured a discontinuity of the laser's power and thus indirectly saw the longitudinal mode-hop hysteresis. They successfully explained the hysteresis and the behind gain suppression by a model based on a four-wave mixing (FWM) process. In their model, coupled by the so-called "population pulsation", the lasing mode and its two adjacent modes form four-wave mixing, which results in a redistribution of energy in the two sub-threshold modes, keeping them all below threshold.

We will try to implant their model to our cw Raman laser to explain the hysteresis. But our Raman laser is different from the argon-ion laser that Harris and Loudon studied: ours is a two-field far-off-resonance Raman process whereas theirs is a one-field and two-level (near-resonance) problem. It turns out that (1) instead of one FWM process, we need to consider at least two FWM's and (2) instead of coupled

by the population pulsation, in our system the multiple waves are coupled by the molecular coherences (Raman-resonant or Raman-assisted FWM's). The details of our model are shown in Fig. 56.

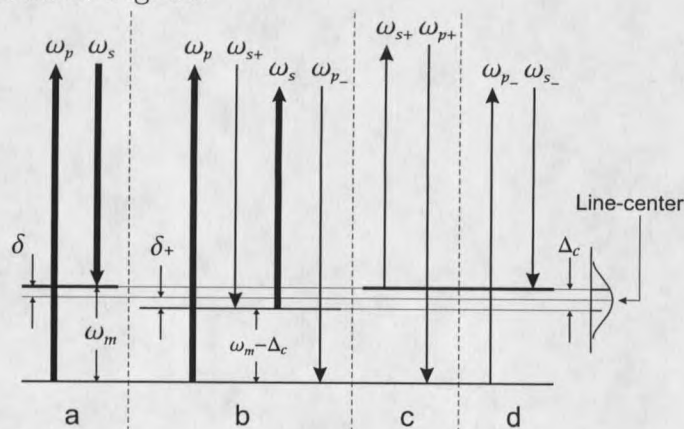


Figure 56 Theoretical model for mop-hop hysteresis. a, The usual Raman process: the pump field at frequency ω_p and the lasing-Stokes mode at frequency ω_s establish a strong coherence between the two energy states oscillating at frequency $\omega_m = \omega_p - \omega_s$. b, The first FWM process: the sub-threshold Stokes $\omega_{s+} = \omega_s + \Delta_c$ beats with the strong pump ω_p , producing a weak coherence sideband oscillating at $\omega_p - \omega_{s+} = \omega_m - \Delta_c$; then the lasing-Stokes mode is scattered off this coherence sideband to produce a weak pump sideband with frequency $\omega_{p-} = \omega_p - \Delta_c$. c, The second FWM process (a and c together): the sub-threshold Stokes ω_{s+} is scattered off the strong coherence, producing another new weak field ω_{p+} . d, A "bonus" new weak field is generated, although it does not contribute to the gain suppression on ω_{s-} : the sideband ω_{p-} is scattered off the strong coherence, producing a new field ω_{s+} . In this plot, we use the thick lines to represent "strong" and the thin lines mean "weak".

First, Fig. 56a shows the general far-off-resonance Raman process: there are the pump field ω_p , the Stokes field ω_s , and the coherence ρ_{ab} oscillating at the difference frequency $\omega_p - \omega_s = \omega_m$. Then, in Fig. 56b, the sub-threshold Stokes mode ω_{s+} , the strong pump ω_p and the strong lasing Stokes mode ω_s produce by FWM a new weak frequency component at ω_{p-} . These four fields are coupled by a weak coherence

sideband oscillating at the difference frequency $\omega_p - \omega_{s+} = \omega_{p-} - \omega_s = \omega_m - \Delta_c$, where Δ_c is the longitudinal mode spacing of the two adjacent Stokes cavity modes (i.e., the cavity's free-spectral-range $\times 2\pi$). One can see that this Raman-assisted FWM is very similar to the Stokes-anti-Stokes Raman process. Knowing that the Stokes-anti-Stokes coupling can suppress the exponential gain in stimulated Raman scattering [56], we conclude that the gain of the field ω_{s+} in Fig. 56b can also be suppressed in a Raman-assisted FWM.

We have found one source of the gain suppression, but that does not complete the picture. Since a strong coherence has been built by the strong fields ω_p and ω_s (Fig. 56a), Fig. 56c shows that the field ω_{s+} can be scattered off this strong coherence and a new field ω_{p+} is generated. We can view Fig. 56c as a pure Raman anti-Stokes scattering; or Fig. 56a and Fig. 56c together can be viewed as another Raman-assisted FWM process. Again the gain of the field ω_{s+} is suppressed because energy is transferred from the field ω_{s+} to the field ω_{p+} .

To complete the entire picture, we note that field ω_{p-} can also be scattered off the strong coherence, producing another weak field oscillating at ω_{s-} , as shown in Fig. 56d. This process does not directly contribute to the gain suppression of the sub-threshold Stokes mode ω_{s+} , but it should be included in the theory in the next section.

From the above analysis, Raman-assisted multi-wave mixings coupled with the molecular coherences lead to two sidebands on both pump and Stokes fields. In other

words, we have totally six fields; two of them are strong (ω_p and ω_s) and four of them are weak ($\omega_{p\pm}$ and $\omega_{s\pm}$). Next we will develop a semi-classical theory based on our model. The two strong fields ω_p and ω_s will be assumed not affected by the other weak sidebands and the steady-state solution of the cw Stokes laser will be directly used for the two strong fields.

Theory

As discussed above, both pump and Stokes fields have a pair of weak sidebands oscillating at $\omega_{p(s)} \pm \Delta_c$:

$$\begin{aligned} \tilde{E}_p(\mathbf{r}, t) = \frac{1}{2} \left[E_{p0}(\mathbf{r}, t)e^{-i\omega_p t} + E_{p+}(\mathbf{r}, t)e^{-i(\omega_p + \Delta_c)t} \right. \\ \left. + E_{p-}(\mathbf{r}, t)e^{-i(\omega_p - \Delta_c)t} + \text{c.c.} \right], \end{aligned} \quad (5.1a)$$

$$\begin{aligned} \tilde{E}_s(\mathbf{r}, t) = \frac{1}{2} \left[E_{s0}(\mathbf{r}, t)e^{-i\omega_s t} + E_{s+}(\mathbf{r}, t)e^{-i(\omega_s + \Delta_c)t} \right. \\ \left. + E_{s-}(\mathbf{r}, t)e^{-i(\omega_s - \Delta_c)t} + \text{c.c.} \right], \end{aligned} \quad (5.1b)$$

(Note that the field amplitude can be split into time-dependent amplitude and spatial-dependent cavity mode:

$$E_q(\mathbf{r}, t) = E_q(t)u_q(\mathbf{r}), \quad (5.2)$$

where $q = p0, s0, p\pm$, and $s\pm$). The coherence also has a weak sideband:

$$\begin{aligned} \tilde{\rho}_{ab}(\mathbf{r}, t) &= \tilde{\rho}_0(\mathbf{r}, t) + \tilde{\rho}_-(\mathbf{r}, t) \\ &= \rho_0(\mathbf{r}, t)e^{i\omega_m t} + \rho_-(\mathbf{r}, t)e^{i(\omega_m - \Delta_c)t}. \end{aligned} \quad (5.3)$$

The "dc" amplitudes E_{p0} , E_{s0} , and ρ_0 have been thoroughly solved for the Stokes laser in a previous chapter (page 18). So here we can follow the previous treatment by replacing the *amplitudes* of the fields and coherence in the following forms:

$$E_p(\mathbf{r}, t) = E_{p0}(\mathbf{r}, t) + E_{p+}(\mathbf{r}, t)e^{-i\Delta ct} + E_{p-}(\mathbf{r}, t)e^{i\Delta ct}, \quad (5.4a)$$

$$E_s(\mathbf{r}, t) = E_{s0}(\mathbf{r}, t) + E_{s+}(\mathbf{r}, t)e^{-i\Delta ct} + E_{s-}(\mathbf{r}, t)e^{i\Delta ct}, \quad (5.4b)$$

$$\rho_{ab}(\mathbf{r}, t) = \rho_0(\mathbf{r}, t) + \rho_-(\mathbf{r}, t)e^{-i\Delta ct}, \quad (5.4c)$$

where $|E_{p\pm}| \ll |E_p|$, $|E_{s\pm}| \ll |E_s|$, and $|\rho_-| \ll |\rho|$. Because of this condition, we will assume in the later analysis that the strong field E_{p0} and E_{s0} as well as the strong coherence ρ_0 are not affected by the presence of the much weaker sidebands $E_{p\pm}$, $E_{s\pm}$, and ρ_- .

Similar to the strong pump and Stokes fields, these weak sidebands should also satisfy the intracavity field equation:

$$\begin{aligned} \dot{E}_{s+}(t) + \left[\frac{\gamma_{cs+}}{2} - i(\omega_{s+} - \omega_{cs+}) \right] E_{s+}(t) = \\ i \frac{\omega_{s+}}{2\epsilon_0} \frac{1}{V_{s+}} \iiint_{\text{cavity}} dx dy dz P_{s+}(\mathbf{r}, t) u_{s+}^*(\mathbf{r}), \end{aligned} \quad (5.5a)$$

$$\begin{aligned} \dot{E}_{p-}(t) + \left[\frac{\gamma_{cp-}}{2} - i(\omega_{p-} - \omega_{cp-}) \right] E_{p-}(t) = \\ i \frac{\omega_{p-}}{2\epsilon_0} \frac{1}{V_{p-}} \iiint_{\text{cavity}} dx dy dz P_{p-}(\mathbf{r}, t) u_{p-}^*(\mathbf{r}), \end{aligned} \quad (5.5b)$$

$$\begin{aligned} \dot{E}_{p+}(t) + \left[\frac{\gamma_{cp+}}{2} - i(\omega_{p+} - \omega_{cp+}) \right] E_{p+}(t) = \\ i \frac{\omega_{p+}}{2\epsilon_0} \frac{1}{V_{p+}} \iiint_{\text{cavity}} dx dy dz P_{p+}(\mathbf{r}, t) u_{p+}^*(\mathbf{r}), \end{aligned} \quad (5.5c)$$

$$\dot{E}_{s-}(t) + \left[\frac{\gamma_{cs-}}{2} - i(\omega_{s-} - \omega_{cs-}) \right] E_{s-}(t) = i \frac{\omega_{s-}}{2\epsilon_0} \frac{1}{V_{s-}} \iiint_{\text{cavity}} dx dy dz P_{s-}(\mathbf{r}, t) u_{s-}^*(\mathbf{r}), \quad (5.5d)$$

where $\gamma_{cs\pm}$ and $\gamma_{cp\pm}$ are the cavity energy decay rate of the fields $\omega_{s\pm}$ and $\omega_{p\pm}$ respectively; $\omega_{cs\pm}$ and $\omega_{cp\pm}$ are the cavity resonance frequencies for the four fields; $V_{s\pm}$ and $V_{p\pm}$ are the cavity mode-volume of the four fields acting as the normalization factor [see Eq. (2.63a)]. In Eqs. (5.5), P 's are the amplitudes of the polarization associated with each fields. According to Eqs. (2.47); and using the replacements Eqs. (5.4), we get

$$\begin{aligned} P_p &= 2N\hbar a_p (E_{p0} + E_{p+} e^{-i\Delta_c t} + E_{p-} e^{i\Delta_c t}) \\ &\quad + 2N\hbar d_s (\rho_0^* + \rho_-^* e^{i\Delta_c t}) (E_{s0} + E_{s+} e^{-i\Delta_c t} + E_{s-} e^{i\Delta_c t}) \\ &= P_{p0} + P_{p+} e^{-i\Delta_c t} + P_{p-} e^{i\Delta_c t}, \end{aligned} \quad (5.6)$$

where

$$P_{p0}(\mathbf{r}, t) = 2N\hbar [a_p E_{p0}(\mathbf{r}, t) + d_s \rho_0^*(\mathbf{r}, t) E_{s0}(\mathbf{r}, t)], \quad (5.7a)$$

$$P_{p+}(\mathbf{r}, t) = 2N\hbar [a_p E_{p+}(\mathbf{r}, t) + d_s \rho_0^*(\mathbf{r}, t) E_{s+}(\mathbf{r}, t)], \quad (5.7b)$$

$$\begin{aligned} P_{p-}(\mathbf{r}, t) &= 2N\hbar [a_p E_{p-}(\mathbf{r}, t) + d_s \rho_0^*(\mathbf{r}, t) E_{s-}(\mathbf{r}, t) \\ &\quad + d_s \rho_-^*(\mathbf{r}, t) E_{s0}(\mathbf{r}, t)]. \end{aligned} \quad (5.7c)$$

Here P_{p0} is the "dc" polarization which is associated with the strong pump field E_{p0} ; whereas $P_{p\pm}$ are the polarizations that generate the two pump sidebands $E_{p\pm}$. We have ignored the second-order small term $\rho_-^* E_{s+}$ and the second harmonic term

$\rho_-^* E_{s-} e^{2i\Delta ct}$ in Eq. (5.6).

Similarly, for the Stokes,

$$\begin{aligned}
 P_s &= 2N\hbar a_s (E_{s0} + E_{s+} e^{-i\Delta ct} + E_{s-} e^{i\Delta ct}) \\
 &\quad + 2N\hbar d_s (\rho_0 + \rho_- e^{-i\Delta ct}) (E_{p0} + E_{p+} e^{-i\Delta ct} + E_{p-} e^{i\Delta ct}) \\
 &= P_{s0} + P_{s+} e^{-i\Delta ct} + P_{s-} e^{i\Delta ct},
 \end{aligned} \tag{5.8}$$

where

$$P_{s0}(\mathbf{r}, t) = 2N\hbar [a_s E_{s0}(\mathbf{r}, t) + d_s \rho_0(\mathbf{r}, t) E_{s0}(\mathbf{r}, t)], \tag{5.9a}$$

$$\begin{aligned}
 P_{s+}(\mathbf{r}, t) &= 2N\hbar [a_s E_{s+}(\mathbf{r}, t) + d_s \rho_0(\mathbf{r}, t) E_{p+}(\mathbf{r}, t) \\
 &\quad + d_s \rho_-(\mathbf{r}, t) E_{p0}(\mathbf{r}, t)],
 \end{aligned} \tag{5.9b}$$

$$P_{s-}(\mathbf{r}, t) = 2N\hbar [a_s E_{s-}(\mathbf{r}, t) + d_s \rho_0(\mathbf{r}, t) E_{p-}(\mathbf{r}, t)]. \tag{5.9c}$$

Next, the total coherence amplitude ρ_{ab} satisfies the equation of motion given by Eq. (2.40b) (ignoring the relative Stark shift):

$$\dot{\rho}_{ab} = -(\gamma_{ab} - i\delta)\rho_{ab} + i\Omega_{ab}D, \tag{5.10}$$

where $\Omega_{ab} = (d_s/2)E_s E_p^*$ is the two-photon Rabi frequency. Substituting in Eqs. (5.4) and grouping the dc terms and the amplitudes of the terms with $e^{\pm i\Delta ct}$, Eq. (5.10)

becomes three equations:

$$\dot{\rho}_0(\mathbf{r}, t) = -(\gamma_{ab} - i\delta)\rho_0(\mathbf{r}, t) + i\frac{d_s}{2}DE_{s0}(\mathbf{r}, t)E_{p0}^*(\mathbf{r}, t), \quad (5.11a)$$

$$\begin{aligned} \dot{\rho}_-(\mathbf{r}, t) = & -(\gamma_{ab} - i\delta_+)\rho_-(\mathbf{r}, t) \\ & + i\frac{d_s}{2}D[E_{s+}(\mathbf{r}, t)E_{p0}^*(\mathbf{r}, t) + E_{s0}(\mathbf{r}, t)E_{p-}^*(\mathbf{r}, t)], \end{aligned} \quad (5.11b)$$

$$\begin{aligned} \dot{\rho}_+(\mathbf{r}, t) = & -(\gamma_{ab} - i\delta_-)\rho_+(\mathbf{r}, t) \\ & + i\frac{d_s}{2}D[E_{s-}(\mathbf{r}, t)E_{p0}^*(\mathbf{r}, t) + E_{s0}(\mathbf{r}, t)E_{p+}^*(\mathbf{r}, t)], \end{aligned} \quad (5.11c)$$

where $\delta_{\pm} = \delta \pm \Delta_c$. Here appears a new coherence sideband ρ_+ , which we have been ignoring in our previous discussion. We will continue to ignore it because it has one more free-spectral-range of detuning compared to the other two coherences ($\sim -1.5\Delta_c$ vs. $\sim \pm 0.5\Delta_c$). Hence any Raman-assisted FWM processes associated with ρ_+ are weak and ignored by us.

The steady-state solutions of Eqs. (5.11a) and (5.11b) are

$$\rho_0(\mathbf{r}, t) = i\frac{d_s}{2}D \frac{E_{s0}(\mathbf{r}, t)E_{p0}^*(\mathbf{r}, t)}{\gamma_{ab} - i\delta}. \quad (5.12a)$$

$$\rho_-(\mathbf{r}, t) = i\frac{d_s}{2}D \frac{E_{s+}(\mathbf{r}, t)E_{p0}^*(\mathbf{r}, t) + E_{s0}(\mathbf{r}, t)E_{p-}^*(\mathbf{r}, t)}{\gamma_{ab} - i\delta_+}. \quad (5.12b)$$

Substituting the above steady-state coherences into Eqs. (5.7b), (5.7c), (5.9b), and (5.9c), we obtain the polarization amplitudes of each field. We then plug them into the

field equations (5.5). Knowing the results of the following integrals [see Eqs. (2.91)-(2.94)]:

$$\frac{1}{V_q} \int_0^{2\pi} d\phi \int_{-L/2}^{L/2} dz \int_0^\infty r dr |u_r|^2 |u_q|^2 = \frac{1}{2} \frac{k_q}{k_r + k_q}, \quad (5.13a)$$

$$\frac{1}{V_q} \int_0^{2\pi} d\phi \int_{-L/2}^{L/2} dz \int_0^\infty r dr u_m u_n u_r^* u_q^* = \frac{1}{2} \frac{k_q}{\sum k} \text{sinc}(\Delta k L/2), \quad (5.13b)$$

where $\sum k = k_m + k_n + k_r + k_q$ and $\Delta k = k_m + k_n - k_r - k_q$, then the field equations become

$$\begin{aligned} \dot{E}_{s+}(t) + \left[\frac{\gamma_{cs+}}{2} - i(n_{s+} \omega_{s+} - \omega_{cs+}) \right] E_{s+}(t) = \\ - \frac{1}{4} \frac{\omega_{s+}}{\epsilon_0} \frac{N \hbar d_s^2 D}{\epsilon_0} \left[\frac{1}{\gamma_{ab} - i\delta_+} \frac{k_{s+}}{k_p + k_{s+}} |E_{p0}(t)|^2 E_{s+}(t) \right. \\ + \frac{1}{\gamma_{ab} - i\delta_+} \frac{k_{s+}}{\sum k_1} \text{sinc}\left(\frac{\Delta k_1 L}{2}\right) E_{p0}(t) E_{s0}(t) E_{p-}^*(t) \\ \left. + \frac{1}{\gamma_{ab} - i\delta_+} \frac{k_{s+}}{\sum k_2} \text{sinc}\left(\frac{\Delta k_2 L}{2}\right) E_{p+}(t) E_{s0}(t) E_{p0}^*(t) \right], \quad (5.14a) \end{aligned}$$

$$\begin{aligned} \dot{E}_{p-}(t) + \left[\frac{\gamma_{cp-}}{2} - i(n_{p-} \omega_{p-} - \omega_{cp-}) \right] E_{p-}(t) = \\ \frac{1}{4} \frac{\omega_{p-}}{\epsilon_0} \frac{N \hbar d_s^2 D}{\epsilon_0} \left[\frac{1}{\gamma_{ab} + i\delta_+} \frac{k_{p-}}{k_s + k_{p-}} |E_{s0}(t)|^2 E_{p-}(t) \right. \\ + \frac{1}{\gamma_{ab} + i\delta_+} \frac{k_{p-}}{\sum k_1} \text{sinc}\left(\frac{\Delta k_1 L}{2}\right) E_{p0}(t) E_{s0}(t) E_{s+}^*(t) \\ \left. + \frac{1}{\gamma_{ab} + i\delta_+} \frac{k_{p-}}{\sum k_3} \text{sinc}\left(\frac{\Delta k_3 L}{2}\right) E_{p0}(t) E_{s-}(t) E_{s0}^*(t) \right], \quad (5.14b) \end{aligned}$$

$$\begin{aligned} \dot{E}_{p+}(t) + \left[\frac{\gamma_{cp+}}{2} - i(n_{p+} \omega_{p+} - \omega_{cp+}) \right] E_{p+}(t) = \\ \frac{1}{4} \frac{\omega_{p+}}{\epsilon_0} \frac{N \hbar d_s^2 D}{\epsilon_0} \frac{1}{\gamma_{ab} + i\delta_+} \frac{k_{p+}}{\sum k_2} \text{sinc}\left(\frac{-\Delta k_2 L}{2}\right) E_{p0}(t) E_{s+}(t) E_{s0}^*(t), \quad (5.14c) \end{aligned}$$

$$\begin{aligned} \dot{E}_{s-}(t) + \left[\frac{\gamma_{cs-}}{2} - i(n_{s-}\omega_{s-} - \omega_{cs-}) \right] E_{s-}(t) = \\ -\frac{1}{4}\omega_{s-} \frac{N\hbar d_s^2 D}{\epsilon_0} \frac{1}{\gamma_{ab} - i\delta} \frac{k_{s-}}{\sum k_3} \text{sinc}\left(\frac{-\Delta k_3 L}{2}\right) E_{p-}(t) E_{s0}(t) E_{p0}^*(t), \end{aligned} \quad (5.14d)$$

where $n_q = 1 + N\hbar a_q/\epsilon_0$ is the refractive index at frequency ω_q , and

$$\sum k_1 = k_p + k_s + k_{p-} + k_{s+},$$

$$\Delta k_1 = k_p + k_s - k_{p-} - k_{s+},$$

$$\sum k_2 = k_{p+} + k_s + k_p + k_{s+},$$

$$\Delta k_2 = k_{p+} + k_s - k_p - k_{s+},$$

$$\sum k_3 = k_{p-} + k_s + k_p + k_{s-},$$

$$\Delta k_3 = k_{p-} + k_s - k_p - k_{s-}.$$

Since the cavity mode spacing $\Delta \ll \omega_s$ or ω_p , it is reasonable to take $\omega_{s\pm} \approx \omega_s$ and $\omega_{p\pm} \approx \omega_p$, and thus $k_{s\pm} \approx k_s$ and $k_{p\pm} \approx k_p$. Therefore, $\sum k_i \approx 2(k_p + k_s)$, and $\Delta k_i \approx 0$ or $\text{sinc}(\Delta k_i L/2) \approx 1$.

Next, we assume that all the field amplitudes are real for simplicity and use the gain term that has been previously defined by Eq. (2.65):

$$G(\delta) = -\frac{1}{4}\omega_s \frac{N\hbar d_0^2 D}{\epsilon} \frac{\gamma_{ab}}{\gamma_{ab}^2 + \delta^2} \frac{\lambda_p}{\lambda_p + \lambda_s}. \quad (5.15)$$

Then, by keeping only the real parts in Eqs. (5.14), we obtain

$$\begin{aligned} \dot{E}_{s+} + \frac{\gamma_{cs+}}{2} E_{s+} = G(\delta_+) E_{p0}^2 E_{s+} \\ + \frac{1}{2} G(\delta_+) E_{p0} E_{s0} E_{p-} + \frac{1}{2} G(\delta) E_{p+} E_{s0} E_{p0}, \end{aligned} \quad (5.16a)$$

$$\dot{E}_{p-} + \frac{\gamma_{cp-}}{2} E_{p-} = -\frac{\omega_p^2}{\omega_s^2} \left[G(\delta_+) E_{s0}^2 E_{p-} + \frac{1}{2} G(\delta_+) E_{p0} E_{s0} E_{s+} + \frac{1}{2} G(\delta) E_{p0} E_{s-} E_{s0} \right], \quad (5.16b)$$

$$\dot{E}_{p+} + \frac{\gamma_{cp+}}{2} E_{p+} = -\frac{\omega_p^2}{\omega_s^2} \frac{1}{2} G(\delta) E_{p0} E_{s+} E_{s0}, \quad (5.16c)$$

$$\dot{E}_{s-} + \frac{\gamma_{cs-}}{2} E_{s-} = \frac{1}{2} G(\delta) E_{p-} E_{s0} E_{p0}. \quad (5.16d)$$

Eqs. (5.16) can be expressed in alternative forms as

$$\left(\frac{d}{dt} + \alpha_{s+} \right) E_{s+} = \kappa_{s+} E_{p-} + \kappa_{s-} E_{p+}, \quad (5.17a)$$

$$\left(\frac{d}{dt} + \alpha_{p-} \right) E_{p-} = \kappa_{p-} E_{s+} + \kappa_{p+} E_{s-}, \quad (5.17b)$$

$$\left(\frac{d}{dt} + \frac{\gamma_{cp+}}{2} \right) E_{p+} = \kappa_{p+} E_{s+}, \quad (5.17c)$$

$$\left(\frac{d}{dt} + \frac{\gamma_{cs-}}{2} \right) E_{s-} = \kappa_{s-} E_{p-}, \quad (5.17d)$$

where

$$\alpha_{s+} = \frac{\gamma_{cs+}}{2} - G(\delta_+) E_{p0}^2, \quad \alpha_{p-} = \frac{\gamma_{cp-}}{2} + \frac{\omega_p^2}{\omega_s^2} G(\delta_+) E_{s0}^2, \quad (5.18a)$$

$$\kappa_{s+} = \frac{1}{2} G(\delta_+) E_{p0} E_{s0}, \quad \kappa_{p-} = -\frac{1}{2} \frac{\omega_p^2}{\omega_s^2} G(\delta_+) E_{p0} E_{s0}, \quad (5.18b)$$

$$\kappa_{p+} = -\frac{1}{2} \frac{\omega_p^2}{\omega_s^2} G(\delta) E_{p0} E_{s0}, \quad \kappa_{s-} = \frac{1}{2} G(\delta) E_{p0} E_{s0}. \quad (5.18c)$$

Multiplying both sides of Eq. (5.17a) by $(d/dt + \gamma_{cp+}/2)$ and substituting in Eq. (5.17c),

we can eliminate E_{p+} and obtain

$$\left(\frac{d}{dt} + \alpha_{s+} \right) \left(\frac{d}{dt} + \frac{\gamma_{cp+}}{2} \right) E_{s+} = \left(\frac{d}{dt} + \frac{\gamma_{cp+}}{2} \right) \kappa_{s+} E_{p-} + \kappa_{p+} \kappa_{s-} E_{s+}, \quad (5.19)$$

We can do the same step to eliminate E_{s-} using Eqs. (5.17b) and (5.17d) and obtain

$$\left(\frac{d}{dt} + \alpha_{p-} \right) \left(\frac{d}{dt} + \frac{\gamma_{cs-}}{2} \right) E_{p-} = \left(\frac{d}{dt} + \frac{\gamma_{cs-}}{2} \right) \kappa_{p-} E_{s+} + \kappa_{p+} \kappa_{s-} E_{p-}, \quad (5.20)$$

or

$$\left[\frac{d^2}{dt^2} + \left(\alpha_{s+} + \frac{\gamma_{cp+}}{2} \right) \frac{d}{dt} + \alpha_{s+} \frac{\gamma_{cp+}}{2} - \kappa_{p+} \kappa_{s-} \right] E_{s+} = \left(\frac{d}{dt} + \frac{\gamma_{cp+}}{2} \right) \kappa_{s+} E_{p-}, \quad (5.21a)$$

$$\left[\frac{d^2}{dt^2} + \left(\alpha_{p-} + \frac{\gamma_{cs-}}{2} \right) \frac{d}{dt} + \alpha_{p-} \frac{\gamma_{cs-}}{2} - \kappa_{p+} \kappa_{s-} \right] E_{p-} = \left(\frac{d}{dt} + \frac{\gamma_{cs-}}{2} \right) \kappa_{p-} E_{s+}. \quad (5.21b)$$

We can eliminate E_{p-} to get

$$\begin{aligned} & \left[\frac{d^2}{dt^2} + \left(\alpha_{s+} + \frac{\gamma_{cp+}}{2} \right) \frac{d}{dt} + \alpha_{s+} \frac{\gamma_{cp+}}{2} - \kappa_{p+} \kappa_{s-} \right] \times \\ & \left[\frac{d^2}{dt^2} + \left(\alpha_{p-} + \frac{\gamma_{cs-}}{2} \right) \frac{d}{dt} + \alpha_{p-} \frac{\gamma_{cs-}}{2} - \kappa_{p+} \kappa_{s-} \right] E_{s+} = \\ & \left(\frac{d}{dt} + \frac{\gamma_{cp+}}{2} \right) \left(\frac{d}{dt} + \frac{\gamma_{cs-}}{2} \right) \kappa_{s+} \kappa_{p-} E_{s+}. \end{aligned} \quad (5.22)$$

Assuming a trial solution

$$E_{s+} = E_{s+}(0) e^{gt}, \quad (5.23)$$

where g represents an exponential gain coefficient for the field amplitude E_{s+} . If $g < 0$, E_{s+} is below threshold but once g starts to be larger than zero, E_{s+} will experience exponential growth and will overcome the loss to lase. Therefore it is natural to consider that $g = 0$ is the mode-hop condition. We solve for g by substituting the above trial solution into Eq.(5.22) and obtaining

$$\begin{aligned} & \left[g^2 + \left(\alpha_{s+} + \frac{\gamma_{cp+}}{2} \right) g + \alpha_{s+} \frac{\gamma_{cp+}}{2} - \kappa_{p+} \kappa_{s-} \right] \times \\ & \left[g^2 + \left(\alpha_{p-} + \frac{\gamma_{cs-}}{2} \right) g + \alpha_{p-} \frac{\gamma_{cs-}}{2} - \kappa_{p+} \kappa_{s-} \right] = \\ & \left(g + \frac{\gamma_{cp+}}{2} \right) \left(g + \frac{\gamma_{cs-}}{2} \right) \kappa_{s+} \kappa_{p-}. \end{aligned} \quad (5.24)$$

This is an ugly equation to 4th degree in g and analytical solution to g seems to be hopeless. However, since $g = 0$ is the mode-hop condition, letting $g = 0$ in Eq. (5.24) we obtain

$$\left(\alpha_{s+} \frac{\gamma_{cp+}}{2} - \kappa_{p+} \kappa_{s-}\right) \left(\alpha_{p-} \frac{\gamma_{cs-}}{2} - \kappa_{p+} \kappa_{s-}\right) - \frac{\gamma_{cp+} \gamma_{cs-}}{4} \kappa_{s+} \kappa_{p-} = f(\delta, R') = 0. \quad (5.25)$$

Because α 's and κ 's are functions of the two-photon-detuning δ and the intracavity field amplitudes $E_{p(s)0}$, we define Eq. (5.25) as a function $f(\delta, R')$, where the pumping rate $R' = P_{ep}/P_{th}(\delta = \pm\Delta_c/2)$ is the input pump power normalized to the symmetric point threshold (i.e., the threshold when $\delta = \pm\Delta_c/2$). The mode-hop condition is $f(\delta, R') = 0$.

We plot $f(\delta, R')$ as a function of the two-photon-detuning $\delta/2\pi$ in Fig. 57. Three curves are plotted when the pumping rate $R' = 1, 1.5,$ and 2 respectively. As the laser is tuned away from the line-center ($|\delta|$ increases), these curves pass through the $y = 0$ horizontal axis and the intersection points are where the mode-hops should happen. We see that the higher the pumping rate, the larger detuning is necessary for the mode-hop to happen; in other words, the hysteresis amount H is bigger at higher pumping rate, qualitatively agreeing with our observation.

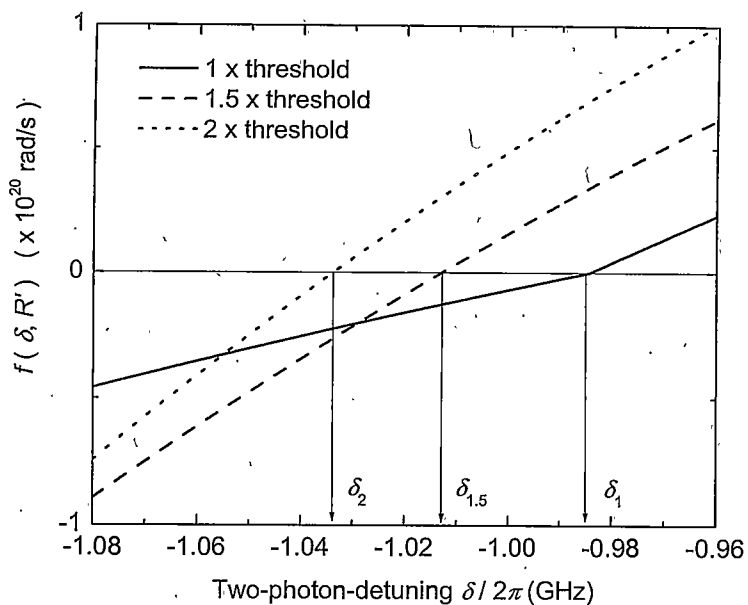


Figure 57 Plot of $f(\delta, R')$ as a function of the two-photon detuning at 3 different pumping rates. $f(\delta, R') = 0$ is when mode-hop should happen. $\delta_1/2\pi = -\Delta_c/2 = 0.985$ GHz (cavity length = 3 inch) is the symmetric point — there is no hysteresis when the laser is pumped right at the threshold. As the laser is pumped harder, we see $\delta_2 > \delta_{1.5} > \delta_1$ — the higher the pumping level, the larger the hysteresis.

Next we collect the two-photon-detuning values corresponding to $f(\delta, R') = 0$ (i.e., $\delta_1, \dots, \delta_{1.5}, \dots, \delta_2, \dots$ in Fig. 57) and convert them into the hysteresis amount H using the relation

$$\begin{aligned}
 H(R') &= 2 \frac{(|\delta_{R'}| - \Delta_c/2)}{1 - \lambda_p/\lambda_s} \frac{1}{2\pi} \\
 &= \frac{H'(R')}{1 - \lambda_p/\lambda_s} \frac{1}{2\pi},
 \end{aligned} \tag{5.26}$$

where $H'(R') = 2(|\delta_{R'}| - \Delta_c/2)$ is the amount of hysteresis expressed in two-photon-detuning (see Fig. 55). However, the hysteresis amount H defined in Fig. 53 is the measurement in the *pump* frequency. Hence we have to convert from H' to H by dividing a factor $1 - \lambda_p/\lambda_s$ (for the reason, see Eq. (3.15) and the discussions in that

section.)

Then we plot the hysteresis amount as a function of the pumping rate in Fig. 58. The experimental measurement is also included for comparison. We see good agreement between the theory and data, confirming the correctness of our theory.

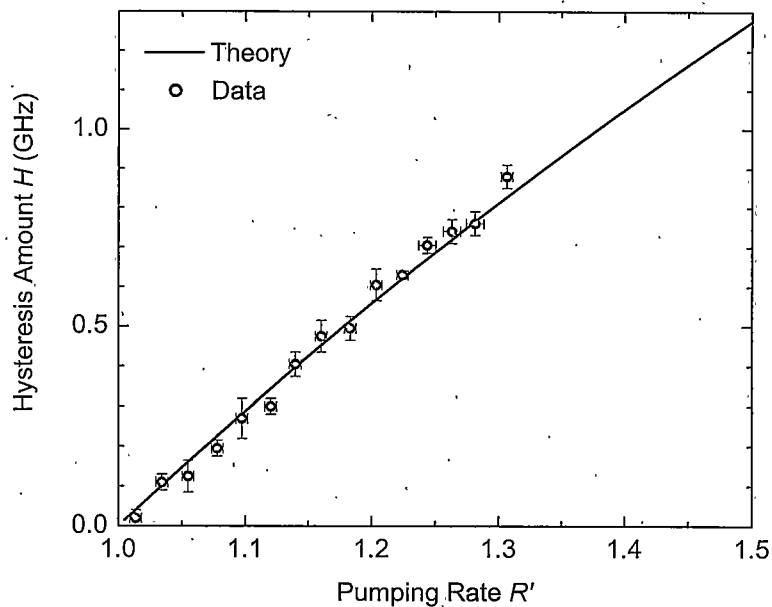


Figure 58 Plot of H as a function of the pumping rate R' . Circles are the experimental measurements.

Actually the nearly perfect theory fitting to the data is unexpected to us — we expected to measure a smaller hysteresis amount than predicted because any acoustic vibrations and(or) laser frequency fluctuations can induce premature mode-hops. However, in our theory, we did not consider any higher-order interactions (there should be more sidebands on the coherence and the pump and Stokes fields) because

they are further away from the Raman gain line-center. We think that this simplification in the theory happens to compensate the realistic perturbations such that good agreement between theory and data is achieved.

Finally, there is one last problem remaining in query: we note tuning asymmetry in the power measurements in Fig. 54 (see the different slopes of the transmitted pump and Stokes powers for the two modes). Because the Raman gain profile should be symmetric, the two Stokes modes at the two sides should exhibit the same tuning characteristics. Therefore the symmetric butterfly-like pattern is expected. One reason causing the asymmetry is the frequency-dependent mirror reflectance. See Chapter 4, the etalon effect of the cavity mirrors causes significant modulation of the mirror reflectance. This effect leads to Stokes threshold change as the pump frequency is tuned and thus the asymmetric tuning patterns for the two Stokes modes. Of course, there might be some other reasons unknown. For example, is the rotational Raman gain profile itself asymmetric for some reason?

In summary, in this Chapter we found a hysteresis effect associated with the longitudinal-mode-hop in a cw rotational Raman laser. Our model based on Raman-assisted multi-wave mixings successfully explains the experimental measurements.

CHAPTER 6

SUMMARY

In this thesis, we studied the far-off-resonance continuous-wave Raman laser both theoretically and experimentally.

The theoretical study was made in Chapter 2. A semi-classical theory for the far-off-resonance Raman process was developed in a standing-wave Fabry-Perot cavity. The far-off-resonance condition allowed us to use the adiabatic following approximation (i.e., the dynamics of the coherence can be ignored) for the time-dependent field equations. This theory was suitable for arbitrary number of intracavity fields. We used it in the two-field case — the Stokes laser, and then in the three-field case — the Stokes-anti-Stokes coupling. Both steady-state analytical and time-dependent numerical solutions were performed.

Experimentally, we demonstrated cw Raman lasers pumped by diode lasers in high-pressure H_2 gas. Our experiments achieved wide tunability [18] and high conversion efficiency [20] of the vibrational Stokes output. The theory agreed well with the experimental data in the steady state. In addition to the vibrational Stokes output, the rotational Stokes emission was also obtained [11] in one of our cw Raman systems. Details of these experiments were given in Chapter 3 and 4.

Furthermore, in Chapter 5, longitudinal-mode bistability and mode-hop hysteresis

in the rotational Stokes laser were experimentally observed. A theory based on a Raman-assisted multi-wave mixing process successfully explained the observation. To the author's knowledge, this was the first time that the longitudinal-mode-hop hysteresis in a homogeneous laser was *directly* measured.

Since the first demonstration of the far-off-resonance cw Raman laser in 1998 [16], many important advances and exciting discoveries have been accomplished. However, there still exist countless topics and opportunities for the future research in this field. For example, the experimental realization of the high-efficiency cw anti-Stokes emission, the further study on the bistability, the mode-mode competition, and the dynamic behavior in the cw Raman laser, as well as the possibility of reaching the region of electromagnetically-induced-transparency in the cw Raman laser, and so on. The cw Raman laser is not only a technique for optical frequency conversion, but also a unique tool for studies in the field of optical physics.

APPENDICES

APPENDIX A — LASER LOCKING

This Appendix will help to understand and perform the Pound-Drever-Hall (PDH) locking technique [48]. It first provides a mathematical derivation for understanding how the error signal is produced. Then the diagrams of some key electronics used for the PDH-locking in this thesis are attached.

The Error Signal

This section shows mathematically how the error signal is produced in the Pound-Drever-Hall locking technique. A similar derivation can be found in References [57, 58].

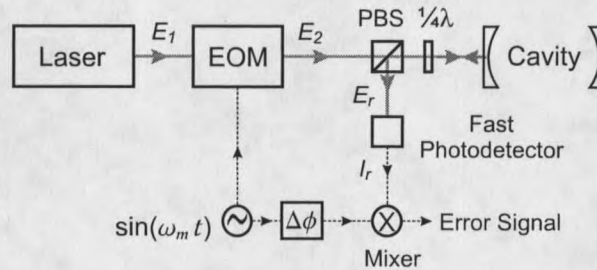


Figure 59 Illustration of the Pound-Drever-Hall laser stabilization technique. EOM: electrooptic modulator; PBS: polarizing beam splitter; $\frac{\lambda}{4}$: quarter-wave plate.

Adding sidebands

We start from an optical field with the form

$$E_1(t) = E_0 e^{i(\omega_L t)}, \quad (6.1)$$

where ω_L is the laser frequency. Using an electrooptic modulator (EOM), one can modulate the phase of the optical field:

$$E_2(t) = E_0 e^{i(\omega_L t + M \cdot \sin \omega_m t)}, \quad (6.2)$$

where ω_m is the modulation frequency and M is the modulation index. Eq.(6.2) can be expanded in terms of the first kind Bessel functions J_n [59, Page 987]:

$$E_2(t) = E_0 \sum_{n=-\infty}^{+\infty} J_n(M) e^{i(\omega_L + n\omega_m)t}, \quad (6.3)$$

This shows that the phase modulation in Eq.(6.2) results in a comb-like spectrum; the separation between these frequency components is the modulation frequency ω_m . In the limit of small modulation index ($M \ll 1$), $J_0(M) \approx 1$, $J_{\pm 1}(M) \approx \pm \frac{M}{2}$ and all the higher order J_n 's vanish. Then

$$E_2(t) \approx E_0 \left[e^{i\omega_L t} + \frac{M}{2} e^{i(\omega_L + \omega_m)t} - \frac{M}{2} e^{i(\omega_L - \omega_m)t} \right]. \quad (6.4)$$

Therefore, we obtain two small sidebands having frequency offsets of $\pm\omega_m$ from the carrier frequency ω_L ; the two sidebands have 180° phase difference.

Detecting cavity reflection

Next the field of Eq.(6.4) will be reflected from a Fabry-Perot cavity. We define the following parameters of the cavity: L : cavity length; $r_{1(2)}$: front (back) mirror's amplitude reflection coefficient; $t_{1(2)}$: front (back) mirror's amplitude transmission coefficient. When an optical field with an arbitrary frequency ω is incident on a Fabry-Perot cavity, the cavity has an effective amplitude reflection coefficient in the form

$$r(\omega) = r_1 - \frac{r_2 t_1^2 e^{-j\omega \cdot 2L/c}}{1 - r_1 r_2 e^{-j\omega \cdot 2L/c}}. \quad (6.5)$$

After being reflected, Eq.(6.4) has the form

$$E_r(t) = E_0 \left[r(\omega_L) \cdot e^{i\omega_L t} + r(\omega_L + \omega_m) \cdot \frac{M}{2} e^{i(\omega_L + \omega_m)t} - r(\omega_L - \omega_m) \cdot \frac{M}{2} e^{i(\omega_L - \omega_m)t} \right]. \quad (6.6)$$

A photodetector receives the intensity of this field:

$$I_r(t) = E_r E_r^*. \quad (6.7)$$

Substituting in Eq.(6.6), discarding the dc terms and the terms oscillating at $2\omega_m$, we obtain

$$I_r(t) = |E_0|^2 \frac{M}{2} \left\{ \text{Re}[F(\omega_L)] \cos \omega_m t + \text{Im}[F(\omega_L)] \sin \omega_m t \right\}, \quad (6.8)$$

where

$$F(\omega_L) = r(\omega_L) r^*(\omega_L + \omega_m) - r^*(\omega_L) r(\omega_L - \omega_m). \quad (6.9)$$

Eq.(6.8) tells us that the output of the photodetector is a signal oscillating at the modulation frequency ω_m . This signal has an in-phase amplitude $\text{Im}[F(\omega_L)]$ and a quadrature amplitude $\text{Re}[F(\omega_L)]$.

Obtaining error signal

After a phase adjustment, the original modulation signal $\sin(\omega_m t + \Delta\phi)$ is multiplied by the signal of Eq.(6.8) by use of an electronic mixer:

$$\text{E.S.} = I_r \times \sin(\omega_m t + \Delta\phi). \quad (6.10)$$

Dropping the terms oscillating at $2\omega_m$, we obtain

$$\text{E.S.} = |E_0|^2 \frac{M}{2} \left\{ \text{Re}[F(\omega_L)] \sin \Delta\phi + \text{Im}[F(\omega_L)] \cos \Delta\phi \right\}. \quad (6.11)$$

This is the mathematical form of the error signal.

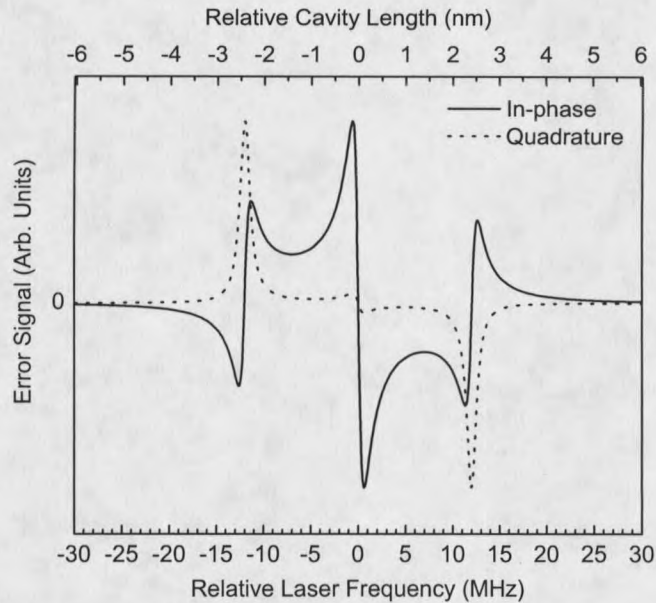


Figure 60 Calculated error signal shape from Eq.(6.11) when either the laser frequency ω_L or the cavity length L is scanned. The in-phase signal is obtained when $\Delta\phi = 0$; the quadrature signal is when $\Delta\phi = \pi/2$. Following parameters are used in calculation: modulation frequency: 12 MHz; mirror reflectance: 0.998 for both mirrors; laser wavelength: 792 nm; cavity length: 7.62 cm.

The Electronics

EOM driver

This is the rf sine-wave generator and phase shifter that drives the electrooptic modulator and the mixer (Fig. 61). The phase shifter design uses the trigonometric identity

$$\sin \omega t \sin \phi + \cos \omega t \cos \phi = \cos(\omega t - \phi)$$

to accomplish a phase shift by ϕ . The circuit was designed by Dr. C. Michael Jefferson

at the IBM Almaden research center.

Post – mixer amplifier

This single-chip amplifier is used after the mixer to amplify the error signal (Fig. 62).

Fast servo

The fast servo controls the diode laser's injection current. For the circuit diagram, see the Appendix in Ref. [23].

Slow servo

The slow servo controls the cavity's PZT to adjust the cavity's length. For the circuit diagram, see the Appendix in Ref. [23].

Diode laser current driver

See Ref. [60].

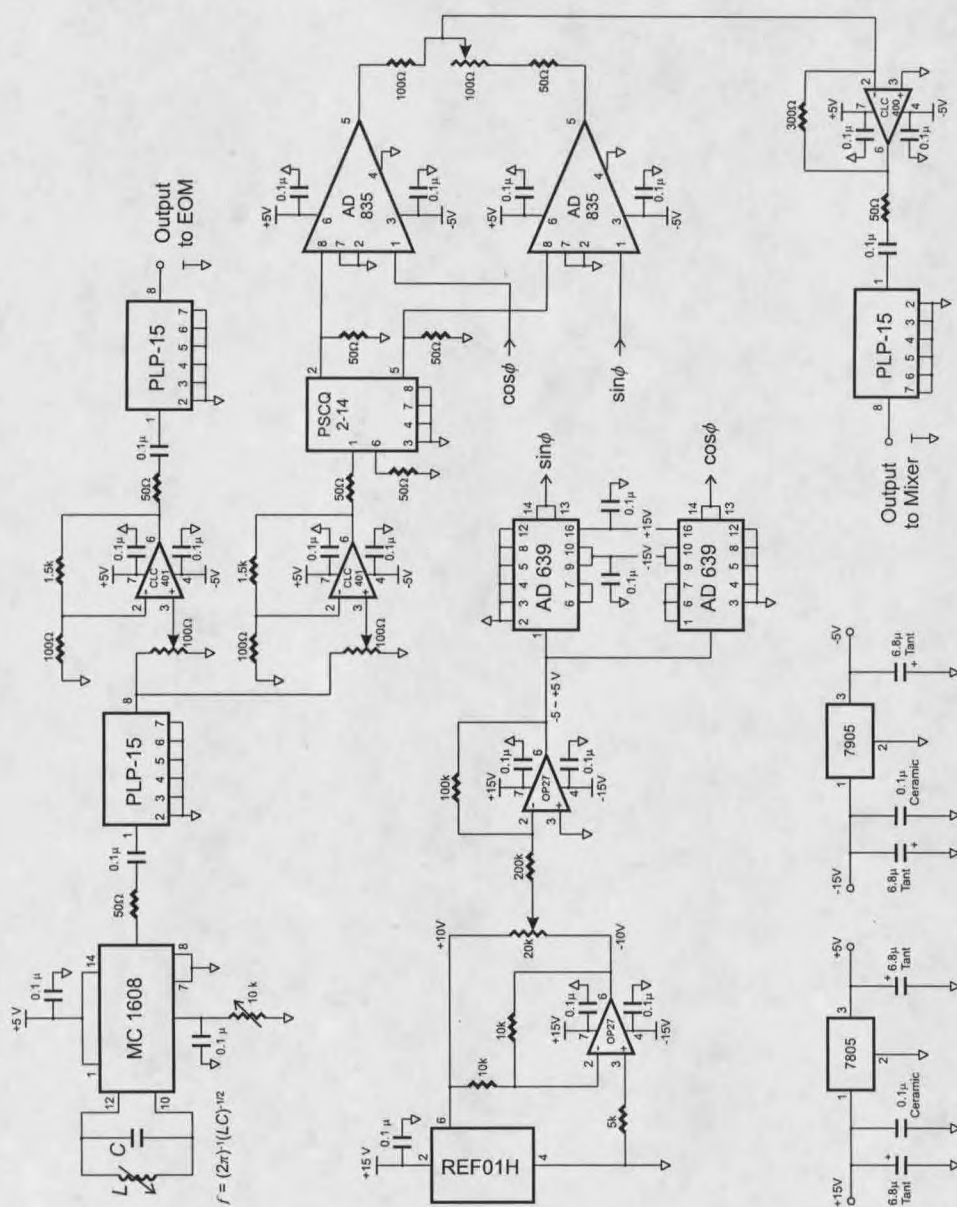
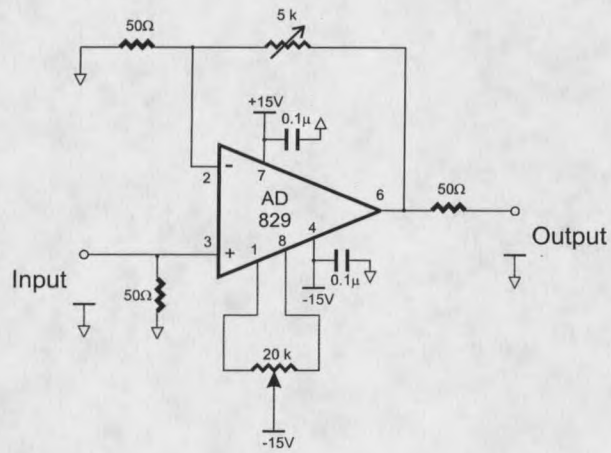


Figure 61 Electronic circuit diagram of the EOM driver and phase shifter. It can produce rf sine wave to two output channels. Relative phase of the two channels is adjustable.



Voltage Source Bypass:

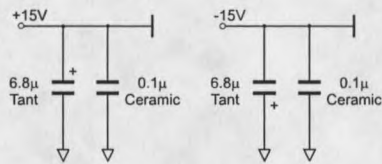


Figure 62 Electronic circuit diagram of the error signal amplifier. It has variable gain (5kΩ pot) and adjustable dc offset (20kΩ pot).

APPENDIX B — MATHEMATICA PROGRAM

This Appendix gives the MATHEMATICA [35] program used in page 36, which gives the numerical solution to the Stokes laser; and in page 50, which gives the numerical solution to the anti-Stokes problem.

MathematicaForPrint.nb

1

Numerical solution cw Raman

6ed Lei-Meng June 2002

□ Define parameters for rotational: (time: μ s, field: true intracavity value)

```

r = 0.9999; tr = 1 - r - 0.00003; c = 3 10^8; l = 0.0762; rad = 0.5; b = sqrt(1 (2 rad - 1));
Yp = c / 1 (1 - r) 10^-6; Ys = Yp; Ya = Yp; Yo = 2 c / 1 sqrt(tr) 10^-6; (* cavity decay rates in MHz *)
g = 2.36 10^-7 10^-6; (* Raman gain, rotational (vib: 5.83 E-7) *)
Yz = .5; (* Raman gain linewidth HWHM GHz, rotational (vib: .25) *)
wp = 2 pi c / 792 10^-9; (* Pump Frequency *)
ws = 2 pi c / 830 10^-9; (* Stokes Frequency *)
wa = 2 pi c / 757 10^-9; (* antiStokes Frequency *)
Cc = .485; (* coupling coefficient or phase matching term, vib, 10 atm *)
xi = - 1 / 2 Cc ( Ya ( wa / ws )^2 wp + wa + 1 ) +
1 / 2 Cc sqrt ( ( Ya ( wa / ws )^2 wp + wa + 1 )^2 - 4 Ya ( wa / ws )^2 Cc^2 ) (* ratio ea/es at linecenter *)
eth = Yp / Yo sqrt ( Ya / 2 g ); (* threshold field amplitude, pure Stokes, linecenter *)
etha = Yp / Yo sqrt ( Ya / 2 g ( 1 + xi Cc ) ); (* threshold field amplitude, antiStokes, linecenter *)
mu = 1.26 10^-6; fp = pi b / 4 wp mu; fs = pi b / 4 ws mu; fa = pi b / 4 wa mu;
(* factors for converting field to power *)
pth = fp eth^2 (* linecenter threshold power *)
ptha = fp etha^2
<< Statistics`DescriptiveStatistics` (* load statistics funtions *)

```

□ Define parameters for vibrational: (time: μs , field: true intracavity value)

```

r = 0.9999; tr = 1 - r - 0.00003; c = 3 10^8; l = 0.0762; rad = 0.5; b =  $\sqrt{1 - (2 \text{ rad} - 1)}$ ;
 $\gamma_p = \frac{c}{l} (1 - r) 10^{-6}$ ;  $\gamma_a = \gamma_p$ ;  $\gamma_s = \gamma_p$ ;  $\gamma_o = \frac{2 c}{l} \sqrt{\text{tr}} 10^{-6}$ ; (* cavity decay rates in MHz *)
g = 5.83 10^{-7} 10^{-6}; (* Raman gain, vibrational *)
 $\gamma_r = .25$ ; (* Raman gain linewidth HWHM GHz, vibrational *)
 $\omega_p = \frac{2 \pi c}{792 10^{-9}}$ ; (* Pump Frequency *)
 $\omega_s = \frac{2 \pi c}{1180 10^{-9}}$ ; (* Stokes Frequency *)
 $\omega_a = \frac{2 \pi c}{596 10^{-9}}$ ; (* antiStokes Frequency *)
Cc = .179; (* coupling coefficient or phase matching term, vib, 10 atm *)
 $\xi = -\frac{1}{2 Cc} \left( \frac{\gamma_a}{\gamma_s} \left( \frac{\omega_a}{\omega_s} \right)^2 \frac{\omega_p + \omega_a}{\omega_p + \omega_a} + 1 \right) +$ 
 $\frac{1}{2 Cc} \sqrt{\left( \frac{\gamma_a}{\gamma_s} \left( \frac{\omega_a}{\omega_s} \right)^2 \frac{\omega_p + \omega_a}{\omega_p + \omega_a} + 1 \right)^2 - 4 \frac{\gamma_a}{\gamma_s} \left( \frac{\omega_a}{\omega_s} \right)^2 Cc^2}$  (* ratio ea/es at linecenter *)
eth =  $\frac{\gamma_p}{\gamma_o} \sqrt{\frac{\gamma_a}{2 g}}$ ; (* threshold field amplitude, pure Stokes, linecenter *)
etha =  $\frac{\gamma_p}{\gamma_o} \sqrt{\frac{\gamma_a}{2 g (1 + \xi Cc)}}$ ; (* threshold field amplitude, antiStokes, linecenter *)
 $\mu = 1.26 10^{-6}$ ;  $fp = \frac{\pi b}{4 \omega_p \mu}$ ;  $fs = \frac{\pi b}{4 \omega_s \mu}$ ;  $fa = \frac{\pi b}{4 \omega_a \mu}$ ;
(* factors for converting field to power *)
pth = fp eth^2 (* threshold power *)
ptha = fp etha^2
<< Statistics`DescriptiveStatistics` (* load statistics funtions *)

```

□ Numerical Solution for Stokes Laser

■ Time-dependent solution (complex amplitudes):

```

eep =  $\sqrt{4}$  eth; (* pump field amplitude *)
 $\delta = 0.4$ ; (* two-photon detuning in GHz *)
eq1 = ep'[t] ==
  - $\frac{\gamma_p}{2}$  ep[t] -  $\left(\frac{\omega_p}{\omega_s}\right)^2 g \frac{\gamma_r^2}{\gamma_r^2 + \delta^2} \left(1 - i \frac{\delta}{\gamma_r}\right)$  es[t] Conjugate[es[t]] ep[t] +  $\frac{\gamma_o}{2}$  eep  $\frac{ep[t]}{Abs[ep[t]]}$ 
eq2 = es'[t] == - $\frac{\gamma_s}{2}$  es[t] +  $g \frac{\gamma_r^2}{\gamma_r^2 + \delta^2} \left(1 + i \frac{\delta}{\gamma_r}\right)$  ep[t] Conjugate[ep[t]] es[t]
Sol = NDSolve
  [{eq1, eq2, ep[0] == 0.00001, es[0] == 1.8}, {ep, es}, {t, 0, 2000}, MaxSteps -> 2000000];

(* This cell calculates what the Stokes initial condition means *)
 $\xi = 6.626 \cdot 10^{-34} \times \frac{c}{1180 \cdot 10^{-9}}$ ; (* energy of one photon *)
 $\eta = 2 l / c$ ; (* round-trip time in cavity *)
 $\xi / \eta$  (* power of a single-photon traveling-wave in cavity *)
 $fs = 1.8^2$  (* this is the initial condition of Stokes field power *)
 $3.3161 \times 10^{-10}$ 
 $3.35438 \times 10^{-10}$ 

(* Plot pump and Stokes time-dependent intracavity power *)
pp =
  Plot[Evaluate[fp Abs[ep[t]]^2 /. Sol], {t, 0, 1000}, Frame -> True, GridLines -> Automatic,
  FrameLabel -> {TIME, Pump}, PlotRange -> All, PlotStyle -> {Thickness[0.008]};
ps = Plot[Evaluate[fs Abs[es[t]]^2 /. Sol], {t, 0, 1000}, Frame -> True,
  GridLines -> Automatic, FrameLabel -> {TIME, Stokes},
  PlotRange -> All, PlotStyle -> {Thickness[0.008]};

(* Plot pump and Stokes time-dependent phase *)
pfp =
  Plot[Evaluate[ $\frac{-Arg[ep[t]]}{\pi}$  /. Sol], {t, 0, 1000}, Frame -> True, GridLines -> Automatic,
  FrameLabel -> {TIME, Pump}, PlotRange -> All, PlotStyle -> {Thickness[0.008]};
pfs = Plot[Evaluate[ $\frac{-Arg[es[t]]}{\pi}$  /. Sol], {t, 0, 1000}, Frame -> True,
  GridLines -> Automatic, FrameLabel -> {TIME, Stokes},
  PlotRange -> All, PlotStyle -> {Thickness[0.008]};

```

■ Export the solutions

```
t1 = Table[1, {1, 0, 1000, .5}];
pump = Flatten[Table[Evaluate[fp Abs[ep[t]]^2 /. Sol], {t, 0, 1000, .5}]];
stokes = Flatten[Table[Evaluate[fs Abs[es[t]]^2 /. Sol], {t, 0, 1000, .5}]];
powerdata = Transpose[{t1, pump, stokes}];
Export["D:\MathematicaData\powertime.dat", powerdata]
t2 = Table[1, {1, 1900, 2000, .5}];
pph = Flatten[Table[Evaluate[ $\frac{-\text{Arg}[ep[t]]}{\pi}$  /. Sol], {t, 1900, 2000, .5}]];
sph = Flatten[Table[Evaluate[ $\frac{-\text{Arg}[es[t]]}{\pi}$  /. Sol], {t, 1900, 2000, .5}]];
phasedata = Transpose[{t2, pph, sph}];
Export["D:\MathematicaData\phasetime.dat", phasedata]
```

■ Calculate steady-state values as function of tuning

```
eep = 2 eth; (* pump field amplitude *)
eq1 = ep'[t] ==
  - $\frac{\gamma_p}{2}$  ep[t] -  $\left(\frac{\omega_p}{\omega_n}\right)^2 g \frac{\gamma_r^2}{\gamma_r^2 + \delta^2} \left(1 - i \frac{\delta}{\gamma_r}\right)$  es[t] Conjugate[es[t]] ep[t] +  $\frac{\gamma_e}{2}$  eep  $\frac{ep[t]}{\text{Abs}[ep[t]}}$ 
eq2 = es'[t] == - $\frac{\gamma_s}{2}$  es[t] +  $g \frac{\gamma_r^2}{\gamma_r^2 + \delta^2} \left(1 + i \frac{\delta}{\gamma_r}\right)$  ep[t] Conjugate[ep[t]] es[t]
Do[
  Sol[ $\delta$ ] = NDSolve
    [(eq1, eq2, ep[0] == 0.00001, es[0] == 1.8), {ep, es}, {t, 0, 2000}, MaxSteps -> 2000000];
  Print[ $\delta$ ],
  { $\delta$ , - $\frac{100}{100}$ ,  $\frac{100}{100}$ ,  $\frac{5}{100}$ }}];
```

```
(* Plot steady-state tuning curves *)
epSS = {};
Do[
  (*Print[ $\delta$  100];*)
  epSS = Append[epSS,  $\delta$  // N];

  epSSData = Mean[Flatten[Table[Evaluate[Abs[ep[t]] /. Sol[ $\delta$ ]], {t, 1900, 2000, 1}]]];
  epSS = Append[epSS, epSSData],
  { $\delta$ , - $\frac{100}{100}$ ,  $\frac{100}{100}$ ,  $\frac{5}{100}$ }}];
epSS = Partition[epSS, 2];
esSS = {};
Do[
  (*Print[ $\delta$  100];*)
  esSS = Append[esSS,  $\delta$  // N];

  esSSData = Mean[Flatten[Table[Evaluate[Abs[es[t]] /. Sol[ $\delta$ ]], {t, 1900, 2000, 1}]]];
  esSS = Append[esSS, esSSData],
  { $\delta$ , - $\frac{100}{100}$ ,  $\frac{100}{100}$ ,  $\frac{5}{100}$ }}];
esSS = Partition[esSS, 2];

ListPlot[epSS, PlotJoined -> True, PlotRange -> All];
ListPlot[esSS, PlotJoined -> True, PlotRange -> All];
```

```

(* Plot steady-state tuning curves of frequency pulling *)
fppSS = {}; (* fp means frequency pulling *)
Do[
  fppSS = Append[fppSS,  $\delta$  // N];
  data = Flatten[Table[Evaluate[Arg[ep[t]] /. Sol[ $\delta$ ]], {t, 1900, 2000, 1}]];
  slop = {};
  Do[
    d = Part[data, t + 1] - Part[data, t];
    If[Abs[d] <  $\pi$ , slop = Append[slop, -d]],
    {t, 1, 100, 1}];
  fppSS = Append[fppSS, Mean[slop]],
  { $\delta$ , - $\frac{100}{100}$ ,  $\frac{100}{100}$ ,  $\frac{5}{100}$ }}];
fppSS = Partition[fppSS, 2];

fpsSS = {}; (* fp means frequency pulling *)
Do[
  fpsSS = Append[fpsSS,  $\delta$  // N];
  data = Flatten[Table[Evaluate[Arg[es[t]] /. Sol[ $\delta$ ]], {t, 1900, 2000, 1}]];
  slop = {};
  Do[
    d = Part[data, t + 1] - Part[data, t];
    If[Abs[d] <  $\pi$ , slop = Append[slop, -d]],
    {t, 1, 100, 1}];
  fpsSS = Append[fpsSS, Mean[slop]],
  { $\delta$ , - $\frac{100}{100}$ ,  $\frac{100}{100}$ ,  $\frac{5}{100}$ }}];
fpsSS = Partition[fpsSS, 2];

ListPlot[fppSS, PlotJoined -> True, PlotRange -> All];
ListPlot[fpsSS, PlotJoined -> True, PlotRange -> All];

```

■ Export the solutions

```

Export["D:\MathematicaData\FreqPullp.dat", fppSS]
Export["D:\MathematicaData\FreqPulls.dat", fpsSS]

```

Plot steady-state values as function of pump power

```

δ = 0; (* two-photon detuning in GHz *)
eq1 = ep'[t] == - $\frac{\gamma_p}{2}$  ep[t] -
       $\left(\frac{\omega_p}{\omega_s}\right)^2 g \frac{\gamma_r^2}{\gamma_r^2 + \delta^2} \left(1 - i \frac{\delta}{\gamma_r}\right) es[t] \text{Conjugate}[es[t]] ep[t] + \frac{\gamma_s}{2} eep \frac{ep[t]}{\text{Abs}[ep[t] ]}$ ;
eq2 = es'[t] == - $\frac{\gamma_s}{2}$  es[t] + g  $\frac{\gamma_r^2}{\gamma_r^2 + \delta^2} \left(1 + i \frac{\delta}{\gamma_r}\right) ep[t] \text{Conjugate}[ep[t]] es[t]$ ;
Do[
  Sol[eep] = NDSolve
    [(eq1, eq2, ep[0] == 0.00001, es[0] == 1.8), {ep, es}, {t, 0, 2000}, MaxSteps -> 2000000];
  If[IntegerQ[eep/1000], Print[eep, "--", fp eep^2],
    {eep, 0, 27000, 100}];

ppSS = {};
Do[
  ppSS = Append[ppSS, fp eep^2 1000 // N];
  data = Mean[Flatten[Table[Evaluate[fp Abs[ep[t]]^2 /. Sol[eep]], {t, 1900, 2000, 1}]]];
  ppSS = Append[ppSS, data],
  {eep, 0, 12000, 100}];
ppSS = Partition[ppSS, 2];
ListPlot[ppSS, PlotJoined -> True, PlotRange -> All];

psSS = {};
Do[
  psSS = Append[psSS, fp eep^2 1000 // N];
  data = Mean[Flatten[Table[Evaluate[fs Abs[es[t]]^2 /. Sol[eep]], {t, 1900, 2000, 1}]]];
  psSS = Append[psSS, data],
  {eep, 0, 12000, 100}];
psSS = Partition[psSS, 2];
ListPlot[psSS, PlotJoined -> True, PlotRange -> All];

```

■ Numerical Solution for Anti-Stokes Emission

■ Field equations (complex amplitudes):

$$\begin{aligned} \text{eq1} &= \text{ep}'[t] = -\frac{\gamma_p}{2} \text{ep}[t] - \left(\frac{\omega_p}{\omega_n}\right)^2 g \frac{\gamma_x^2}{\gamma_x^2 + \delta^2} \left(1 - i \frac{\delta}{\gamma_x}\right) \text{es}[t] \text{Conjugate}[\text{es}[t]] \text{ep}[t] + \\ &\quad \left(\frac{\omega_p}{\omega_n}\right)^2 \frac{\omega_p + \omega_n}{\omega_p + \omega_n} g \frac{\gamma_x^2}{\gamma_x^2 + \delta^2} \left(1 + i \frac{\delta}{\gamma_x}\right) \text{ea}[t] \text{Conjugate}[\text{ea}[t]] \text{ep}[t] + \\ &\quad 2i \frac{\delta}{\gamma_x} \left(\frac{\omega_p}{\omega_n}\right)^2 g \frac{\gamma_x^2}{\gamma_x^2 + \delta^2} \text{Cc} \text{Conjugate}[\text{ep}[t]] \text{es}[t] \text{ea}[t] + \frac{\gamma_a}{2} \text{eep} \frac{\text{ep}[t]}{\text{Abs}[\text{ep}[t]]} \\ \text{eq2} &= \text{es}'[t] = -\frac{\gamma_s}{2} \text{es}[t] + g \frac{\gamma_x^2}{\gamma_x^2 + \delta^2} \left(1 + i \frac{\delta}{\gamma_x}\right) \text{ep}[t] \text{Conjugate}[\text{ep}[t]] \text{es}[t] + \\ &\quad g \frac{\gamma_x^2}{\gamma_x^2 + \delta^2} \left(1 + i \frac{\delta}{\gamma_x}\right) \text{Cc} \text{ep}[t]^2 \text{Conjugate}[\text{ea}[t]] \\ \text{eq3} &= \text{ea}'[t] = -\frac{\gamma_a}{2} \text{ea}[t] - \left(\frac{\omega_a}{\omega_n}\right)^2 \frac{\omega_p + \omega_n}{\omega_p + \omega_n} g \frac{\gamma_x^2}{\gamma_x^2 + \delta^2} \left(1 - i \frac{\delta}{\gamma_x}\right) \text{ep}[t] \text{Conjugate}[\text{ep}[t]] \text{ea}[t] - \\ &\quad \left(\frac{\omega_a}{\omega_n}\right)^2 g \frac{\gamma_x^2}{\gamma_x^2 + \delta^2} \left(1 - i \frac{\delta}{\gamma_x}\right) \text{Cc} \text{ep}[t]^2 \text{Conjugate}[\text{es}[t]] \end{aligned}$$

■ Time-dependent solution and plots

```
pr = 17.289;
eep = Sqrt[pr] etha; (* pump field amplitude *)
delta = 1.2; (* two-photon detuning in GHz *)
Sol = NDSolve[
  {{eq1, eq2, eq3, ep[0] == 0.00001, es[0] == 1.8, ea[0] == 0.},
  {ep, es, ea}}, {t, 0, 2000}, MaxSteps -> 2000000];

(* Plot time-dependent pump, Stokes, and anti-Stokes intracavity power *) pp =
Plot[Evaluate[fp Abs[ep[t]]^2 /. Sol], {t, 0, 2000}, Frame -> True, GridLines -> Automatic,
FrameLabel -> {TIME, Pump}, PlotRange -> All, PlotStyle -> {Thickness[0.006]};
ps = Plot[Evaluate[fs Abs[es[t]]^2 /. Sol], {t, 0, 2000}, Frame -> True,
GridLines -> Automatic, FrameLabel -> {TIME, Stokes},
PlotRange -> All, PlotStyle -> {Thickness[0.006]};
pa = Plot[Evaluate[fa Abs[ea[t]]^2 /. Sol], {t, 0, 2000}, Frame -> True,
GridLines -> Automatic, FrameLabel -> {TIME, AntiStokes},
PlotRange -> All, PlotStyle -> {Thickness[0.006]};
```

```

(* Plot time-dependent pump, Stokes, and anti-Stokes phase *)
pp2 = Plot[Evaluate[ $\frac{-\text{Arg}[ep[t]]}{\pi}$  /. Sol], {t, 1900, 2000},
  Frame -> True, GridLines -> Automatic, FrameLabel -> {TIME, Pump},
  PlotRange -> All, PlotStyle -> {Thickness[0.006]};
ps2 = Plot[Evaluate[ $\frac{-\text{Arg}[es[t]]}{\pi}$  /. Sol], {t, 1900, 2000}, Frame -> True,
  GridLines -> Automatic, FrameLabel -> {TIME, Stokes},
  PlotRange -> All, PlotStyle -> {Thickness[0.006]};
pa2 = Plot[Evaluate[ $\frac{-\text{Arg}[ea[t]]}{\pi}$  /. Sol], {t, 1900, 2000}, Frame -> True,
  GridLines -> Automatic, FrameLabel -> {TIME, AntiStokes},
  PlotRange -> All, PlotStyle -> {Thickness[0.006]};
(* Time-dependent phase difference *)
pas = Plot[Evaluate[ $\frac{\text{Arg}[es[t]] + \text{Arg}[ea[t]] - 2 \text{Arg}[ep[t]]}{\pi}$  /. Sol],
  {t, 0, 2000}, Frame -> True, GridLines -> Automatic, FrameLabel -> {TIME, Total},
  PlotRange -> All, PlotStyle -> {Thickness[0.006]};

(* Smooth the phase difference, e.g.,  $\pi$  is equivalent to  $-\pi$  *)
x = Flatten[
  Table[Evaluate[ $\frac{\text{Arg}[es[t]] + \text{Arg}[ea[t]] - 2 \text{Arg}[ep[t]]}{\pi}$  /. Sol], {t, 1, 1000, 1}];
pdif = {};
Do[pdif = Append[pdif, t];
  y = Part[x, t];
  z1 = If[y > 2, y - 2, If[y > 1, y - 1, y]];
  z2 = If[z1 < -2, z1 + 3, If[z1 < -1, z1 + 2, If[z1 < 0, z1 + 1, z1]]];
  z = If[z2 < 0.1, z2 + 1, z2];
  pdif = Append[pdif, z],
  {t, 1, 1000, 1}
];
pdif = Partition[pdif, 2];
ListPlot[pdif, PlotJoined -> True, PlotRange -> All];

```

■ Export the solutions

```

t1 = Table[i, {i, 0, 1000, .5}];
pump = Flatten[Table[Evaluate[fp Abs[ep[t]]2 /. Sol], {t, 0, 1000, .5}]];
stokes = Flatten[Table[Evaluate[fs Abs[es[t]]2 /. Sol], {t, 0, 1000, .5}]];
antist = Flatten[Table[Evaluate[fa Abs[ea[t]]2 /. Sol], {t, 0, 1000, .5}]];
powerdata = Transpose[{t1, pump, stokes, antist}];
Export["D:\MathematicaData\powertime.dat", powerdata]
t2 = Table[i, {i, 1900, 2000, .5}];
pph = Flatten[Table[Evaluate[ $\frac{-\text{Arg}[ep[t]]}{\pi}$  /. Sol], {t, 1900, 2000, .5}]];
sph = Flatten[Table[Evaluate[ $\frac{-\text{Arg}[es[t]]}{\pi}$  /. Sol], {t, 1900, 2000, .5}]];
aph = Flatten[Table[Evaluate[ $\frac{-\text{Arg}[ea[t]]}{\pi}$  /. Sol], {t, 1900, 2000, .5}]];
phasedata = Transpose[{t2, pph, sph, aph}];
Export["D:\MathematicaData\phasetime.dat", phasedata]
Export["D:\MathematicaData\phdifftime.dat", pdif]

```

■ Calculate steady-state values as function of tuning

```

eep =  $\sqrt{16}$  etha; (* pump field amplitude *)
Do[
  Sol[ $\delta$ ] = NDSolve
    [{eq1, eq2, eq3, ep[0] == 0.00001, es[0] == 1.8, ea[0] == 0.},
     {ep, es, ea}, {t, 0, 2000}, MaxSteps -> 2000000];
  If[IntegerQ[ $\delta$ 10], Print[ $\delta$ ],
    { $\delta$ ,  $\frac{150}{100}$ ,  $\frac{150}{100}$ ,  $\frac{2}{100}$ }}];

```

```

epSS = {};
Do[
  (*Print[δ 100];*)
  epSS = Append[epSS, δ // N];

  epSSData =
    Mean[Flatten[Table[Evaluate[fp Abs[ep[t]]^2 /. Sol[δ]], {t, 1900, 2000, 1}]]];
  epSS = Append[epSS, epSSData],
  {δ, - $\frac{150}{100}$ ,  $\frac{150}{100}$ ,  $\frac{2}{100}$ }}];
epSS = Partition[epSS, 2];
esSS = {};
Do[
  (*Print[δ 100];*)
  esSS = Append[esSS, δ // N];

  esSSData =
    Mean[Flatten[Table[Evaluate[fs Abs[es[t]]^2 /. Sol[δ]], {t, 1900, 2000, 1}]]];
  esSS = Append[esSS, esSSData],
  {δ, - $\frac{150}{100}$ ,  $\frac{150}{100}$ ,  $\frac{2}{100}$ }}];
esSS = Partition[esSS, 2];
eaSS = {};
Do[
  (*Print[δ 100];*)
  eaSS = Append[eaSS, δ // N];

  eaSSData =
    Mean[Flatten[Table[Evaluate[fa Abs[ea[t]]^2 /. Sol[δ]], {t, 1900, 2000, 1}]]];
  eaSS = Append[eaSS, eaSSData],
  {δ, - $\frac{150}{100}$ ,  $\frac{150}{100}$ ,  $\frac{2}{100}$ }}];
eaSS = Partition[eaSS, 2];
(* Plot pump, Stokes, and anti-Stokes intracavity powers as function of tuning *)
ListPlot[epSS, PlotJoined → True, PlotRange → All];
ListPlot[esSS, PlotJoined → True, PlotRange → All];
ListPlot[eaSS, PlotJoined → True, PlotRange → All];

```

```

fppSS = {}; (* fp means frequency pulling *)
Do[
  fppSS = Append[fppSS,  $\delta$  // N];
  data = Flatten[Table[Evaluate[Arg[ep[t]] /. Sol[ $\delta$ ]], {t, 1900, 2000, 1}]];
  slop = {};
  Do[
    d = Part[data, t + 1] - Part[data, t];
    If[Abs[d] <  $\pi$ , slop = Append[slop, -d],
      {t, 1, 100, 1}];
    fppSS = Append[fppSS, Mean[slop]],
    { $\delta$ , - $\frac{150}{100}$ ,  $\frac{150}{100}$ ,  $\frac{2}{100}$ }}];
fppSS = Partition[fppSS, 2];

fpsSS = {}; (* fp means frequency pulling *)
Do[
  fpsSS = Append[fpsSS,  $\delta$  // N];
  data = Flatten[Table[Evaluate[Arg[es[t]] /. Sol[ $\delta$ ]], {t, 1900, 2000, 1}]];
  slop = {};
  Do[
    d = Part[data, t + 1] - Part[data, t];
    If[Abs[d] <  $\pi$ , slop = Append[slop, -d],
      {t, 1, 100, 1}];
    fpsSS = Append[fpsSS, Mean[slop]],
    { $\delta$ , - $\frac{150}{100}$ ,  $\frac{150}{100}$ ,  $\frac{2}{100}$ }}];
fpsSS = Partition[fpsSS, 2];

fpaSS = {}; (* fp means frequency pulling *)
Do[
  fpaSS = Append[fpaSS,  $\delta$  // N];
  data = Flatten[Table[Evaluate[Arg[ea[t]] /. Sol[ $\delta$ ]], {t, 1900, 2000, 1}]];
  slop = {};
  Do[
    d = Part[data, t + 1] - Part[data, t];
    If[Abs[d] <  $\pi$ , slop = Append[slop, -d],
      {t, 1, 100, 1}];
    fpaSS = Append[fpaSS, Mean[slop]],
    { $\delta$ , - $\frac{150}{100}$ ,  $\frac{150}{100}$ ,  $\frac{2}{100}$ }}];
fpaSS = Partition[fpaSS, 2];
(* Plot pump, Stokes, and anti-Stokes frequency-pullings as function of tuning *)
ListPlot[fppSS, PlotJoined -> True, PlotRange -> All];
ListPlot[fpsSS, PlotJoined -> True, PlotRange -> All];
ListPlot[fpaSS, PlotJoined -> True, PlotRange -> All];

```

```
(* phase difference *)
ΔφSS = {};
Do[
  ΔφSS = Append[ΔφSS, δ // N];

  x = Max[Flatten[Table[
    Evaluate[ $\frac{\text{Arg}[es[t]] + \text{Arg}[ea[t]] - 2 \text{Arg}[ep[t]]}{\pi}$  /. Sol[δ]], {t, 1900, 2000, 1}]]];
  ΔφSSData = If[x > 2, x - 2, If[x < 0, x + 2, x]];
  ΔφSS = Append[ΔφSS, ΔφSSData];
  If[IntegerQ[δ 10], Print[δ],
    {δ, - $\frac{150}{100}$ ,  $\frac{150}{100}$ ,  $\frac{2}{100}$ ]];
  ΔφSS = Partition[ΔφSS, 2];
  ListPlot[ΔφSS, PlotJoined -> True, PlotRange -> All];

```

■ Export the solutions

```
Export["D:\MathematicaData\PumpTune.dat", epSS];
Export["D:\MathematicaData\StokesTune.dat", esSS];
Export["D:\MathematicaData\AsTune.dat", eaSS];
Export["D:\MathematicaData\PhasePump.dat", fppSS];
Export["D:\MathematicaData\PhaseStokes.dat", fpsSS];
Export["D:\MathematicaData\PhaseAS.dat", fpaSS];

Export["D:\MathematicaData\PhaseDif.dat", ΔφSS];

```

■ Calculate steady-state values as function of pump power

```
δ = 1.2; (* two-photon detuning in GHz *)
Do[
  'Sol[eeep] = NDSolve'
  [{eq1, eq2, eq3, ep[0] == 0.00001, es[0] == 1.8, ea[0] == 0.},
   {ep, es, ea}, {t, 0, 2000}, MaxSteps -> 2000000];

  If[IntegerQ[eeep/1000], Print[eeep, "--", fp eeep2],
   {eeep, 0, 27000, 100}];

```

```

(* intracavity powers *)
ppSS = {};
Do[
  ppSS = Append[ppSS, fp eep^2 1000 // N];
  data = Mean[Flatten[Table[Evaluate[fp Abs[ep[t]]^2 /. Sol[eep]], {t, 1900, 2000, 1}]]];
  ppSS = Append[ppSS, data],
  {eep, 0, 27000, 100}];
ppSS = Partition[ppSS, 2];
ListPlot[ppSS, PlotJoined -> True, PlotRange -> All];
psSS = {};
Do[
  psSS = Append[psSS, fp eep^2 1000 // N];
  data = Mean[Flatten[Table[Evaluate[fs Abs[es[t]]^2 /. Sol[eep]], {t, 1900, 2000, 1}]]];
  psSS = Append[psSS, data],
  {eep, 0, 27000, 100}];
psSS = Partition[psSS, 2];
ListPlot[psSS, PlotJoined -> True, PlotRange -> All];
paSS = {};
Do[
  paSS = Append[paSS, fp eep^2 1000 // N];
  data = Mean[Flatten[Table[Evaluate[fa Abs[ea[t]]^2 /. Sol[eep]], {t, 1900, 2000, 1}]]];
  paSS = Append[paSS, data],
  {eep, 0, 27000, 100}];
paSS = Partition[paSS, 2];
ListPlot[paSS, PlotJoined -> True, PlotRange -> All];

(* Phase difference *)
ΔφSS = {};
Do[
  ΔφSS = Append[ΔφSS, fp eep^2 1000 // N];

  x = Max[Flatten[Table[Evaluate[
    
$$\frac{\text{Arg}[es[t]] + \text{Arg}[ea[t]] - 2 \text{Arg}[ep[t]]}{\pi}$$

    /. Sol[eep]], {t, 1900, 2000, 1}]]];

  ΔφSSData = If[x > 2, x - 2, If[x < 0, x + 2, x]];
  ΔφSS = Append[ΔφSS, ΔφSSData];
  If[IntegerQ[eep/1000], Print[eep, "--", fp eep^2]],
  {eep, 0, 27000, 100}];
ΔφSS = Partition[ΔφSS, 2];
ListPlot[ΔφSS, PlotJoined -> True, PlotRange -> All];

```

■ Export the solutions

```

Export["D:\MathematicaData\PowerPump.dat", ppSS];
Export["D:\MathematicaData\PowerStokes.dat", psSS];
Export["D:\MathematicaData\PowerAS.dat", paSS];

Export["D:\MathematicaData\PhaseDif.dat", ΔφSS];

```

REFERENCES CITED

1. D. E. Gray, ed., *American Institute of Physics Handbook*. McGraw-Hill Book Company, Inc., second ed., 1963.
2. W. K. Bischel and M. J. Dyer, "Wavelength dependence of the absolute Raman gain coefficient for the Q(1) transition in H₂," *J. Opt. Soc. Am. B*, vol. 3, pp. 677-682, 1986.
3. W. K. Bischel and M. J. Dyer, "Temperature dependence of the Raman linewidth and line shift for the Q(1) and Q(0) transitions in normal and para-H₂," *Phys. Rev. A*, vol. 33, pp. 3113-3123, 1986.
4. J. L. Carlsten and R. G. Wenzel, "Stimulated rotational Raman scattering in CO₂ pumped para-H₂," *IEEE J. Quan. Electron.*, vol. 19, pp. 1407-1413, 1983.
5. R. W. Carlson and W. R. Fenner, "Absolute Raman scattering cross-section of molecular hydrogen," *Astrophys. J.*, vol. 178, pp. 551-556, 1972.
6. M. R. Perrone, V. Piccinno, G. D. Nunzio, and V. Nassisi, "Dependence of rotational and vibrational Raman scattering on focusing geometry," *IEEE J. Quan. Electron.*, vol. 33, pp. 938-944, 1997.
7. G. C. Herring, M. J. Dyer, and W. K. Bischel, "Temperature and density dependence of the linewidths and line shifts of the rotational Raman lines in N₂ and H₂," *Phys. Rev. A*, vol. 34, pp. 1944-1951, 1986.
8. G. L. Abbas, S. Yang, V. W. S. Chan, and J. G. Fujimoto, "Injection behavior and modeling of 100 mW broad area diode lasers," *IEEE J. Quantum Electronics*, vol. 24, pp. 609-617, 1988.
9. I. D. Lindsay and M. Ebrahimzadeh, "Efficient continuous-wave and Q-switched operation of a 946-nm Nd:YAG laser pumped by an injection-locked broad-area diode laser," *Appl. Opt.*, vol. 37, pp. 3961-3970, 1998.
10. J. Bienfang, W. Rudolph, P. A. Roos, L. S. Meng, and J. L. Carlsten, "Steady-state thermo-optic model of a continuous-wave Raman laser," *J. Opt. Soc. Am. B*, vol. 19, pp. 1318-1325, 1986.

11. L. S. Meng, P. A. Roos, and J. L. Carlsten, "Continuous-wave rotational Raman laser in H₂," *Opt. Lett.*, vol. 27, pp. 1226–1228, 2002.
12. N. Bloembergen, "The stimulated Raman effect," *Am. J. Phys.*, vol. 35, pp. 989–1023, 1967.
13. R. W. Boyd, *Nonlinear Optics*. Academic Press, 1992.
14. R. Max, U. Huber, I. Abdul-Halim, J. Heppner, Y. Ni, G. Willengerg, and C. O. Weiss, "Far-infrared cw Raman and laser gain in ¹⁴NH₃," *IEEE J. Quan. Electron.*, vol. 17, p. 1123, 1981.
15. J. K. Brasseur, T. L. Henshaw, D. K. Neumann, R. F. Teehan, and R. J. Knize, "Highly efficient, resonant Raman molecular iodine laser," *Opt. Lett.*, vol. 27, pp. 930–932, 2002.
16. J. K. Brasseur, K. S. Repasky, and J. L. Carlsten, "Continuous-wave Raman laser in H₂," *Opt. Lett.*, vol. 23, pp. 367–369, 1998.
17. P. A. Roos, J. K. Brasseur, and J. L. Carlsten, "Diode-pumped nonresonant continuous-wave Raman laser in H₂ with resonant optical feedback stabilization," *Opt. Lett.*, vol. 15, pp. 1130–1132, 1999.
18. L. S. Meng, K. S. Repasky, P. A. Roos, and J. L. Carlsten, "Widely tunable continuous-wave Raman laser in diatomic hydrogen pumped by an external-cavity diode laser," *Opt. Lett.*, vol. 25, pp. 472–474, 2000.
19. P. A. Roos, L. S. Meng, and J. L. Carlsten, "Efficient, tunable, high power cw near-infrared generation through Raman down-conversion of a diode laser in H₂," *Conference on Lasers and Electro-optics*, vol. Postdeadline papers, p. CPD24, 2000.
20. L. S. Meng, P. A. Roos, K. S. Repasky, and J. L. Carlsten, "High-conversion-efficiency, diode-pumped continuous-wave Raman laser," *Opt. Lett.*, vol. 26, pp. 426–428, 2001.
21. J. K. Brasseur, P. A. Roos, K. S. Repasky, and J. L. Carlsten, "Characterization of a continuous-wave Raman laser in H₂," *J. Opt. Soc. Am. B*, vol. 16, pp. 1305–1312, 1999.
22. R. W. Minck, E. E. Hangenlocker, and W. G. Rado, "Stimulated pure rotational Raman

- scattering in deuterium," *Phys. Rev. Lett.*, vol. 17, pp. 229–231, 1966.
23. J. K. Brasseur, *Construction and noise studies of a continuous-wave Raman laser*. PhD thesis, Montana State University, 1998. Unpublished.
 24. P. A. Roos, *The diode-pumped cw Raman laser: classical, quantum and thermo-optic fundamentals*. PhD thesis, Montana State University, 2002. Unpublished.
 25. A. E. Siegman, *Lasers*. University Science Books, 1986.
 26. S. E. Harris and A. V. Sokolov, "Broadband spectral generation with refractive index control," *Phys. Rev. A*, vol. 55, pp. R4019–4022, 1997.
 27. S. E. Harris and A. V. Sokolov, "Subfemtosecond pulse generation by molecular modulation," *Phys. Rev. Lett.*, vol. 81, pp. 2894–2897, 1998.
 28. F. L. Kien, J. Q. Liang, M. Katsuragawa, K. Ohtsuki, K. Hakuta, and A. V. Sokolov, "Subfemtosecond pulse generation with molecular coherence control in stimulated Raman scattering," *Phys. Rev. A*, vol. 60, pp. 1562–1571, 1999.
 29. M. M. Audibert, C. Joffrin, and J. Ducuing, "Vibrational relaxation in hydrogen-rare-gas mixtures," *Chem. Phys. Lett.*, vol. 1, pp. 26–28, 1973.
 30. S. E. Harris, "Electromagnetically induced transparency," *Phys. Today*, pp. 36–42, July 1997.
 31. A. Yariv, *Quantum Electronics*. John Wiley & Sons, third ed., 1989.
 32. G. D. Boyd, J. W. D. Johnston, and I. P. Kaminow, "Optimization of the stimulated Raman scattering threshold," *IEEE J. Quan. Electron.*, vol. 5, pp. 203–206, 1969.
 33. P. Rabinowitz, A. Stein, R. Brickman, and A. Kaldor, "Stimulated rotational Raman scattering from para-H₂ pumped by a CO₂ TEA laser," *Opt. Lett.*, vol. 3, pp. 147–149, 1978.
 34. E. Hecht, *Optics*. Addison-Wesley, 4th ed., 2002.

35. S. Wolfram, *The Mathematica Book*. Cambridge University Press, 4th ed., 1999.
36. F. X. Kärtner, N. Matuschek, T. Schibli, and U. Keller, "Design and fabrication of double-chirped mirrors," *Opt. Lett.*, vol. 22, pp. 831–833, 1997.
37. R. H. Dicke, "The effect of collisions upon the Doppler width of spectral lines," *Phys. Rev.*, vol. 89, pp. 472–473, 1953.
38. R. W. Minck, E. E. Hangenlocker, and W. G. Rado, "Consideration and evaluation of factors influencing the stimulated optical scattering in gases," *Ford Motor Company, Scientific Laboratory Report*, vol. SL66-24, 1966.
39. P. A. Roos, L. S. Meng, and J. L. Carlsten, "Optimization of a nonresonant continuous-wave Raman laser," *J. Opt. Soc. B*, vol. unknown, p. unknown, 2002.
40. J. A. Barnes, T. E. Gough, and M. Stoer, "Laser power build-up cavity for high-resolution laser spectroscopy," *Rev. Sci. Instrum.*, vol. 70, pp. 3515–3518, 1999.
41. A. Ashkin, G. D. Boyd, and J. M. Dziedzic, "Resonant optical second harmonic generation and mixing," *IEEE J. Quantum Electronics*, vol. 2, pp. 109–123, 1966.
42. Z. Y. Ou, S. F. Pereira, E. S. Polzik, and H. J. Kimble, "85% efficiency for cw frequency doubling from 1.08 to 0.54 μm ," *Opt. Lett.*, vol. 17, pp. 640–642, 1992.
43. G. Breitenbach, S. Schiller, and J. Mlynek, "81% conversion efficiency in frequency-stable continuous-wave parametric oscillation," *J. Opt. Soc. Am. B*, vol. 12, pp. 2095–2101, 1995.
44. K. S. Repasky, L. S. Meng, J. K. Brasseur, J. L. Carlsten, and R. C. Swanson, "High-efficiency, continuous-wave Raman lasers," *J. Opt. Soc. B*, vol. 16, pp. 717–721, 1999.
45. J. K. Brasseur, P. A. Roos, L. S. Meng, and J. L. Carlsten, "Frequency tuning characteristics of a continuous wave Raman laser in H_2 ," *J. Opt. Soc. Am. B*, vol. 17, pp. 1229–1232, 2000.
46. T. Day, M. Brownell, and I. F. Wu, "Widely tunable external cavity diode lasers," *Proc. SPIE*, vol. 2378, p. 35, 1995.

47. K. S. Repasky, L. E. Watson, and J. L. Carlsten, "High-finesse interferometers," *Appl. Opt.*, vol. 34, pp. 2615-2618, 1995.
48. R. W. P. Drever, J. L. Hall, F. V. Kowalski, J. Hough, G. M. Ford, A. J. Munley, and H. Ward, "Laser phase and frequency stabilization using an optical resonator," *Appl. Phys. B*, vol. 31, pp. 97-105, 1983.
49. M. Bass, ed., *Handbook of Optics*. Volume IV: Fiber Optics and Nonlinear Optics, McGraw-Hill Book Company, Inc., second ed., 2001.
50. S. Kobayashi and T. Kimura, "Injection locking in AlGaAs semi-conductor laser," *IEEE J. Quantum Electronics*, vol. 17, pp. 681-689, 1981.
51. T. Kurosu, J. Ishikawa, N. Ito, and R. W. Fox, "High-resolution diode laser spectrometer for the Ca 1S_0 - 3P_1 transition," *Proc. SPIE*, vol. 2378, pp. 236-244, 1995.
52. P. A. Roos, L. S. Meng, and J. L. Carlsten, "Using an injection-locked diode laser to pump a cw Raman laser," *IEEE J. Quan. Electron.*, vol. 36, pp. 1280-1283, 2000.
53. P. A. Roos, J. K. Brasseur, and J. L. Carlsten, "Intensity-dependent refractive index in a nonresonant cw Raman laser that is due to thermal heating of the Raman-active gas," *J. Opt. Soc. B*, vol. 17, pp. 758-763, 2000.
54. D. A. Long, *Raman Spectroscopy*. McGraw-Hill International Book Company, 1977.
55. M. Harris, R. Loudon, T. J. Shepherd, and J. M. Vaughan, "Mode-hopping hysteresis in a single-frequency laser," *Opt. Commun.*, vol. 101, pp. 432-441, 1993.
56. M. D. Duncan, R. Mahon, J. Reintjes, and L. L. Tankersley, "Parametric Raman gain suppression in D₂ and H₂," *Opt. Lett.*, vol. 11, pp. 803-805, 1986.
57. G. C. Bjorklund, "Frequency-modulation spectroscopy: a new method for measuring weak absorptions and dispersions," *Opt. Lett.*, vol. 5, pp. 15-17, 1980.
58. G. C. Bjorklund, M. D. Levenson, W. Lenth, and C. Ortiz, "Frequency modulation spectroscopy," *Appl. Phys. B*, vol. 32, pp. 145-152, 1983.

59. I. S. Gradshteyn and I. M. Ryzhik, *Table of Integrals, Series, and Products*. Academic Press, fifth ed., 1994.
60. K. G. Kibbrecht and J. L. Hall, "A low-noise high-speed diode laser current controller," *Rev. Sci. Instrum.*, vol. 64, pp. 2133-2135, 1993.

MONTANA STATE UNIVERSITY - BOZEMAN



3 1762 10379230 3